UNIVERSITÀ DI PISA

FACOLTÀ DI INGEGNERIA

Dipartimento di Ingegneria Civile e Industriale

Corso di Laurea Magistrale in
Materials and Nanotechnology

TESI DI LAUREA

Surface reconstructions induced by Rb on Si(111)

Relatore:

Dr. Stefan Heun

Candidato:

Letizia Ferbel

Correlatore:

Dr. Stefano Veronesi

Anno Accademico 2019/2020

Contents

Chapter 1

Introduction

Motivated by the extremely wide use of semiconductor devices in electronic industry, studies of semiconductor surfaces have been an active field. Recalling the history of modern surface physics, the electrical conduction near semiconductor surfaces has been an important subject since the discovery of transistors in the 1950s [1]. With the ongoing reduction in size of electronic devices, surface effects are becoming more and more important, and surface analysis provides a means to correlate device performance with surface or thin film composition. This knowledge can be used to accelerate the development of new materials and to improve the performance of existing materials systems. Experimental tools, above all scanning tunneling microscopy (STM), as well as advanced theoretical approaches provoked a more profound understanding of semiconductor surface and interface properties.

It is well known that the surface of materials may differ from the bulk in both structure and composition. The surface of a solid crystal is created by breaking interatomic bonds within the three dimensional periodicity, which leaves these bonds dangling into the vacuum. In order to minimize the number of dangling bonds, a wide range of surfaces undergo a reconstruction, which consists in a rearrangement of the surface atoms with respect to the bulk structure. This can affect one or more layers at the surface [2].

The best-known semiconductor is silicon (Si). Silicon is a crystalline covalent solid, and its (111) surface is among the most fascinating and a great example of a surface reconstruction. After a cleave, the Si(111) surface shows a metastable (2×1) reconstructed structure. A stable (7×7) structure is observed after annealing this surface to above 600°C [3]. In the specific case of the Si(111)-(7×7) surface, the number of dangling bonds reduces to 19 by the reconstruction into the dimer-adatom-stacking-fault (DAS) structure, a number to be compared to the 49 dangling bonds, in the same surface area, of a Si(111)-(1×1) ideal surface [4]. The Si(111)-(7×7) reconstructed surface has received much attention due to the fact that it has metallic conducting properties despite the fact that bulk silicon is a semiconductor [5].

In connection with the development of nanoelectronic devices, the technological and fundamental scientific interest in metal/semiconductor interfaces increases. Adsorption of metal atoms modifies the electronic structures of clean semiconductor surfaces and, in many cases, changes their geometric structure.

Of particular interest is the chemisorption of alkali metals on semiconductors. These are metals that have a simple electronic structure: a single valence *s* electron interacting with the surface. From a fundamental point of view, such studies are interesting because alkali metal overlayers on semiconductor surfaces represent simple model systems in the formation of metal semiconductor interfaces and for metallization processes. At the same time, the bonding character (i.e., ionic or covalent) of alkali metals on semiconductor surfaces is still

controversial, since it concerns the amount of charge transfer between alkali metal adatoms and substrate atoms [6]. Actually, this charge transfer is a driving force for metal-induced reconstructions because the surface atomic arrangement of the deposited metal overlayer is decisive and may play a crucial role in determining the geometrical structure of the interface. Moreover, the strong mutual interaction between alkali metal adatoms may result in two-dimensional ordered structures and phase transitions in adsorbed layers. Thus, depending on coverage, the geometrical structure of adsorbate-covered semiconductor surfaces may be determined by the competition between alkali-semiconductor and alkali-alkali interactions both being defined by the atomic sizes and the polarizabilities of the alkali metal atoms.

The ionic or covalent bonding character between the alkali metal and the silicon atoms can also give rise to interesting phenomena such as a large enhancement in the oxidation rate of the Si substrate when covered with alkali metals, or the ability of thin intralayers of alkali metal atoms to control the band offsets in heterojunctions and in insulator-semiconductor interfaces. Lastly, alkali metal absorption on the silicon surface has been of great help to unmask the proper structure of the (7×7) reconstruction of Si, since alkali atoms are monovalent and adsorb preferentially on dangling bonds at the surface [7].

Knowledge of adsorption sites and substrate geometry from experiment will provide a better starting point for theoretical calculations to predict the electronic structure and properties of these interfaces. In addition, studying the changes in surface reconstruction geometries of these interfaces with different AM coverages and under annealing will provide information on the adsorption process.

Various ordered structures of the alkali metal-semiconductor interface have been observed at submonolayer metal coverages, and a (3×1) phase has been frequently observed for alkali-metal adsorption on the Si(111) surface [8]. The Si(111)-(3×1) surface exhibits unusual electronic and chemical properties, e.g. a semiconducting surface and passivation against oxidation [9] [10]. Although in the literature there is experimental evidence for the formation of the (3×1) reconstruction induced by all alkali metals, for what concerns rubidium this evidence is just limited to the reciprocal space.

In this thesis, I report a wide investigation on the interaction and induced reconstructions by Rb on the Si(111)-(7×7) surface. By tuning parameters of the induced surface reconstructions, a better and more detailed understanding of the Rb/Si(111) system has been gained.

Sample analysis via Low Energy Electron Diffraction allowed to observe for the first time a Rb/Si(111)-(6×1) reconstruction. Moreover, the Low Energy Electron Diffraction analysis allowed to obtain a fast characterization of the samples as well as qualitative information on the surface induced modifications and its periodicity.

The use of Scanning Tunneling Microscopy allowed to obtain the first real space characterization of the Rb/Si(111)-(3×1) surface. Scanning Tunneling Microscopy provided a direct and local information on the surface arrangement as well as further insights on the interaction between Si and Rb atoms and on the film growth dynamics. On the other hand, Scanning Tunneling Spectroscopy has provided some insight on the electronic structure of the system.

This entire work has been realized at the facilities of Laboratorio NEST. Sample preparation as well as their characterization, done via low energy electron diffraction (LEED) and scanning tunneling microscopy and spectroscopy (STM and STS), has been performed in an Ultra-High Vacuum environment (UHV chamber of a RHK Technology STM).

A summary description of the thesis chapters is briefly listed below:

- Chapter 2 reports an introduction to the two elements involved in this thesis, namely rubidium and silicon. It also reviews the State of the Art of the current research as

well as the theoretical and experimental results already obtained for this alkali metal-semiconductor system.

- Chapter 3 outlines the experimental setup, operating principles, and methods used to perform this work: namely the UHV system, LEED, STM, the Rb evaporator, and the residual gas analyzer (RGA).
- Chapter 4 reports the results obtained via LEED and STM on the pristine Si(111)-(7×7) surface.
- Chapter 5 reports the results obtained via LEED and STM on the Rb adsorption on Si(111) at room temperature and the effect of annealing cycles on these samples.
- Chapter 6 reports the results obtained via LEED and STM on the Rb adsorption on Si(111) held at elevated temperature during deposition and the effect of annealing cycles on these samples.
- Chapter 7 provides a summary of the results and a comprehensive discussion of the Rb/Si(111) system. This chapter also briefly outlines the conclusions of this work.

Chapter 2

State of the Art

This chapter starts with an introduction to rubidium: its properties and current applications are shown. We then review the literature on silicon and its surface reconstructions, with a particular focus on the (7×7) reconstruction. Lastly, an overview of alkali-metals/Si practical importance, interaction, and the experimental results obtained on these systems are reviewed. A particular focus has been placed on the (limited) literature on the Rb/Si(111) system.

2.1 Rubidium

Rubidium (Rb) is the 37th element of the periodic table. It was discovered in 1861 by two German chemists, Gustav Robert Kirchhoff and Robert Wilhelm Bunsen who used a spectroscope that the two scientists have built the year before. The discovery of this new material happened while observing the spectrum of the mineral lepidolite as it burned: the spectrum showed two dark red lines, and the newly discovered element was called Rubidium (which in Latin is the word for dark red). The discovery of rubidium, with the discovery of cesium the year before, inaugurated a new era in the methods used to find new elements.

Rubidium, together with five other chemical elements, lithium, sodium, potassium, cesium, and francium, belongs to Group 1, the leftmost column of the periodic table, commonly known as the group of the alkali metals. The six alkali metals have some common physical and chemical properties that can be readily explained by their valence electron configuration (AM:[Noble gas] ns$-$1), which results in weak metallic bonding. Hence, all the alkali metals are soft and have low densities. Rubidium is the first alkali metal in the group to have a density higher than water, so it sinks, unlike the metals above it in the group. All alkali metals have low melting points (T_m(Rb) = 39.3°C). At the same time, their thermal and electrical conductivities are among the highest of all known materials. They all crystallize in the body-centered cubic crystal structure, and have distinctive flame colors because their outer *s* electron is easily excited. The (ns^1) configuration results in the alkali metals having large atomic and ionic radii. Their chemistry is dominated by the loss of their lone valence electron in the outermost s-orbital, to form the +1 oxidation state, due to the ease of ionizing this atom and the high second ionization energy. Most of the chemistry has been observed only for the first five members of the group, being Fr a short lifetime radioactive atom. All alkali metals are paramagnetic, due to the single unpaired s electron. Moreover, the stable alkali metals are all silver-coloured metals, except for caesium, which has a pale golden tint.

Alkalies are extremely reactive in standard conditions of temperature and pressure. Because of their high reactivity, they rapidly oxidize when exposed to air. This is the reason why they need to be stored under oil and are naturally found in salts, but never as pure elements.

2.1.1 Applications

Rubidium can be used in a variety of applications. Rubidium has 32 isotopes, and only two of them are naturally occurring isotopes, namely ^{85}Rb and the radioactive ^{87}Rb. These isotopes have natural abundance of 72.17% and 27.83%, respectively [11]. Among the non-natural isotopes, ^{82}Rb finds some applications. This radioisotope is produced by electron-capture decay of ^{82}Sr.

The resonant element in atomic clocks utilizes the hyperfine structure of rubidium's energy levels, and rubidium is thus useful for high-precision timing. It is used as the main component of secondary frequency references (rubidium oscillators) in cell site transmitters and other electronic transmitting, networking, and test equipment. These rubidium standards are often used with GPS to produce a "primary frequency standard" that has greater accuracy and is less expensive than caesium standards. Such rubidium standards are often mass-produced for the telecommunication industry [12].

Rubidium compounds are sometimes used in fireworks to give them a purple color. Rubidium can be used for ion propulsion systems in space exploration. It has also been considered for use in a thermoelectric generators using the magnetohydrodynamic principle, where hot rubidium ions are passed through a magnetic field, to generate an electrical current [13]. Rubidium, particularly vaporized ^{87}Rb, is one of the most commonly used atomic species employed for laser cooling and Bose-Einstein condensation [14]. Its desirable features for this application include the ready availability of inexpensive diode laser sources at the relevant wavelength and the moderate temperatures required to obtain substantial vapor pressures. For cold-atom applications requiring tunable interactions, ^{85}Rb is preferable due to its rich Feshbach spectrum [15].

Rubidium has been used for polarizing ^{3}He, producing volumes of magnetized ^{3}He gas, with the nuclear spins aligned rather than random. Rubidium vapor is optically pumped by a laser, and the polarized Rb polarizes ^{3}He through the hyperfine interaction. Such spin-polarized ^{3}He cells are useful for neutron polarization measurements and for producing polarized neutron beams for other purposes [16].

Other uses of rubidium include a working fluid in vapor turbines, as a getter in vacuum tubes, and as a photocell component. Rubidium is also used as an ingredient in special types of glass, in the production of superoxide by burning in oxygen, in the study of potassium ion channels in biology, and as the vapor in atomic magnetometers. In particular, ^{87}Rb is used with other alkali metals in the development of spin-exchange relaxation-free (SERF) magnetometers [17].

^{82}Rb is used for positron emission tomography, as biomarker. Rubidium is very similar to potassium, and tissue with high potassium content will also accumulate the radioactive rubidium. One of the main uses is myocardial perfusion imaging. This allows the use of radioisotope ^{82}Rb in nuclear medicine to locate and image brain tumors [18]. Moreover, ^{82}Rb decays to produce strontium isotopes and lend to the ability to age-date rock strata [19].

This is just a partial list of practical applications of this element. There are a lot of other possible uses which have been and still are under investigation. In this thesis work we investigate the interaction between Rb atoms and silicon and the Rb-induced reconstruction of the latter. This is a system of particular interest in surface science and electronics, as will be shown in the next sections.

2.2 Silicon

The best-known semiconductor is silicon (Si). It is the basis for most electronics today. Si is an example of a covalent crystal (also called 'lattice crystal'), i.e. a crystal in which atoms are linked by covalent bonds, which crystallizes in the diamond structure. The diamond structure can be described as two interpenetrating fcc lattices displaced by $(a/4)(1,1,1)$ along the body diagonal of the conventional cube (see Fig. 2.1). The underlying Bravais lattice is fcc with two atoms forming the basis in positions $(0,0,0)$ and $(a/4)(1,1,1)$. The coordination number is 4, i.e. each atom in a given sublattice is surrounded by four atoms of the other sublattice, at a distance of $(a/4)\sqrt{3}$, in a tetrahedral configuration (each atom in the crystal lattice has sp^3 hybridized orbitals). The lattice constant in the case of Si is $a = 5.43$ Å while each bond is 2.35 Å long and has a bond strength of 2.35 eV [20].

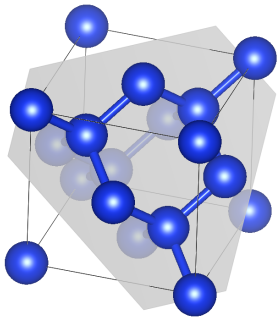

Figure 2.1: Diamond crystal structure of silicon. The outlined plane corresponds to the (111) plane.

Silicon belongs to the elements of group *IV*. In the most external shell there are four electrons ($3s^2$,$3p^2$); the inner shells are completely filled. The most external s and p_x, p_y, p_z atomic orbitals of the two atoms in the unit cell form bonding (and antibonding) combinations, which generate the highest valence bands (and the lowest conduction bands) of the crystal. For what concerns the energy bands, silicon is a semiconductor with indirect band gap 1.17 eV (at $T = 0$ K) [20].

Of special interest is the trend of the energy bands around the fundamental gap. In silicon, in the ΓX direction, the minimum of the conduction band occurs at the point $\vec{k} \approx (2\pi/a)(0.85,0,0)$; there are six equivalent minima, nearer to the boundary of the Brillouin zone (see Fig. 2.2). The top of the valence band is at Γ'_{25}. The state Γ'_{25} arises from the three p_x, p_y, p_z bonding orbitals, which are degenerate at the center of the Brillouin zone; considering the spin of the electrons, Γ'_{25} is sixfold degenerate. Spin-orbit interaction splits the topmost valence bands into two groups: $p_{3/2}$ bands (heavy-hole and light-hole bands) with degeneracy 4 at the Γ point (Γ_8^+ state), and $p_{1/2}$ bands (split-off band) with degeneracy 2 (Γ_7^+ state). The spin-orbit separation Δ_{SO} of the valence bands at Γ is 0.044 eV for Si [20].

2.2.1 Si(111) surface reconstructions

When a crystal is cleaved to create a new surface, each surface atom is left with one or more unpaired electrons as a result of reduced coordination. These electrons are localized in so called dangling bond orbitals. The number and spatial orientation of these orbitals depends on the crystallographic plane within which the crystal is cleaved. Dangling bonds increase the free energy of the surface. Reconstruction refers to a change in the two-dimensional structure of the surface layers, in addition to changes in the position of the entire layer. Surface reconstruction is the process that occurs to minimize the surface energy and to take care

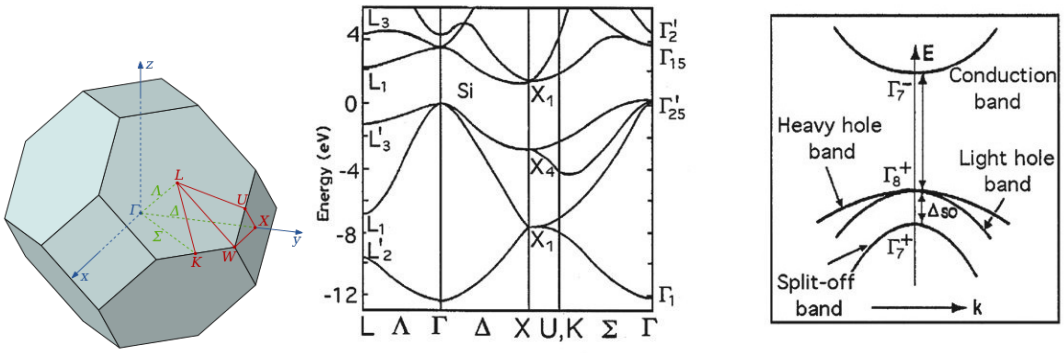

(a) (b)

Figure 2.2: (a) Diagram of the first Brillouin zone of a diamond lattice such as silicon, with points of high symmetry marked. (b) Left: band structure for silicon, and right: schematically reports the typical band structure of cubic semi-conductors near the gap at $\vec{k} = 0$; Δ_{SO} denotes the spin-orbit splitting. (a) and (b) from Refs. [21] and [20], respectively.

of the dangling bonds associated with the topmost atoms of an atomically clean surface. The formation of new bonds can occur between neighbouring surface atoms or between surface atoms and atoms supplied by diffusion from nearby sources such as steps [22]. Each new bond reduces the free energy of the surface by approximately 1 eV per atom [23], but at the expense of increasing surface stress [24]. This is minimized by relaxing atoms at and beneath the surface. Each atomic relaxation reduces the free energy of the surface by approximately 0.01 eV per atom [24]. Surface reconstruction can be either activated or passive. Activated surface reconstruction requires energy to occur, whereas passive surface reconstruction does not. The surface obtained following reconstruction depends on the crystallographic plane within which the crystal is cleaved, and on the technique used to prepare the surface following cleavage. It always corresponds to the lowest energy structure kinetically accessible under the conditions of preparation [22].

Silicon exhibits several well known surface reconstructions. These different well ordered reconstructions depend on temperature and crystal face. The reconstruction of Si along the (111) plane is one of the most complicated and fascinating structures. It has been of great interest and was widely investigated in fields like surface science, materials science, and nano-technology. Si(111) refers to the cleaved face of silicon along the set of atomic planes perpendicular to the vector $(1,1,1)$ (highlighted in figure Fig. 2.1 and Fig. 2.3).

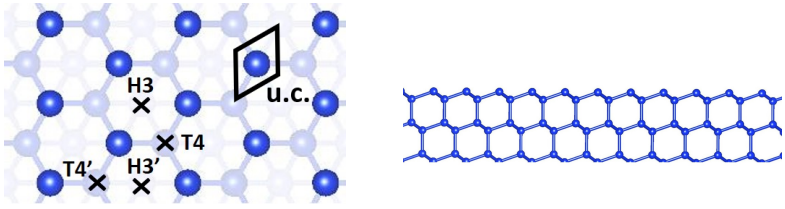

(a) (b)

Figure 2.3: (a) Top and (b) lateral view of the Si(111) surface. The primitive unit cell is show in (a).

The unreconstructed Si(111) surface forms a hexagonal surface lattice with a primitive lattice vector of 3.84 Å, and is known as the (1×1) surface. The half filled dangling bonds on each surface atom raise the free energy of the surface significantly. This free energy, if kinetic permits, is what drives the surface atoms to reconstruct into the reconstruction with the lowest free energy, as thermodynamic systems have the tendency to find their lowest

energy states.

Cleavage of Si(111) at low temperature ($T \leq 330$°C) in UHV produces a (2×1) structure. An annealing of this surface to above 330°C generates a (5×5) structure, which upon a further heating to 600°C becomes a (7×7) structure. It is interesting to mention that this structure is stable up to about 850°C when it converts back to a (1×1) structure [3]. Since its discovery in 1959 by Schlier and Farnsworth, the (7×7) reconstruction has been of particular interest both from a theoretical and experimental point of view due to its high stability.

2.2.2 The DAS Model

The structure of the Si(111)-(7×7) reconstructed surface has been subject of debate since its discovery [25]. Nowadays, the atomic arrangement commonly accepted is the dimer-adatom-stacking fault (DAS) structure proposed by Takayanagi et al. in 1985 [4] based on transmission electron diffraction studies (TED).

The Si(111)-(7×7) structure involves several types of atomic positions in the top three atomic layers and has a unit cell with lattice vectors 26.88 Å long. According to the DAS model, these layers can be identified as an unreconstructed base layer (1×1), a dimer layer, a stacking faulted rest atom layer, and an adatom layer (as reported in Fig. 2.4a).

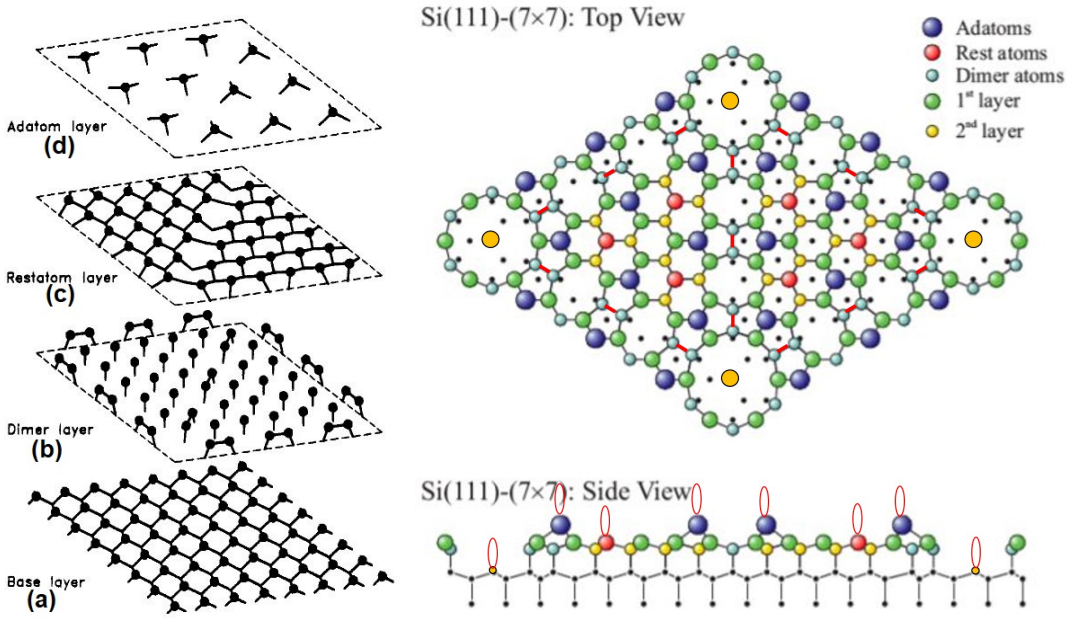

Figure 2.4: DAS model of the Si(111)-(7×7) surface. (a) Layer by layer construction of the Si(111)-(7×7) structure and (b) top and side view (dangling bonds highlighted in orange) of the Si(111)-(7×7) unit cell as described by the DAS model. (a) and (b) from Refs. [26] and [27], respectively.

In the unreconstructed (1×1) base layer (Fig. 2.4a panel (a)) each atom has a single dangling bond saturated by an atom in the dimer layer above (Fig. 2.4a panel (b)). In the dimer layer (Fig. 2.4a panel (b)) there are 9 dimer per unit cell and single atoms. Each atom in the dimer layer saturates the dangling bond of an atom in the base layer below (Fig. 2.4a panel (a)). There is an atomic vacancy at each corner of the layer which gives rise to the so-called corner holes. Dimers are formed between atoms at the edges of the layer and between atoms along the short diagonal crossing its center. These dimers divide the unit cell into two distinct triangular subunits. Each dimer atom has two dangling bonds, while all other atoms

in this layer have three dangling bonds. These dangling bonds are saturated by atoms in the rest atom layer above (Fig. 2.4a panel (c)). In the rest atom layer there are 42 atoms, and each atom saturates the dangling bonds of 3 atoms in the dimer layer below (Fig. 2.4a panel (b)). The unterminated rest atom layer has a total of 42 dangling bonds. In order to saturate all these dangling bonds, the rest atoms in one triangular subunit must occupy positions out of registry with the positions of the rest atoms in the opposite subunit. This is called a stacking fault. Thus, the stacking fault divides the two triangular subunits in a faulted half (FHUC) and an unfaulted half unit cell (UHUC), and hence the two triangular subunits of the unit cell are not equivalent. The left half of the unit cell in Fig. 2.4b has a stacking fault relative to the bulk. The triangular units alternatively faulted and unfaulted are bounded by dimers rows. It is not possible to saturate all of these 42 dangling bonds using tri-coordinated silicon atoms. In order to best overcome this problem, each of the 12 atoms in the adatom layer above (Fig. 2.4a panel (d)), forming a local 2×2 structure, saturates the dangling bonds of 3 atoms in the rest atom layer below (Fig. 2.4a panel (c)). This reduces the number of dangling bonds in the rest atom layer to 6 and leaves 12 dangling bonds in the adatom layer.

By adapting the DAS model, the 49 dangling bonds of a bulk-terminated (7×7) unit cell are reduced to 19 (each adatom, restatom, and corner hole exhibits one dangling bond). The tunneling current in STM of the Si(111)-(7×7) surface is due to these dangling bonds. The stacking fault is located between the third and fourth atomic layer in the FHUC, which makes the latter more reactive than UHUC.

Summarizing, the DAS model (of a unit cell) can be described by

- twelve adatoms (occupying T4 sites, see Fig. 2.3a, blue balls in Fig. 2.4b);
- six rest atoms (red balls in Fig. 2.4b);
- two triangular subunits;
- nine dimers (pairs of atoms) per unit cell which border the triangular subunits (light blue balls in Fig. 2.4b);
- one deep corner hole.

Besides the (7×7) reconstruction of the $((2n+1) \times (2n+1))$ DAS reconstruction family, there are also the (3×3), (5×5), (9×9) etc. reconstructions. These other structures can be obtained from the (7×7) structure by eliminating or creating one dimer at a time along the dimer strings, and eliminating or creating corresponding rows of adatoms and rest atoms. Furthermore, the formation of the dimer strings and the stacking fault are more important than the introduction of adatoms in terms of lowering the surface energy. The dimer strings dictate the triangular shape as the basic unit of the DAS structures, since this is the only way the dimer strings can be combined without introducing other (less energetically favorable) structures. However the (7×7) represents the most stable surface rearrangement, i.e. the one with lowest energy. Nevertheless, other DAS structure could be observed in non-equilibrium conditions [26].

2.2.3 Electronic structure of Si(111)-(7×7)

The electronic structure is closely related to the atomic structure, so it should in principle show the effects of the surface reconstruction. The (7×7) reconstruction of Si(111) has the interesting property of being metallic despite bulk Si being a semiconductor. It is believed that the dangling bonds of the adatoms play a crucial role in the high conductivity and that this is predominantly a surface-state band effect.

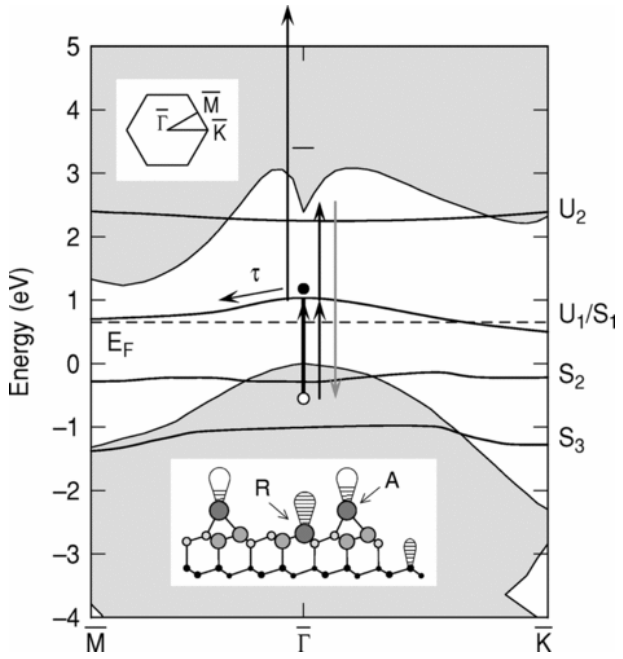

Figure 2.5: Electronic structure of Si(111)-(7 × 7). U_n states denote unfilled surface states, and S_n states denote filled surface states. The shaded regions are the projected bulk bands. E_F shows the pinned Fermi energy with the energy measured with respect to the valence band maximum. The upper inset shows the Brillouin zone of silicon and highlights high symmetry points. The lower inset shows a side view of the Si(111)-(7 × 7) reconstruction with a filled rest atom dangling bond and 5/12 filled adatom dangling bonds. From Ref. [5].

According to the DAS model, each (7 × 7) unit cell contains 19 dangling bonds located at 12 adatoms, six rest atoms, and one corner hole. The adatoms donate seven electrons to the restatoms and the corner hole such that only five electrons are left in the 12 adatoms, thus each being 5/12 saturated (see Fig. 2.5). This gives rise to a metallic band manifold within the bulk band gap (Fig. 2.5, band U_1/S_1), pinning the Fermi level at 0.65 eV above the valence-band maximum. The S_n labelled states are filled surface states, and the U_n labeled states are unfilled surface states. The state S_2 arises from the fully occupied dangling bonds of the rest atoms, while the states S_3 and U_2 originate from the backbonds of the adatoms to the next atomic layer. Of course, the Si(111)-(7 × 7) surface differs considerably from a conventional metal. Its electron density is small, the metallic bands are formed by localized sp^3 orbitals instead of delocalized sp electrons, and a sizable on-site Coulomb interaction points at strong correlation effects. Nevertheless, Si(111)-(7 × 7) apparently retains its metallic character even at low temperatures [5]. The shaded region in Fig. 2.5 shows the projected bulk bands, and a degenerate surface resonance exists when a surface state crosses into this bulk band projection.

The existence of a substantial density of states at the Fermi energy results in the Fermi level being pinned at ∼ 0.65 eV [28]. Moreover, the pinning is independent from the type of doping (p or n).

2.3 Alkali metals adsorption on the Si(111) surface

After the discovery of the stable (7 × 7) reconstruction, a lot of studies have been published on the adsorption of foreign atoms by this Si(111)-(7 × 7) surface. The alkali metal-Si interface has been a main focus of experimental and theoretical investigations, because the

alkali metal overlayers in semiconductors represent examples of simple model systems for the formation of metal-semiconductor interfaces and for metallization processes. Another reason for these studies is the ionic or covalent bonding character between the alkali metal and the silicon atoms. This interaction can give rise to interesting phenomena such as a large enhancement in the oxidation rate of the Si substrate when covered with alkali metals, and the ability of thin intralayers of alkali metal atoms to control the band offsets in heterojunctions, and in insulator-semiconductor interfaces. Lastly, alkali metal absorption on the silicon surface has been of great help to unmask the proper structure model of the (7×7) reconstruction of Si, since alkali atoms are monovalent and will preferentially adsorb on dangling bonds at the surface.

Both ordered and disordered structures have been observed upon AM adsorption on the Si(111)-(7×7). The drastic chemical, electrical and structural changes that have been observed highly depend on the coverage and temperature. In the following, I show common features, differences and results obtained via various analysis techniques on both ordered and disordered structures. At the end I focus on the current literature about Rb adsorption on the Si(111) surface, since this system will be the center of the investigation of this thesis.

2.3.1 Ordered superstructures: the (3×1) reconstruction

At submonolayer coverage, all alkali metal have been found to induce a (3×1) reconstruction in Si(111). In the last decades, the (3×1) reconstruction induced by alkali metals on the Si(111) surface has been an object of extensive investigations by many groups using surface sensitive techniques and theoretical calculations. It has attracted particular interest both from a chemical and electrical prospective, because of its inactivity against oxidation and its semiconducting character.

Some common features between different AM-induced Si(111)-(3×1) structures have been found. These can be summarized as are as follows:

(1) Si(111)-(3×1) is plausibly very similar for all metals and is predominantly a Si(111) substrate reconstruction. The (3×1) reconstruction has been similarly found for Ge(111) as substrate [29]. Moreover, the metals stabilizing this surface structure are not only limited to the alkalies but metals such as Ag [30, 31], Ca [32] or Mg [33] induce the same structure.

(2) The AM/Si(111)-(3×1) reconstruction can be achieved either upon deposition on an heated substrate without further annealing [8, 9, 34, 35] or upon deposition at RT and a subsequent annealing [30, 31, 36, 37]. High temperature deposition and subsequent surface transition from $(7 \times 7) \rightarrow (3 \times 1)$ has been the most studied method. The temperature range in which this (3×1) superstructure is observed depend on the adsorbate and has been found to be the widest for Li, about 400°C, and the narrowest for Cs, about 100°C [8]. It has been reported, by STM analysis, that it is possible to obtain a 100% transformation of the surface to (3×1) [38]. In the case of RT deposition instead, only a small fraction of the surface has been found to convert to (3×1) upon a mild annealing of the RT deposited samples [36].

(3) The AM/Si(111)-(3×1) surface is semiconducting. The tunneling I-V curves measured via STS on the (3×1) surface [9, 31, 34, 38] show a distinctive band gap indicating a semiconducting nature of the surface. STS results are compatible also with photoelectron spectroscopy results which confirm the presence of a band gap, and thus the semiconducting nature of this surface [39–41].

(4) π-bonded chains formed by top Si atoms are present on this surface. Real space characterization of the surface via STM demonstrated that the empty as well as the occupied surface states are arranged in parallel rows oriented in a $\langle 1\bar{1}0 \rangle$ direction (see Fig. 2.6). The separation between the rows (~ 11.52 Å) and the granular structure along them establishes a (3×1) unit mesh [9, 31, 34, 37, 38, 41].

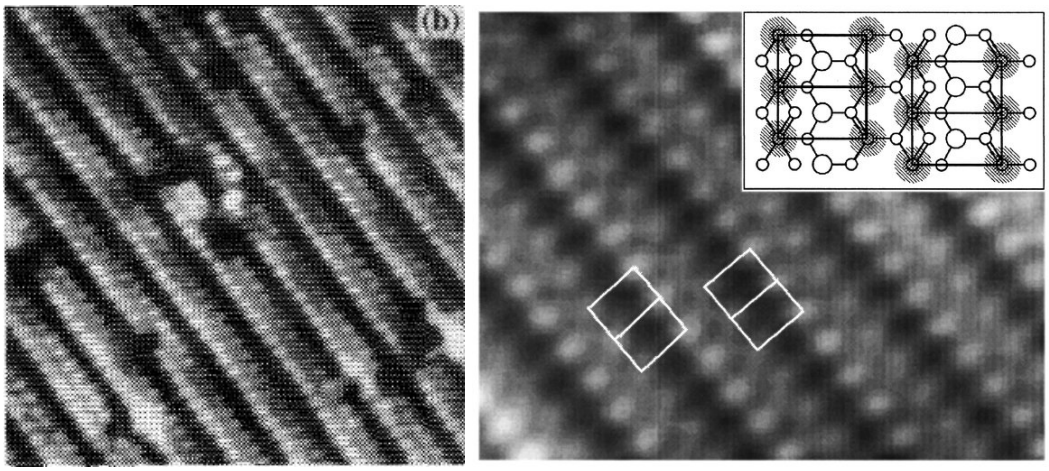

Figure 2.6: Atomically resolved STM images (filled state) of Na induced Si(111)-(3×1) reconstruction showing zigzag chains separated by a single atomic row. Image parameters: (a) -2.5 V, 20 pA, and (b) -1.8 V, 20 pA. From Refs. [38] and [42], respectively.

(5) The $(7 \times 7) \rightarrow (3 \times 1)$ transition has been found to be reversible. Annealing at sufficient high temperature the (3×1) surface will restore the (7×7) periodicity of the pristine substrate. The temperature range for which this transition occurs depends on the alkali metal, however complete desorption of several alkalies has been found at around 700°C [35].

Even though similarities exist, the atomic size difference and interactions with the substrate lead to differences among the different alkalies. For instance, the (7×7) to (3×1) phase conversion in the case of Na extends from the step edges and is accompanied by monolayer island formation situated on the terraces. For any other alkali metal such islands do not form [29, 38].

Adsorption of Na on the silicon surface produces an highly ordered (3×1) surface with little or no defects. In the case of other alkali metals, the (3×1) surface often contains vacancy defects or additional atoms adsorbed on top of the rows [38]. Additionally, it has been possible to grow highly ordered (3×1) Na multilayers on the Si(111) surface, while for other alkalies the growth was either not possible (e.g. Cs) or of poor quality (e.g. K) [38]. These difference between Na and the other alkalies have been ascribed to a size difference: the lattice mismatch between the bcc Na(110) and the Si(111) planes is small, thus also the strain involved in the surface transformation is small. In the case of both Na and K, the first overlayer was found to be metallic, indicating that this type of metallic transition is irrelevant to the surface ordering.

The importance of the atomic size becomes clear in the case of Cs adsorbed on the Si(111) surface [35, 43]. There is PES (PhotoEmission Spectroscopy) and LEED evidence that at high Cs coverage the (3×1) structure was transformed to the (6×1) by enlarging the (3×1) domain size. The appearance of this phase with doubled periodicity is ascribed to the large atomic size of the Cs atoms and the Cs nearest neighbour distance which is larger then the Si(111)-(1×1) lattice spacing.

The observed differences among the alkalies led to controversies on the structural model as well as the saturation coverage of the alkali metal adsorbed (3×1) surfaces. The extended Pandey model, for which the absolute metal coverage of the (3×1) phase is 1/3 ML, is now considered the most plausible candidate. This model will be described in detail in sec. 2.3.3.

2.3.2 Disordered adsorption

When Alkali metals are deposited on a Si(111)-(7×7) substrate held at RT or at a higher temperature, outside the range of the (3×1) phase formation, the the alkali will be adsorbed to form a disordered overlayer or not adsorb at all.

Structural and electronic changes on the (7×7), induced by alkali deposition up to 1 ML, has been observed by RHEED, XSW, XPS, XPD and PES techniques. In particular RHEED studies on Cs [35], K [44], Li [44] have shown several induced reconstructions called δ-(7×7) [8] and generically modified (7×7). Deposition of increasing AM amounts led to the observation of these modified (7×7) prior to the appearance of a (1×1) structure. XSW measurement showed multisite occupancy with preferential adsorption on the H_3 and T_4 site, and the remaining atoms occupying the atop site or adatom site (ref. Fig. 2.7) [45–47] [1]. UPS and inverse PES on K [49,50] and Cs/Si(111)-(7×7) [49] surface have been observed. Both metals were found to interact preferentially with the adatom dangling bonds. This interaction lowers the energy of the filled surface state S_1 and the surface becomes semiconducting. At the same time the empty surface state U_1 became weaker and totally vanished at saturation coverage.

Real space characterization via STM have complemented the information about the AM-Si(7×7) system. In details, STM and work function measurements on alkali metals deposited on the Si(111)-(7×7) surface at RT and low coverages were presented [36,48]. STM experiments carried out on Li, Na, K and Cs indicated the adatom sites, mainly on the faulted half of the (7×7) cell, as preferential adsorption sites at very low coverage (less than about 0.01 ML) and the formation of clusters with a successive occupation of the unfaulted half with the increasing coverage.

Therefore, when alkali metals are deposited on a Si(111)-(7×7) substrate at conditions which do not allow the formation of (3×1) reconstruction, some structural modifications are induced to the (7×7) surfaces and the electronic configuration is modified. This underlines that alkali are not merely standing on the surface but interacting with the Si atoms.

2.3.3 Rb on Si(111)

As discussed in the previous sections, there are still some unanswered questions on the AM/Si(111) interaction. In particular, the AM atomic size seems to play an important role in the differences among the alkalies. Rb has a large atomic radius which is comparable to Cs. Moreover, a real space characterization as well as a complete investigation of the Rb(3×1) structure is still missing. These are some of the reasons that make Rb worth studying, relevant and necessary.

The first study of Rb adsorption on the Si(111)-(7×7) dates back to 1985. Using RHEED, Daimon and Ino [8] studied the adsorption of alkali metals on the Si(111)-(7×7) both at room temperature and on the heated substrate. When the alkali metals were deposited at room temperature, the RHEED intensity distribution changed gradually and after the deposition of about one monolayer, a new superstructure with (7×7) periodicity was observed, which however has a different intensity distribution from that of the original (7×7) structure. They called it $\delta(7 \times 7)$. When the alkali metals were deposited at about 500°C, the (3×1) superstructures have been observed for the first time for all alkali metals: Li, Na, K, Rb and Cs. The temperature range in which this (3×1) superstructure is observed is the widest for Li, about 400°C, and the narrowest for Cs, about 100°C.

[1] To note that these XSW measurement yield opposite results, on the AM site occupancy, compared to STM [36,48] and PES [49] observations. However, XSW totally excludes the possible adsorption on the 19 dangling bonds, in agreement with other observations.

The adsorption sites of Rb deposited at room temperature on the (7×7) silicon surface were studied by X-ray standing waves (XSW). Fig. 2.7 indicates the adsorption sites cited in these studies. Low (~ 0.06 ML), medium (~ 0.15 ML) and high (the coverage at which the

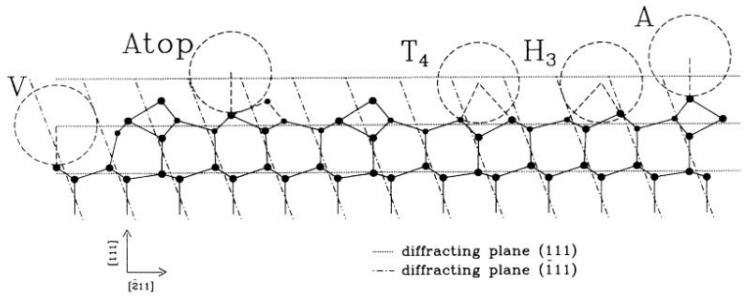

Figure 2.7: $(\bar{1}11)$ side view of the 7×7 reconstructed cell. The threefold hollow (H_3), threefold filled (T_4), on-top (A), adatom on top (Atop) and vacancy (V) sites are indicated. From Ref. [45]

LEED pattern showed a $\sim (1 \times 1)$ structure, referred as saturation coverage) Rb coverages of the Si(111)-(7×7) have been analyzed [45–47]. The XSW measurements, for all the initial coverages, showed occupancy of more than one site. The H_3, the T_4, and all dangling bonds were considered as possible adsorption sites. The results pointed to a distribution where at least fifty percent of the Rb atoms adsorb at the H_3 site on the unfaulted half of the unit cell and at the T_4 site, a large percentage of the other Rb atoms occupies the Atop sites, mainly on the faulted half. Conclusions were the same at all coverages.

Eteläniemi et al. [46] starting from a sample with Rb at saturation coverage, also reported the structure changes upon annealing cycles [46]. Annealing in the range of 300-350°C a the sample at saturation coverage led to observe a much better ordered adlayer, and the adsorption on the H_3 site of the unfaulted half of the unit cell was promoted. It is suggested that the observation of the H_3 site in this temperature range is related to the formation of (3×1) domains. This would also explain why unfaulted sites are predominant since there is no faulting at the (3×1) reconstruction. Moreover, this interpretation is agreement with STM observation of the K and Cs (3×1) reconstruction obtained upon a 300°C annealing of the AM/Si surface obtained upon alkali deposition at RT [36]. After annealing to higher temperatures, a significant increase in the adsorbate-substrate distance was detected. The collected evidence favors occupation of on-top sites (A, Atop) at these very low coverages.

Theoretical studies by Rodrigues [51] and Erwin [52] made an attempt to explain these experimental observations and to give a comprehensive analysis of the system. Rodrigues [51] studied the nature of the AM-Si bond performing an ab initio all-electron cluster model calculation of the absorption of alkali metals on the Si(111) surface. For the equilibrium Rb-Si distance, a value of 3.50 Å has been found. This result is consistent with the sum of atomic radii interpolated using the covalent and ionic radii and the actual atomic charges found in the calculation. The binding energy for Rb is 1.43 eV. The population analysis shows a picture of a highly ionic bond, with Mulliken charge on the metal of 0.94 electrons per bond. The AM-Si bond populations decrease steadily from Li (0.32 e-) to Rb (0.06 e-). Nevertheless, one must be very careful to avoid interpreting these results as a simple ionic bond whose ionic character grows in going from Li to Rb. From the analysis of the charge density-change maps a complex charge distribution exhibits the richness in the nature of the bond. Rb shows an appreciable polarization, and the associated dipole moments align with the dipole moment of the surface, partly originated by the presence of the sp^3 dangling bonds. In the case of Rb, a counter-polarization of the core and semi-core p orbitals is also evident from the changes

in the charge density and is attributed to the Coulomb repulsion with the polarized valence states. In all cases, the last occupied molecular orbital shows a significant participation of the adsorbate valence states. For Rb the mixing with the valence p states that give rise to the polarization is clear. These facts emphasize the presence of some degree of covalency in the bond.

Erwin [52] studied the (3×1) reconstruction induced by the alkalies on the Si(111)-(7×7) surface and proposed a model to explain the geometry as well as the accumulated evidence. Erwin proposed an extended Pandey chain model. This model can best be described as an extension of Pandey's π-bonded chain model, which is widely accepted as the atomic geometry of the clean Si(111)-(2×1) reconstruction [53]. The (2×1) Pandey model consists of alternating seven-member and five-member rings (...757575...). The metal:3×1 extension of this model simply inserts a six-member ring into this sequence (...765765...), as shown in Fig. 2.8.

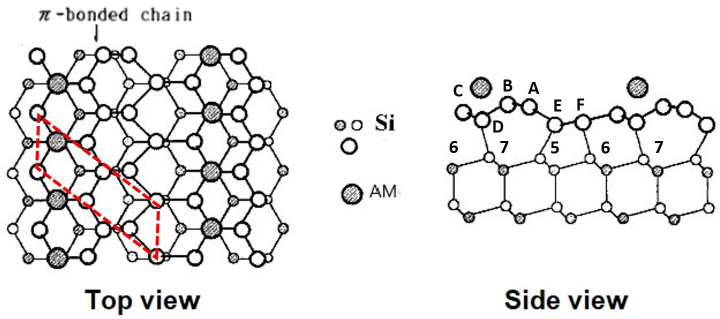

Figure 2.8: Top and side view of the fully relaxed geometry for the extended Pandey chain model for the AM/Si(111)-(3×1) structure. The (3×1) unit cell is highlighted in red. The model suggests an alkali coverage of 1/3 ML. From Ref. [52]

First principle total energy calculations (making use of LDA) for several alkali adsorbates (including Rb) showed this model to be more stable than other previously proposed models. The results from the computational data can be summarized as following. The model suggests an alkali coverage of 1/3 ML. The role of the adsorbate is primarly that of an electron donor and dangling-bond passifier. The ionically bound adsorbate strongly perturbs the surface geometry and electronic dispersion; all the alkalies considered in this study are found to behave in a very similar fashion, irrespective of their size. The calculated energy gap (for Rb equal to 0.37 eV, this is usually an underestimation due to the use of LDA), surface state dispersion, and simulated STM images are in good agreement with the accumulated experimental evidence. The filled state images show a double row of equilateral triangular spots, which arise from the occupied surface states associated with the two highest silicon atoms.

The surface electronic structure of the Rb(3×1) was studied by means of Core Level Spectroscopy (CLS) [39]. The high resolution surface Si 2p core level spectrum of the Rb/Si(111)-(3×1) surface was fitted well with one bulk and three surface components as shown in Fig. 2.9. Here two of the three surface states are shifted to lower binding energies (E_B's). The estimated number of the surface atoms corresponding to these three surface components are 2, 1.6 and 1.33 for S_1, S_2, and S_3 respectively. This means that in the unit cell there are about 2, 1 (or 2), and 2 (or 1) surface silicon atoms which are positively-, negatively-, and slightly negatively charged. These results can be explained by the (...765765...) model (the extended Pandey's chain [52]) if the S_2 component is assigned to electrons from 'B' and 'C' atoms (ref. Fig. 2.8) which are negatively charged, the S_1 component to those from 'A' and other atoms which are positively charged, and the S_3 component to those from bulk-like

'D', 'E' or 'F' atoms which may be slightly negatively charged (see Fig. 2.8).

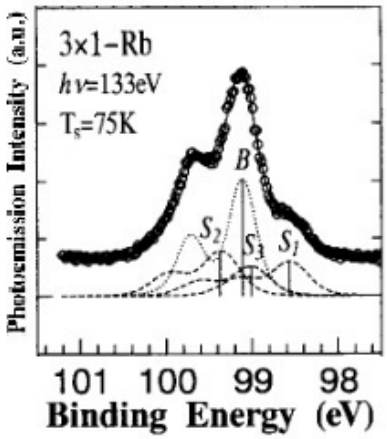

Figure 2.9: Si 2p core level spectra of Rb(3×1). Empty circles are the experimental data. From the curve fitting, one bulk (B) and three surface (S_1, S_2 and S_3) components are deconvoluted. From Ref. [39].

In addition to the Si 2p core level, also the core level spectrum of Rb 4p was measured (figure omitted in the paper). The observed Rb 4p core level spectra showed a simple spectral shape without any shifted components. These results indicate a single adsorbate site on these surfaces and are consistent with the 1/3 ML coverage.

Chapter 3

Experimental Methods

In this chapter, the experimental methods and apparatus used to perform this investigation are presented and described. The whole investigation has been performed in an ultra-high vacuum system (section 3.1). The equipment used for the experiments is directly mounted on the vacuum chamber. Low energy electron diffraction and scanning tunneling microscopy, both used to characterize the surface and the quality of the samples, are described in sections 3.2 and 3.3, respectively. The sample holder is described in section 3.4. Then, section 3.5 is dedicated to the Rb evaporator. The evaporation rate has been monitored using a Residual Gas Analyzer (RGA). This is described in section 3.6.

3.1 Ultra-high vacuum (UHV)

Many surface analysis techniques would not be possible without a clean UHV environment. Analysis techniques require high purity over a sustained analysis time and thus are prime candidates for UHV. All measurements presented in this thesis are performed in an ultra high vacuum environment.

3.1.1 UHV Conditions

In order to investigate a solid surface on the atomic scale, the interactions between the surface and species from the environment should be low to avoid contamination. The latter can change the surface conditions. This means that such experiments should be conducted in vacuum.

Vacuum is primarily measured by its absolute pressure, but a complete characterization requires further parameters. Common parameters that allow an understanding of the vacuum concept are molecular density, mean free path, and time constant to form a monolayer [2].

From the kinetic theory of gases [2], the flux I of gas molecules impacting on a surface from the gas phase (one of the factors determining how long a surface can be maintained clean) reads

$$I = \frac{p}{\sqrt{2\pi m k_B T}} \tag{3.1}$$

where p, m, k_B and T indicate respectively pressure, mass, Boltzmann's constant, and temperature. From this equation one can easily obtain the molecular density n (number of molecules per volume unit):

$$n = \frac{p}{k_B T} \tag{3.2}$$

The mean free path λ, i.e. the average distance that a particle (atom, electron, molecule) travels in the gas phase between collisions, can be written as [2]

$$\lambda = \frac{k_B T}{\pi p \sigma}, \tag{3.3}$$

where σ is the particle scattering cross-section. The time constant to form a monolayer, i.e. how long it will take for a clean surface to become covered by a monolayer from the gas phase, is:

$$\tau = \frac{n_0}{I} = \frac{n_0 \sqrt{2\pi m k_B T}}{p} \tag{3.4}$$

with n_0 the number of atoms in a monolayer (number of surface atoms of the investigated surface).

Once the pressure in a vacuum system has reached high vacuum levels, most gas particles reside on the walls of the system. Thus, at high vacuum and ultrahigh vacuum levels, the pressure in the system is determined by the equilibrium between the adsorption and desorption of gas particles on the surfaces of the chamber walls. Looking at Table 3.1 one can see that with a gas pressure of $1.3 \cdot 10^{-6}$ mbar it only takes 2.2 seconds to create a monolayer of gas on the sample, while at $1.3 \cdot 10^{-12}$ mbar it will take 25 days, explaining the reason of UHV environment for surface analysis techniques.

Vacuum level	p (mbar)	n (cm^{-3})	λ (cm)	τ (s)
Rough	10^3	$2.5 \cdot 10^{19}$	$6.7 \cdot 10^{-6}$	$2.9 \cdot 10^{-9}$
$> 10^{-3}$ mbar	1.3	$3.3 \cdot 10^{16}$	$5.1 \cdot 10^{-3}$	$2.2 \cdot 10^{-6}$
High	$1.3 \cdot 10^{-3}$	$3.3 \cdot 10^{13}$	5.1	$2.2 \cdot 10^{-3}$
($10^{-3}$$10^{-9}$) mbar	$1.3 \cdot 10^{-6}$	$3.3 \cdot 10^{10}$	$5.1 \cdot 10^{3}$	2.2
Ultra high	$1.3 \cdot 10^{-9}$	$3.3 \cdot 10^{7}$	$5.1 \cdot 10^{6}$	$2.2 \cdot 10^{3}$
$< 10^{-9}$ mbar	$1.3 \cdot 10^{-12}$	$3.3 \cdot 10^{4}$	$5.1 \cdot 10^{9}$	$2.2 \cdot 10^{6}$

Table 3.1: Useful vacuum parameters: pressure p, molecular density n, mean free path λ, and monolayer formation time τ for different levels of vacuum. From Ref. [2].

3.1.2 UHV Technology

Ultra high vacuum systems demand the use of special materials of construction, such as 304 or 316 stainless steel, that have low gas permeability, ability to endure bakeout, and that are nonmagnetic and resistant to corrosion. Materials such as copper, aluminum, and refractory materials are commonly employed inside the vacuum vessel, e.g. in the construction of evaporator and sample holders. Instead, other materials such as pyrex and ceramics or teflon are used for the construction of window flanges and for electrical insulation inside the vacuum chamber. Moreover, in order to prevent any leakage in the UHV system, fittings and gaskets are used between components. Nearly all such fittings are ConFlat metal flanges, with knife-edges on both sides cutting into a soft gasket, typically copper. These all-metal seals can maintain integrity to UHV ranges [2].

To reach UHV conditions, the system needs to be *baked*, i.e. heated up to 150°C (this is the maximum rating for our RHK system). With this procedure one removes water and rest gas molecules which are generally adsorbed on the chamber walls. The vapor pressure trend of water is exponential with temperature, so that at room temperature water slowly desorbs from the chamber, and thus the time needed to pump it away is very long. The bakeout process accelerates this outgassing process.

In order to reach ultra high vacuum levels ($\sim 10^{-10} - 10^{-11}$ mbar) from atmospheric pressure (10^3 mbar), the pressure needs to be decreased by 13-14 orders of magnitude, and once UHV conditions are reached, they need to be maintained: this is achieved by a pumping system.

The ultra high vacuum level is reached by three steps of pumping, and to each step a particular type of pump is associated. In the first step, starting from atmospheric pressure, a rotary pump or a *scroll pump* is used to get rough vacuum (down to $10^{-2} - 10^{-3}$ mbar). The latter pump is most commonly used because it is oil free. The principle of operation of the scroll pump (see Fig. 3.1) is that the gas enters the inlet port and is trapped in between two interleaving scrolls, one of which is fixed, while the other orbits eccentrically without rotating. The gas is compressed by the motion of the eccentrically mounted motor and expelled into atmosphere through the exhaust discharge valve.

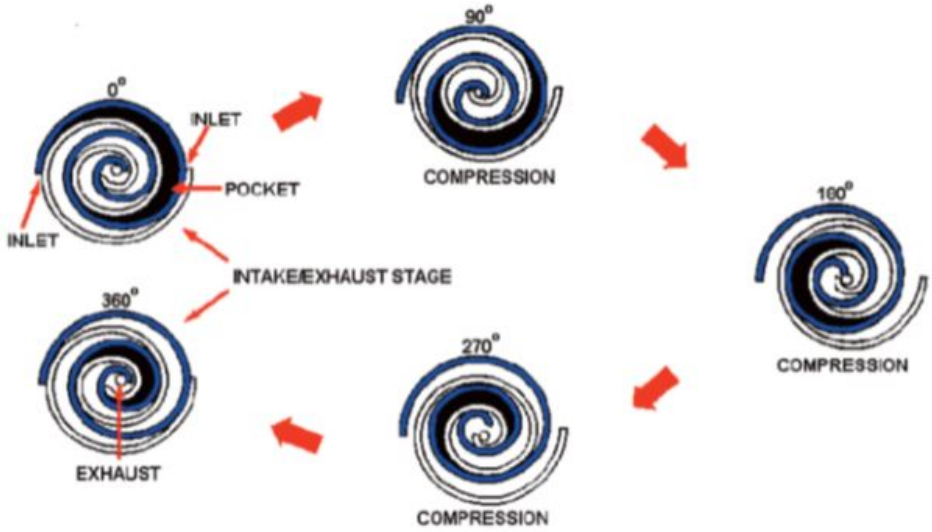

Figure 3.1: Principle of operation of a scroll pump. The gas enters from the inlet valve (left-up), is compressed while moving between the scrolls, and is finally exhausted from the pump (left-down). From Ref. [54].

The second step is high vacuum (down to 10^{-8} mbar), which is achieved employing a *turbomolecular pump* (see Fig. 3.2). The working principle of this pump is to transfer momentum in the direction out-of-the chamber to gas molecules by repeated collisions with a moving solid surface. In order to do this, a stack of rotors with multiple angled blades is rotated at very high speed. The pressure range in which this pump works corresponds to a molecule mean free path about some tens of meters (see Table 3.1). This means that the operation of the pump is based on a statistical process: each molecule present in the chamber has a certain probability in a certain time to be near the inlet. In this time instant, the molecule enters through the inlet and the rotor, which has a number of angled blades, hits the molecule. Thus the mechanical energy of the blades is transferred to the gas molecules. With this newly acquired momentum, the gas molecules enter into the gas transfer holes in the stator. This leads them to the next stage where they again collide with the rotor surface, and this process is continued, finally leading them outwards through the exhaust connected to the foreline. The performance of a turbomolecular pump is strongly related to the rotation frequency of the rotor. In fact, as rpm increases, the rotor blades deflect more. To increase speed and

reduce the deformation, stiffer materials and different blade designs have been suggested. In our case the operational frequency of the turbo is 1200 rpm.

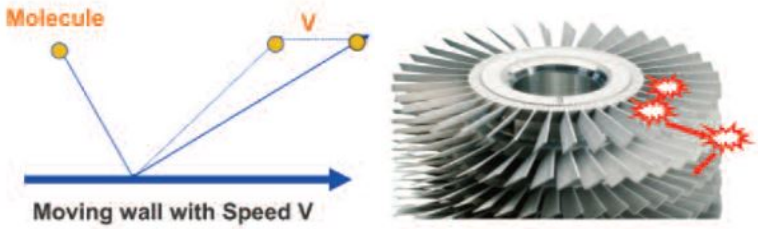

(a) (b)

Figure 3.2: Principle of operation of a turbomolecular pump. (a) Transfer of momentum to the gas particle in the direction of the stator holes. (b) Consecutive collisions with the blades lead particles outwards. From Ref. [54].

Ultra high vacuum (down to 10^{-11} mbar) is finally achieved using an *ion pump* (see Fig. 3.3). The configuration of an ion pump includes two plates made of Ti (that act as cathodes) mounted close to the open ends of short stainless steel tubes (that act as anodes). A high voltage is applied between the anode and the cathode, and a strong magnetic field parallel to the tubes axes. The pumping action works as follows: the gas present in the chamber is ionized, and the emitted electrons move along helical trajectories in the anodic tubes, due to the strong magnetic field present, causing ionization of other gas molecules. The ionized molecules are accelerated by the applied electric field and buried in the titanium, when striking the cathode. In this process, some Ti is also sputtered. The sputtered Ti coats the tubes, the cathode, and the pump walls. As a result of chemical reactions with the gas molecules, ion burial and neutral burial can be realized as possible pumping mechanisms. To note that this type of pump does not involve any mechanical movement of its parts, thus it does not produce any vibration on the STM structure.

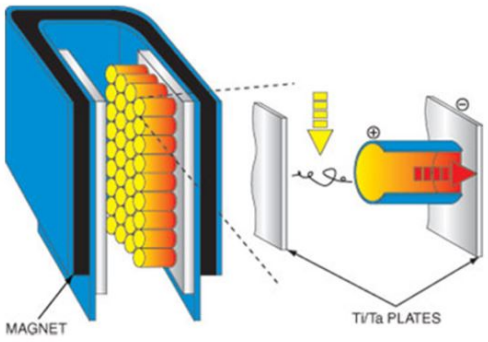

Figure 3.3: Principle of operation of an ion pump. The ionized atoms and molecules are accelerated and sputter Ti when striking the cathode. After chemical reaction with Ti, residual gas molecules are buried into the pump surfaces. From Ref. [54].

Commonly present in UHV systems, usually combined with ion pumps, are *Titanium Sublimation Pumps* (TSP). These pumps consist of a titanium filament through which a high current (typically about 40 A) is passed periodically. This current is enough to reach the titanium sublimation temperature, and hence the surrounding chamber walls become coated with a thin film of clean titanium. This Ti is reactive with the residual gas in the chamber which, colliding with the chamber wall, reacts to form stable and solid products. Thus, the gas pressure in the chamber is reduced. Because of the reactivity of Ti films, this procedure

is periodically repeated, in order to deposit new clean layers.

The UHV system used for this thesis (see Fig. 3.4) consists of three chambers: a fast-entry sample loading chamber (Load Lock, LL), a preparation chamber, and the STM chamber. The load lock is a small chamber used for loading and removing samples and tips, without venting the entire system. This chamber is pumped by a turbomolecular pump connected to a scroll pump, down to $\sim 10^{-8}$ mbar, and is separated from the preparation chamber by a manual gate valve. The prep chamber is maintained at $\sim 10^{-10}$ mbar using an ion pump. Communication between two environments at different pressures (10^{-8} and 10^{-10} mbar) does not perturb the UHV too much. Indeed, the mean free path at 10^{-8} mbar is greater than the LL dimensions, therefore the gas transfer between LL and preparation chamber is only ballistic. The preparation chamber is equipped with a mass spectrometer (RGA), a metal evaporator, low energy electron diffraction (LEED), Auger electron spectroscopy (AES), and a thermal hydrogen cracker. Meanwhile, the STM chamber is separated from the preparation chamber by another manual gate valve, and pumped down to a pressure of the order of 10^{-11} mbar, using a second ion pump. This chamber contains solely the STM. Both the preparation and the STM chambers also have titanium sublimation pumps.

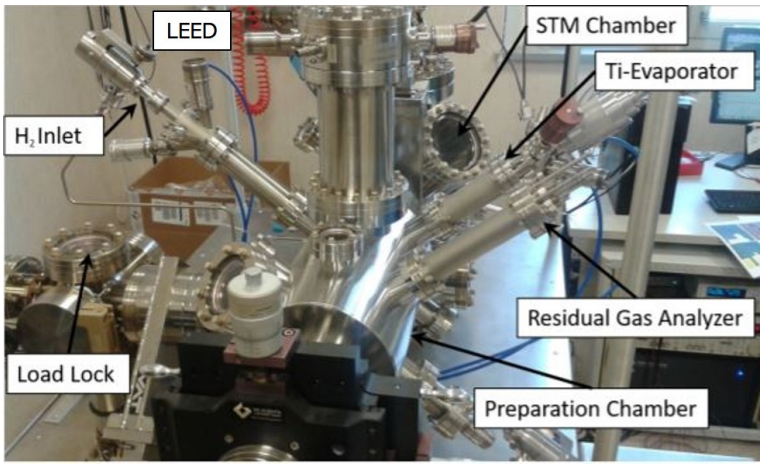

Figure 3.4: Photo of the RHK system, showing the three vacuum chambers and the fitted instruments.

3.2 Low Energy Electron diffraction (LEED)

Electron diffraction techniques are widely used to investigate surface structures. Structural information can be obtained analyzing the particles/waves elastically scattered by the crystal. The intensity of the diffracted electron beam gives information on the atomic arrangement inside a unit cell, while the spatial distribution of the diffracted beam provides information about the crystal lattice.

Low-Enegy Electron Diffraction (LEED) is the most widely used technique for surface characterization. LEED is based on a collimated electron beam of low energy (20-200 eV), directed towards the sample surface, that produces a pattern of diffracted electrons which are observed as spots on a fluorescent screen.

3.2.1 LEED Theory

The wave-particle duality of nature allows to consider an electron beam as a succession of electron waves. In a typical LEED experiment, these waves impinge normal on a surface.

The waves will be scattered by regions of high electron density, i.e. the surface atoms, which can therefore be considered to act as point scatterers. The wavelength of the electrons is given by the de Broglie relation,

$$\lambda = h/p \tag{3.5}$$

where h is the Plank constant ($\sim 6.626 \times 10^{-34}$ m^{2}kg/s), and p is the electron momentum defined as $p = mv = \sqrt{2mE_k}$ where m is the electron mass ($\sim 9.11 \times 10^{-31}$ kg), v is their velocity ([m s^{-1}]), and E_k their kinetic energy ([eV]). Using the latter relation, one can equally write the electron wavelength as:

$$\lambda = \frac{h}{\sqrt{2mE_k}} \quad \Rightarrow \quad \lambda[\text{Å}] = \frac{12.264}{\sqrt{E_k([\text{eV}])}} \tag{3.6}$$

Therefore, in the typical energy range used in LEED ($20-200$ eV) the electrons have a wavelength of $1-2$ Å comparable with interatomic spacings, which is the necessary condition to observe the diffraction effects associated with an atomic structure.

Due to the strong interaction with the surface atoms, the electrons are subject to diffraction phenomena. If the surface is well-ordered (crystalline), it will act like a diffraction grating, giving intense diffraction maxima in certain directions, whereas no intensity is observed for other directions.

In crystals, i.e. in periodic systems, the condition of elastic scattering is satisfied only in correspondence to reciprocal lattice vectors [20]. This condition is called Laue condition and means that occurrence of diffraction peaks requires

$$\mathbf{Q} \equiv \mathbf{k}_i - \mathbf{k}_f = \mathbf{G} \tag{3.7}$$

where $\mathbf{Q}$ is the scattering vector defined as $\mathbf{k}_i - \mathbf{k}_f$, $\mathbf{k_i}$ the incident wave vector, $\mathbf{k_f}$ the diffracted wave vector, and $\mathbf{G}$ is a reciprocal lattice vector. It follows, the necessary condition for diffraction is that the difference between the incident and the scattered radiation wavevectors equals a reciprocal lattice vector. Eq. 3.7 can be rewritten as

$$\hbar\mathbf{k}_i = \hbar\mathbf{k}_f + \hbar\mathbf{G} \tag{3.8}$$

Bragg considered specular reflection of the incident radiation by a family of lattice planes; as illustrated in Figure 3.5, the geometrical condition for the coherent scattering from two successive planes (and hence from the whole sequence of parallel planes) requires:

$$2d\sin\theta = n\lambda \tag{3.9}$$

where n is a positive integer, λ is the wavelength of the scattered (and incident) wave, θ is the scattering angle, and d is the distance between adjacent planes.

Figure 3.5 also shows the geometrical construction of the vector $\mathbf{Q} = \mathbf{k}_i - \mathbf{k}_f$. Since for elastic scattering $|\mathbf{k}_i| = |\mathbf{k}_f| = 2\pi/\lambda$, we have:

$$|\mathbf{Q}| = 2|\mathbf{k}_i|\sin\theta = 2\frac{2\pi}{\lambda}\sin\theta = n\frac{2\pi}{d} \tag{3.10}$$

where the last equality follows from Bragg's law (Eq. 3.9). From Fig. 3.5 it is seen that for specular reflection $\mathbf{Q}$ is perpendicular to the family of lattice planes with distance d; furthermore, equation 3.10 shows that the magnitude $|\mathbf{Q}|$ is an integer multiple of the quantity $2\pi/d$; these two observations (together with the general properties of real and reciprocal spaces) allow one to conclude that $\mathbf{Q}$ must be a reciprocal lattice vector.

In conclusion, in the case of specular reflection the Laue condition (Eq. 3.7) for occurrence of diffracted beams is fully equivalent to the Bragg condition (Eq. 3.9) for occurrence of reflected beams, and the expressions diffracted beam and reflected beam in this context become synonymous. From the Bragg condition (Eq. 3.9), the possibility of elastic scattering occurs only if $\lambda < 2d$. Thus λ must be of the order of an Å or less. Furthermore, λ cannot be much smaller than the interatomic distance, otherwise experimental arrangements at glancing angles would be necessary to detect diffraction peaks with small momentum transfer.

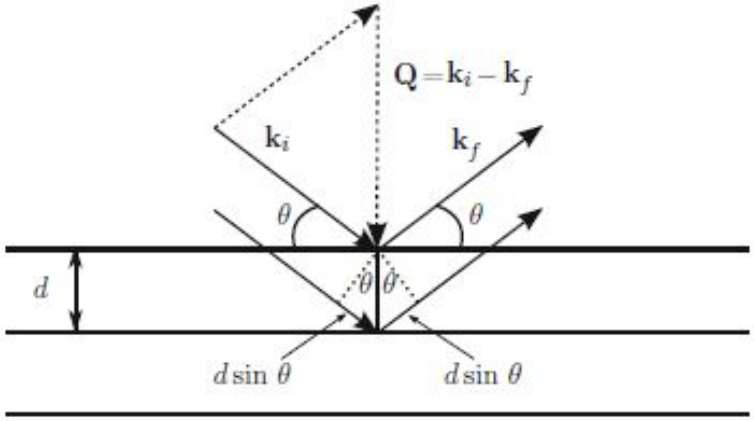

Figure 3.5: Waves reflected from successive planes constructively interfere if $2d\sin\theta$ equals an integer number $n\lambda$ of wavelengths. The geometrical construction of $\mathbf{Q} = \mathbf{k}_i - \mathbf{k}_f$ is also provided. From Ref. [20].

3.2.2 Ewald construction

It is also possible to consider the following geometrical construction due to Ewald for an easy determination of the occurrence of (elastic) diffraction peaks.

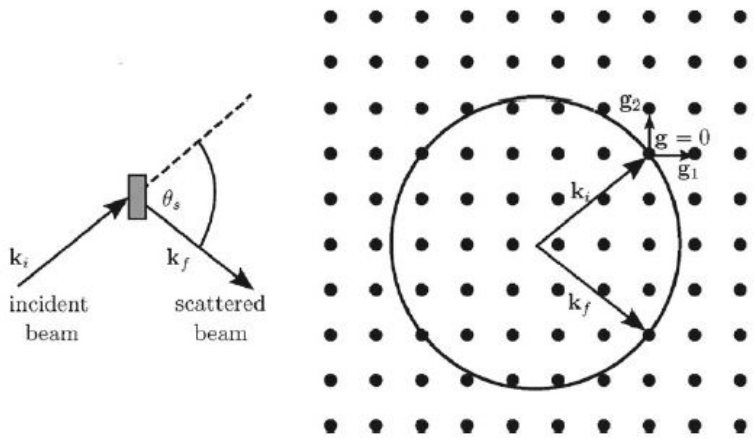

Figure 3.6: Ewald construction in the reciprocal lattice (supposed cubic for simplicity) of allowed wavevectors for elastic diffraction. From Ref. [20].

Suppose to have an incident monochromatic beam of particles of wavevector $\mathbf{k}_i$ and a diffracted beam with propagation wavevector $\mathbf{k}_f$. For elastic scattering, the conservation of energy and the conservation of momentum (within reciprocal lattice vectors $\mathbf{G}$ times $\hbar$) imply:

$$|\mathbf{k}_i| = |\mathbf{k}_f| \text{ and } \mathbf{k}_i = \mathbf{k}_f + \mathbf{G} \tag{3.11}$$

The Ewald construction (see Fig. 3.6) permits a simple geometrical interpretation of Eq. 3.11. In reciprocal space, the vector $\mathbf{k}_i$ is drawn in such a way that its tip terminates at the reciprocal lattice vector $\mathbf{G} = 0$. With the center at the origin of the vector $\mathbf{k}_i$, a sphere of radius $\mathbf{k}_f$ is drawn; if this sphere intersects, besides $\mathbf{G} = 0$, one (or more) points of the reciprocal lattice, conditions (3.11) are satisfied and elastic diffraction is observed. It is evident that diffraction may only occur if the length of $\mathbf{k}_i$ exceeds one half of the length of the smallest (non-vanishing) $\mathbf{G}$ vector.

In LEED, most of the information regards the very top layer of the sample, i.e. the 2D atomic structure of the sample surface, since the energies of the incident beam allow the electrons to penetrate at most few atomic layers. The Ewald construction for diffraction on a 2D lattice is shown in Fig. 3.7

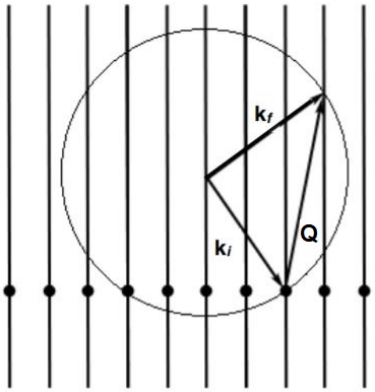

Figure 3.7: Ewald construction for diffraction on a 2D surface lattice.

The reciprocal lattice rods, also called crystal truncation rods (CTR), perpendicular to the surface are related to the 2D reciprocal lattice points. To explain this, a 2D lattice can be imagined as a 3D lattice with infinite periodicity in the normal direction. Therefore, the reciprocal periodicity tends to zero, and the reciprocal lattice points along the normal direction are infinitely dense, forming rods. For the Ewald construction, again the incident wave vector $\mathbf{k}_i$ is placed such that it terminates at a reciprocal lattice point. With its center at the origin of the vector $\mathbf{k}_i$, a circle of radius $\mathbf{k}_f$ is drawn. The intercepts of the rods with this Ewald circle define the scattered wave vectors $\mathbf{k}_f$ for diffracted beams.

In the case of diffraction from a 2D surface, the law of conservation of the momentum becomes:

$$k_i^{||} - k_f^{||} = G_{hk} \tag{3.12}$$

In this case, only the components parallel to the surface are involved in the law of conservation of the momentum, and therefore the scattering vectors parallel to the surface ($k_i^{||} - k_f^{||}$) must be equal to the vector of the 2D surface reciprocal lattice, $G_{hk} = h\mathbf{a}^* + k\mathbf{b}^*$ ($\mathbf{a}^*$ and $\mathbf{b}^*$ are the primitive translation vectors of the reciprocal net).

3.2.3 LEED Setup

A typical LEED setup is shown in Fig. 3.8. This system sends an electron beam normal to the surface of the sample, which is at the center of a transparent hemispherical fluorescent screen. The electron gun consists of a heated cathode filament with a Wehnelt cylinder and a set of focusing lenses which send a focused electron beam at low energies. The electrons impinge on the sample surface and diffract in different directions depending on the surface crystal order. Once diffracted, they travel to the fluorescent screen. Before colliding with

the screen, they must pass through four different grids (known as retarding grids), which contain a central hole through which the electron gun is inserted. The first grid is nearest to the sample and grounded, as is the sample. A negative potential is applied to the second and third grids, which act as suppressor grids, given that they repel all electrons originating from non-elastic processes. These grids therefore perform as energy high-pass filter. The fourth grid is grounded and screens the fluorescent screen, which is biased to a high voltage of about +5 kV to accelerate the electrons so that they can excite it. This allows to visualize the diffraction pattern. The diffraction patterns generated on the fluorescent screen is then acquired by a CCD camera, connected to a PC which allows their direct observation on the monitor.

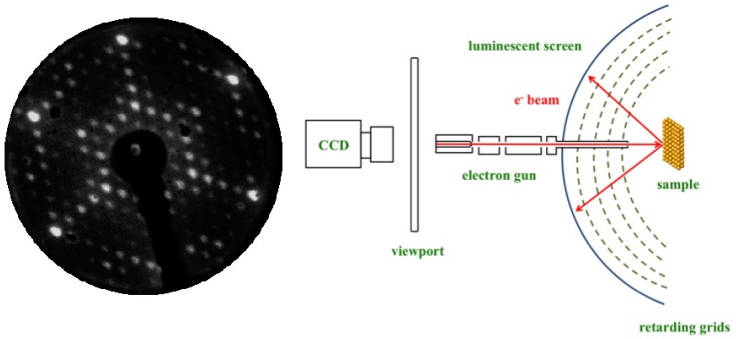

Figure 3.8: Right, schematic diagram of a typical LEED instrument and left, LEED pattern of a Si(111)-7 $\times$ 7 surface (Energy: 32.5 eV) viewed by the CCD camera. Adapted from Ref. [55].

The LEED patterns presented in this thesis have been taken in the same experimental conditions. In particular we choose 600 ms as integration time for the CCD. In the following the as acquired LEED patterns are shown either in B/W or W/B without altering the original colorscale, they will be addressed as raw LEED patterns. Otherwise, the set of LEED patterns has been subject to a uniform rescalation of the colorbar.

3.3 Scanning Tunneling Microscopy (STM)

The Scanning Tunnelling Microscope (STM) was developed by Binnig and Rohrer in 1981, instrument for which they were awarded the 1986 Nobel Prize in physics. The STM was the instrument used to generate the real-space images of the (7×7) silicon surface with atomic resolution (in the scale of Å). The basic principle of the STM is to take advantage of tunneling electrons to create a map of the density of the states of a surface at a given energy. When a metal tip is brought close to the surface and a bias voltage is applied between them, electrons can pass from the tip to the sample or vice versa through the vacuum by so-called quantum tunnelling. The gap between tip and sample behaves as a barrier for the electrons. When this gap is small enough, electrons can pass through this barrier. This would not occur according to classical mechanics, but it can take place with a non vanishing probability in quantum mechanics. The resulting tunnelling current depends on the distance between tip and surface, the local density of states (LDOS) of the sample, and the applied voltage.

3.3.1 Theory

A brief description of tunneling through a one-dimensional potential barrier will help to understand the basic concept on which STM relies [56]. In classical mechanics, an electron

with energy E, moving in z-direction under a potential $U(z)$ can be described by:

$$E = \frac{p_z^2}{2m} + U(z) \tag{3.13}$$

where m is the electron mass and p_z the momentum in the direction of the motion. In regions where $E > U(z)$ the electron has a momentum $p_z \neq 0$. On the contrary, in regions in which $E < U(z)$, the electron cannot penetrate the potential barrier described by $U(z)$.

In quantum mechanics, the same electron is described by a wavefunction $\psi(z)$, which satisfies the Schrödinger equation,

$$E\psi(z) = -\frac{\hbar^2}{2m}\frac{d^2}{dz^2}\psi(z) + U(z)\psi(z) \tag{3.14}$$

Consider the case of a piecewise-constant potential, as shown in Fig. 3.9. In the classically allowed regions, where $E > U$, the solution of the Schrödinger equation is:

$$\psi(z) = \psi(0)e^{\pm ikz}, \text{ where } k = \frac{\sqrt{2m(E-U)}}{\hbar} \text{ is the wave vector.} \tag{3.15}$$

The electron is moving (in either a positive or negative direction) with a constant momentum $p_z = \hbar k = \sqrt{2m(E-U)}$, or a constant velocity $v_z = p_z/m$, the same as in the classical case. In the classically forbidden region, equation 3.14 has the solution:

$$\psi(z) = \psi(0)e^{\pm \kappa z}, \text{ where } \kappa = \frac{\sqrt{2m(U-E)}}{\hbar} \text{ is the decay constant.} \tag{3.16}$$

The equation with the $-$ describes a state of the electron decaying in the $+z$ direction. The other solution with $+$ describes an electron state decaying in the $-z$ direction, indicating that the tunneling is bidirectional. Knowing the wave function one can calculate the probability density for that electron to be found at some location. The probability density to observe an electron at z is proportional to $|\psi(0)|^2 e^{-2\kappa z}$, which has a non-zero value in the barrier region, and thus the electron has a non-zero probability to penetrate the barrier.

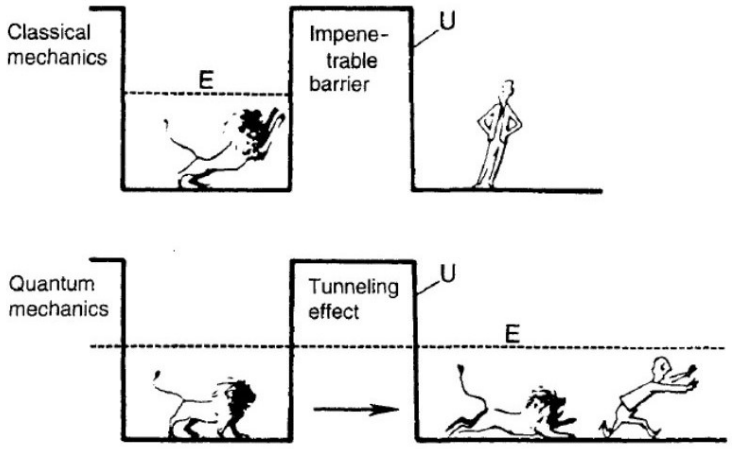

Figure 3.9: Difference between classical and quantum theory. In quantum mechanics, an electron has a nonzero probability of tunneling through a potential barrier. Image from Ref. [2].

Tunneling occurs when the tip and sample wave functions overlap, that is when under a bias there is some finite probability for the electron to cross the barrier and pass from the tip to the sample, or vice-versa. Let us assume that the bias is V_b and the barrier width, i.e. the

distance between the tip and the sample, is d. The probability P that an electron at $z = 0$ (at the sample surface) and in the state ψ_n can be found at $z = d$ (at the tip surface) is proportional to the wave function squared,

$$P \propto |\psi_n(0)|^2 e^{-2\kappa d} \tag{3.17}$$

Equation 3.17 also shows that the tunneling current depends exponentially on the tip-sample distance (in typical STM measurement this distance is of the order of 10 Å).

The work function ϕ of the surface represents the minimum energy needed to extract an electron from the Fermi level, the highest occupied level, to the vacuum level. If the bias V_b is small ($eV_b \ll \phi$), we can consider $U - E \approx \phi$. Then κ from Eq. 3.16 takes the form

$$\kappa = \frac{\sqrt{2m\phi}}{\hbar} \tag{3.18}$$

and represents the decay constant of a sample state near the Fermi level in the barrier region. In this condition, only electronic states very close to the Fermi level, within eV_b, are excited and can tunnel across the barrier (Fig. 3.10).

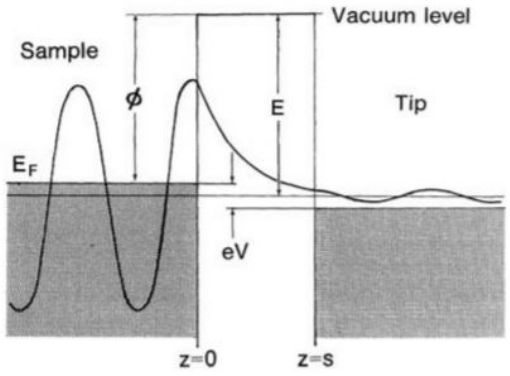

Figure 3.10: One-dimensional metal-vacuum-metal tunneling. The sample, left, and the tip, right, are modeled as semi-infinite pieces of free-electron metal. From Ref. [2].

One can also estimate the value of κ in a typical STM measurent. ϕ is usually around 4 eV, thus κ results to be:

$$\kappa = 0.51\sqrt{\phi(eV)}\ \text{Å}^{-1} \approx 1\ \text{Å}^{-1} \tag{3.19}$$

This means that with a distance increase of 1 Å the tunneling current decreases by a factor e^2, which is about one order of magnitude.

Another way of describing electron tunneling comes from Bardeen's approach which makes use of time-dependent perturbation theory. In the first approximation of the Bardeen formalism, the tunneling current results:

$$I = \frac{2\pi e}{\hbar} \sum_{\mu\nu} f(E_\mu)[1 - f(E_\nu + eV_b)]|M_{\mu\nu}|^2 \delta(E_\mu - E_\nu), \tag{3.20}$$

where $f(E)$ is the Fermi function, $M_{\mu\nu}$ is the tunneling matrix between tip and sample, and V_b the bias voltage applied between tip and sample (μ and ν refers to tip and sample, respectively). The tunneling current is a result of all tunneling events between the occupied states of the tip $f(E_\mu)$ and the unoccupied states of the sample in the energy range from E_ν to $E_\nu + eV$. If the bias voltage polarity is reversed, the occupied and unoccupied states as defined above are inverted, as well.

It is possible to use the STM in spectroscopy mode. In scanning tunneling spectroscopy (STS), the aim is to measure the density of states of the sample. This is accomplished by measuring the current-to-voltage characteristics of the tunneling junction [57].

In the simplest approximation, the density of states of the tip and the transmission factor of the barrier are considered to be voltage independent. Hence the differential conductance is proportional to the energy dependent density of states of the sample

$$\frac{dI}{dV} \propto \rho_{sample}(\mathrm{eV}). \tag{3.21}$$

In this approximation, the differential conductance dI/dV measures the sample density of states at the energy eV relative to the Fermi energy of the sample [57].

3.3.2 STM Setup

The essential components of an STM include a sharp probing tip; a piezoelectric scanning unit, which controls the vertical and lateral movement of the tip; a coarse positioning unit, which brings the tip-sample separation to within the tunneling range ($\sim$ Å); a vibration isolation stage; and a set of electronics, which detects the small tunneling current ($\sim$ 10 pA - 1 nA), controls the piezo-tube scanner via a feedback loop, and drives the coarse positioning.

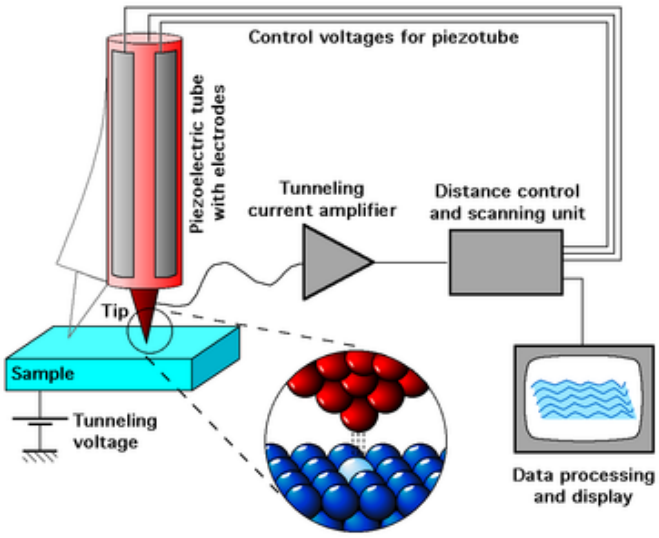

Figure 3.11: Schematic view of an STM. From Ref. [57].

The probe tips are normally made from tungsten (as in our case), platinum-iridium, or gold. The tip apex is very sharp, ideally made of a single atom. A tube piezo element, or tube scanner, moves the probe tip on the sample in order to scan the sample surface. The tube scanner allows the motion in three orthogonal directions. It consists of a tube, made of piezo-ceramics poled in radial direction, which is covered inside and outside with metal electrodes. A motion in z-direction can be achieved by applying a voltage between the inner and the outer electrodes, while a deflection in xy-direction is induced by voltages of opposite polarity applied to the two opposite outer electrodes.

Thus, moving the tip in the z direction and applying a bias voltage, the tunneling condition can be established. Instead, moving the tip across the sample in the $x-y$ plane, the changes

in surface height and density of states cause changes in current, which is mapped in images. Finally, the current is amplified and the data are processed and shown on the computer.

There are two modes of operation (i.e. constant current and constant height) for STM imaging. In constant current mode, feedback electronics adjusts the height of the tip by a voltage to the piezoelectric height control mechanism. The height of the sample changes (mountains and valleys) but the feedback maintains the distance between tip and sample constant, thus the tunneling current stays constant. This mode is frequently used in STM imaging because the height of surface features can be precisely derived from the feedback voltage and sensitivity of the piezoelectric driver element. In constant height mode, the height of the tip and the voltage are constant but the tunneling current changes as the tip scans the surface because the distance between tip and sample changes when the sample is not perfectly flat. In this mode the feedback is turned off. This mode allows faster imaging of atomically flat surfaces. All STM images presented in this thesis have been taken in constant current imaging mode.

It should be mentioned that STM gathers information about the surface from the magnitude of the tunneling current, which is sensitive not only to surface topography, but also to the local density of electron/hole (or "filled" and "empty") surface states. So the STM image is a convolution of both topographical and electronic information.

An STS spectrum (differential conductance) is acquired using the following method. The tip is positioned over a certain desired lateral position of the surface at a certain voltage and a certain current (usually called stabilization voltage and stabilization current). For a specific density of states these conditions define a certain tip-sample distance. Then the feedback loop is disabled (leaving the tip-sample distance constant during spectroscopy) and the dI/dV signal is recorded over the desired range of voltages [57].

The primary measured signal is the current I as a function of the voltage V: $I = f(V)$. In the following, we show how a modulation technique (lock-in technique) is used in order to measure directly the derivative signal dI/dV as a function of the voltage. While generically STM is not an AC technique, in STS a small modulation voltage $V_M cos(\omega t)$ is added to the applied bias voltage $V = V_{dc} + V_{ac} = V_{dc} + V_M cos(\omega t)$. The measured modulated current will be

$$I(t) = f(V) + V_M cos(\omega t). \tag{3.22}$$

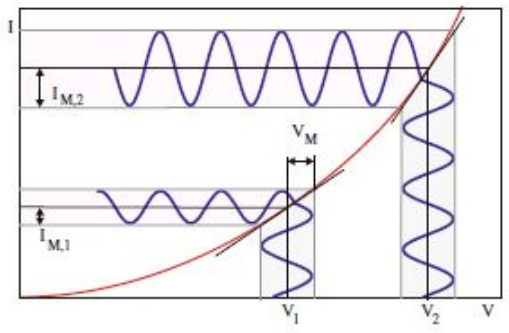

Figure 3.12: Graphical representation of the measurement of the first derivative (black lines) of the $I-V$ curve (red line). The voltage is modulated around a value V_1 or V_2. The measured amplitude of the resulting modulated (tunneling) current dI is proportional to the slope of the $I-V$ curve (dI/dV) at V_1 or V_2, respectively. From Ref. [57].

This signal can be detected by a lock-in amplifier, and its amplitude is for small modulation voltages proportional to dI/dV as can be inferred from Fig. 3.12, which shows a

hypothetical I-V curve. For the voltage V_1 the derivative (dI/dV) is small and for V_2 the derivative is larger. If now a modulation voltage is applied around a center voltage, as indicated by V_M, this will lead to a corresponding modulation of the measured tunneling current. Now, since dV is known, from a measure of dI the dI/dV curve can be readily obtained.

Measuring the derivative using the lock-in technique requires some effort. However, the numerical derivative of an I-V curve is much more noisy than the derivative obtained using the lock-in technique. Also smoothing of the numerically differentiated signal will not improve the signal recovery to the level achieved with the lock-in technique. Without the lock-in technique all signals are amplified, in the lock-in technique only the signal component at the modulation frequency and with a constant phase as the modulation frequency is selected.

During the STM acquisition, also the external conditions must be controlled. Indeed, to achieve atomic resolution, vibration isolation is essential. The STM unit must be as rigid as possible, and the transmission of environmental vibrations to the STM unit has to be reduced. The STM is usually placed on an optical table which allows isolation from ground vibrations. Vertical damping is achieved by the use of a dual chamber damped pneumatic spring. The scan occurs in floating conditions in vacuum, to reduce as much as possible the external noise. The STM sample stage includes a flange with an internal spring suspension system with eddy current dampening to further reduce transmission of vibrations.

The STM experiments can be performed in a variety of ambients: in air, in inert gas, in ultrahigh vacuum, or in liquids including insulating and cryogenic liquids, and even electrolytes. The operating temperature ranges from near absolute zero (-273 °C) for a low-temperature STM (LT-STM) to some hundred degrees centigrade (1000 °C) for a variable temperature STM (VT-STM). In our setup, the STM is a variable temperature (from 100 K to 1500 K) ultra high vacuum STM from RHK Technologies. In this thesis STM was only operated at room temperature.

3.4 Sample holder

The sample holder for inserting samples in the RHK system is shown in Fig. 3.13. It consists of a double grooved copper body, useful to clasp it in the sample stage and for its transfer, and a helical top ramp, which acts as base for the scan head during STM imaging, as shown in Fig. 3.13.

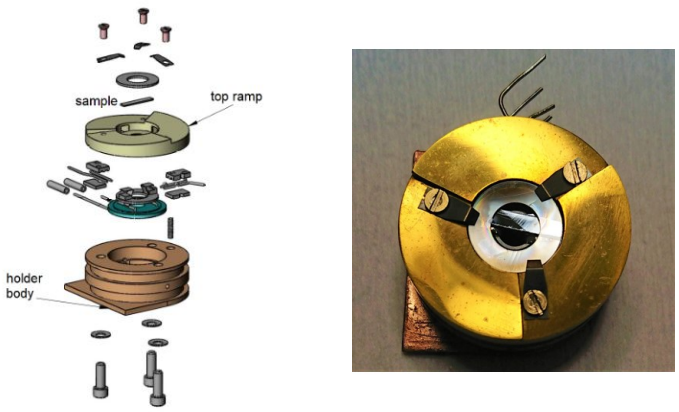

(a) **(b)**

Figure 3.13: (a) Scheme of the sample holder used for the RHK system. (b) Top view of a sample holder used for this thesis which has a rectangular cut Si(111) sample mounted in.

Round or squared flat samples (of maximum dimensions 7 mm $\times$ 7 mm) can be mounted in the holder, sandwiched between two sapphire washers in order to be electrically and thermally isolated from the body. In this thesis we performed a direct current heating of the sample by the use of tantalum foils, mounted at the bottom of the sample holder. The sample holder has a built-in thermocouple (TC) which measures the sample temperature. The two leads of the TC are made from Nickel alloys, precisely one of the leads is a wire of a Ni/Cr alloy, while the other lead is a wire of a Ni/(Al+Mn+Si) alloy. For electrical contact to the sample there are two more contacts (additional contacts) on the holder, which we have used for this thesis work.

For these experiments, the just cut silicon samples have been mounted on the sample holders where the TC has been removed. This operation has been done in order to avoid nickel contamination from the TC. Also the instruments used to handle and cut the Si were nickel-free in order to not contaminate any further the wafer surface. The sample temperature was measured with a pyrometer which has an estimated error on the relative temperature smaller than 5°C and on the absolute temperature of about $10 - 20$°C.

3.5 Rb Evaporator

Our Rubidium source is a commercially available alkali-metal dispenser (SAES Getters, model Rb/NF-FT 10+10). The alkali metal is stabilized as a salt and mixed with a zirconium alloy-based non-evaporable getter material. The mixture is then loaded into the dispenser structure. Our group has previously assembled and designed the evaporator on which the dispenser is mounted. A schematic of the parts of the dispenser is shown in Fig. 3.14.

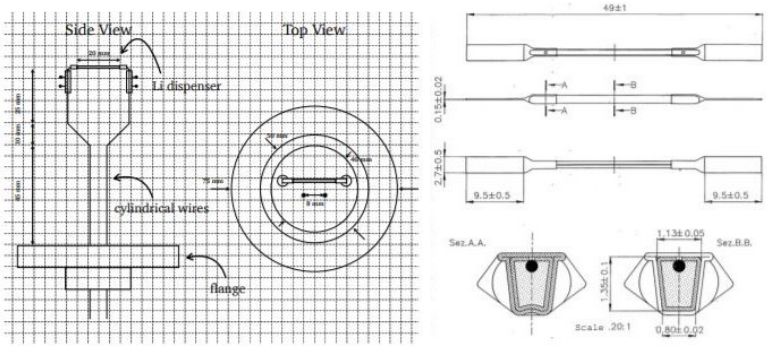

(a) **(b)**

Figure 3.14: Evaporator design and assembly (on the left), and Rb dispenser from SAES Getters utilized for the evaporations (on the right). (a) From Ref. [58], and (b) from Saes Getters AMD datasheet.

When the dispenser is heated (by resistive heating) in vacuum, alkali metal evaporates as the result of a reduction reaction between the alkali metal salt and the getter material. The getter alloy sorbs gases released during the decomposition of the alkali metal salt preventing them from escaping from the dispenser. A pure alkali metal vapor is thus emitted from the dispenser.

After exposure of the dispenser to air, a degassing step is required. This step is done for two main reasons: to clean the dispenser in order to avoid deposition of unknown and unwanted materials on the sample during the evaporation, but also because the dispenser needs to be 'activated' once placed in the UHV chamber. This is because the Rb dispensers come in closed, thus the Rb they contain is protected from the environment. Once annealed

in UHV, the dispenser opens. When a dispenser has not been exposed to air after a previous evaporation, it is not necessary to perform the outgassing process. The current through the dispenser can be increased to the current given in the specifications to start the evaporation (for Rb, $I_{act} = 5.3 \pm 0.2$ A). It is to underline that the current setting is proportional to the deposition rate during the evaporation process. The heating profiles shown in Fig. 3.15 are for an ideal case.

The degassing of the Rb dispenser has been performed in UHV conditions, heated up to 5.3 A for several minutes at $P < 3 \cdot 10^{-9}$ mbar.

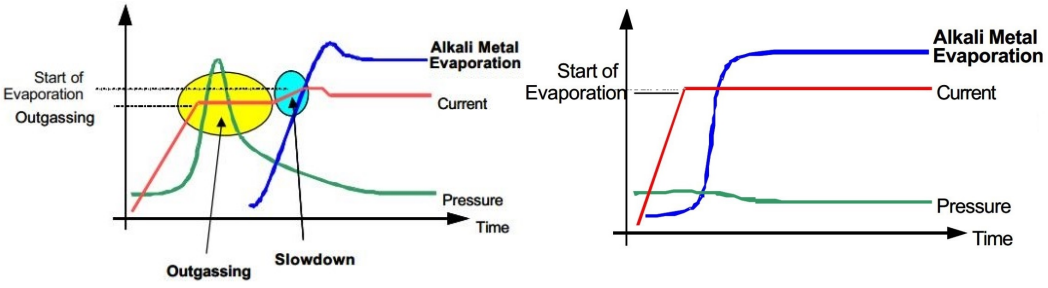

Figure 3.15: (a) Degassing and (b) evaporation process when the dispenser has already been outgassed. From Saes Getters, AMD datasheet.

3.6 Residual Gas Analyzer (RGA)

Complete characterization of a vacuum environment requires the detection of all component gases present, as well as measurement of the total pressure. The instrument used for this purpose is called Residual Gas Analyzer or Partial Pressure Analyzer. A Residual Gas Analyzer is a mass spectrometer of small physical dimensions that can be connected directly to a vacuum system and whose function is to analyze the gases inside the vacuum chamber. The principle of operation is based on the ionization of a small fraction of the gas molecules: the resulting ions are separated, detected and measured according to their mass/charge ratio. It is worth noting that the quadrupole mass filter must operate in a vacuum environment, at a pressure lower than 10^{-4} mbar, in order to avoid collisional scattering between the ions and the neutral gas molecules. RGA's are widely used to quickly identify the different molecules present in a gas environment and, when properly calibrated, can be used to determine the concentrations or absolute partial pressures of the components of a gas mixture.

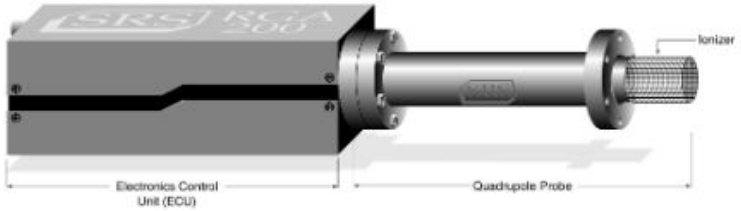

Figure 3.16: Scheme of the SRS Residual Gas Analyzer, composed of an Electronic Control Unit (ECU), connected to the PC, and a quadrupole probe.

We use an SRS RGA, shown in Fig. 3.16, which consists of a quadrupole probe and an Electronics Control Unit (ECU) which mounts directly on the probe flange and contains all the electronics necessary to operate the instrument.

The total probe equipment consists of three parts: the ionizer (electron impact), the quadrupole mass filter and the ion detector. All of these parts reside in the vacuum space where the gas analysis measurements are performed. The detector measures the ion currents directly, by the use of a Faraday Cup, or it can measure an electron signal proportional to the ion current by using an optional electron multiplier detector. However, when the pressure is lower than 10^{-7} mbar, as in our case, the Electron Multiplier upgrade is recommended.

The Multi-Channel Continuous Dynode Electron Multiplier (CDEM) consists of a conical system made out of a special resistive glass. When the cone is biased negatively relative to the back end, positive ions are very efficiently attracted and strike the cone at high velocity, producing electrons by secondary electron emission. This process continues, and depending on the bias voltage applied, up to 10^7 electrons come out at the back end from a single ion and are picked up by a grounded plate.

3.6.1 Use of the RGA in this thesis

In this thesis, the RGA has been used to monitor the evaporation rate of the Rb dispenser. By monitoring the partial pressure of Rb, measured by the RGA, the evaporation rate can be monitored as well. The partial pressure is proportional to the number of Rb atoms in the environment, thus the higher is the partial pressure, the higher is the evaporation rate.

We used the RGA in two modes, the Scan mode and the Leak detection mode. Scan mode provides a line graph representation of the acquired mass spectrum (partial pressure vs mass number). Scans can be single-shot, timed or taken continuously, and the mass span can be set by the operator. Leak detection mode monitors the partial pressure of a particular mass number (only integer mass numbers are allowed) over time.

In a typical deposition experiment, we start by choosing and setting the current for the direct heating of the SAES Rb evaporator. While heating the dispenser, we monitor the partial pressure of Rb that builds up in the preparation chamber using the RGA in Scan Mode. Figure 3.17a shows three different superimposed plots taken in Scan mode for different Rb evaporation rates (corresponding to different heating currents) that were used in this thesis.

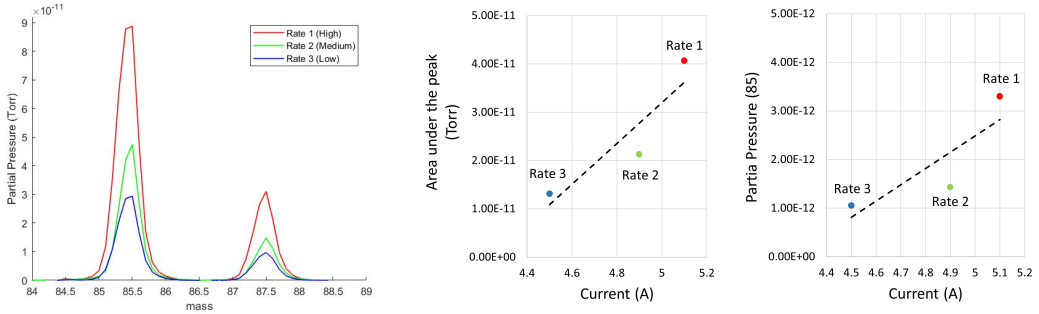

(a) **(b)** **(c)**

Figure 3.17: (a) RGA spectrum zoomed around the Rb isotope masses 85 and 87. The three different curves correspond to three different deposition rates. (b) Plot of the area under the fitted Gaussian curve around the mass 85 of the plots shown in (a) vs. the set direct heating currents of the evaporator. (c) Plot of the partial pressure at the mass 85 of the plots shown in (a) vs. the set direct heating currents of the evaporator. The dashed line are linear fits of the data points.

By analyzing the RGA scans shown in Fig. 3.17, two peaks around isotopic masses 85

and 87 can be identified. These peaks correspond to ^{85}Rb and ^{87}Rb, respectively. Theoretically the peaks should be delta function, but in practice there are many sources of broadening. By fitting the peaks with Gaussian functions, calculating the underlying area and plotting the results obtained as a function of the direct heating current of the evaporator that was set at the beginning of the experiment, we found what is shown in Fig. 3.17b. Fig. 3.17b clearly shows a linear dependence between the direct current heating and the Rb partial pressure measured in the preparation chamber. This linear relationship holds also for the single value of mass 85, as shown in Fig. 3.17c. Based on this, in the experimental sections I will refer to the evaporation rate as the Rb partial pressure in [Torr][1] measured in Leak detection mode (monitoring mass 85).

In general, once a current for the direct heating of the SAES Rb evaporator has been chosen and set, the evaporation rate takes around 20 minutes to reach equilibrium, thus the deposition conditions. The samples during this equilibration time were kept either with the bottom of the sample holder facing the dispenser or at distance. In order to monitor the evaporation rate and its constancy during evaporation, we monitored the mass 85 in Leak detection mode (as shown in Fig. 3.18).

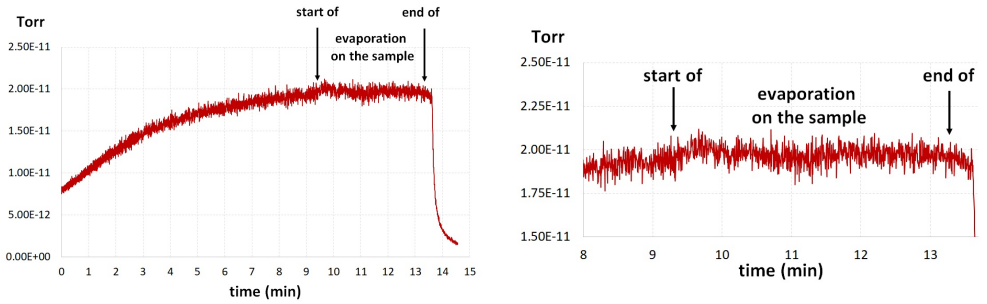

Figure 3.18: (a) Typical leak detection mode signal of mass 85 during Rb evaporation from the SAES dispenser. (b) Zoom-in in the evaporation region: the signal is on average constant. These plots show an evaporation of Rb for 4 minutes with a current of 4.9 A. The first few minutes of evaporation are excluded from the plot.

[1] In the cases in which RGA has not been used to monitor the partial pressure, the deposition rate will be described by the set direct heating current.

Chapter 4

Pristine Si(111)

This chapter outlines the preparation and the analysis of the Si(111)-(7×7) surfaces, used for this thesis work. The samples and the quality of their surface were readily first checked by LEED and then observed and characterized by STM.

As will be shown, the procedure we used was highly reproducible, and well ordered surface were obtained, and shown by LEED. The atomically resolved STM images allowed to conclude on the high quality, and state of the art of our samples.

These samples were then used as substrate for the study of Rb adsorption and induced reconstructions on silicon. The adsorption of Rb atoms on the Si(111)-(7×7) will be outlined in two different chapters. In Chapter 5, the Rb deposition has been performed on the silicon substrate kept at room temperature, while in Chapter 6 the silicon substrate has been kept at higher temperatures (from 300 to 400°C) during deposition.

4.1 Sample preparation procedure

The silicon samples, used in this work were cut from a commercial Si(111) wafer 0.5 mm thick, with a diamond tip pencil, to a rectangular form 2 mm $\times$ 6 mm wide.

In general the production process of the Si(111) wafer relies on the intentional formation of an oxide layer which helps in protecting the wafer from contamination, both physical (scratches) and chemical (impurities like electrically active contaminants). The oxide acts as a passivating layer. Thus, once the sample was transferred in the preparation chamber (UHV environment), it was degassed at a temperature of ~ 600°C for several hours (typically overnight) by direct current heating through tantalum foils mounted at the bottom of the sample holder. The degas procedure have been used to get rid of the adsorbate on the surface.

Lastly, in order to obtain the (7×7) reconstruction and desorb the oxide layer, a flash of the sample was performed, i.e. a rapid annealing at high temperatures ~ 1000°C. During the degassing and flash procedure, the pressure in the preparation chamber never exceeded 10^{-9} mbar. The sample and the quality of the surface were readily first checked by LEED and then observed and characterized by STM.

4.2 LEED analysis

A typical LEED pattern of the Si(111) sample observed with a beam energy of 96.5 eV taken right after the flash procedure is shown in Fig. 4.1.

The well resolved (7×7) LEED pattern in Fig. 4.1 indicates a clean, flat, well-ordered and reconstructed surface. The yellow arrows labeled $\bar{b}_{1,2}$ in Fig. 4.1 indicate the Si(111)-

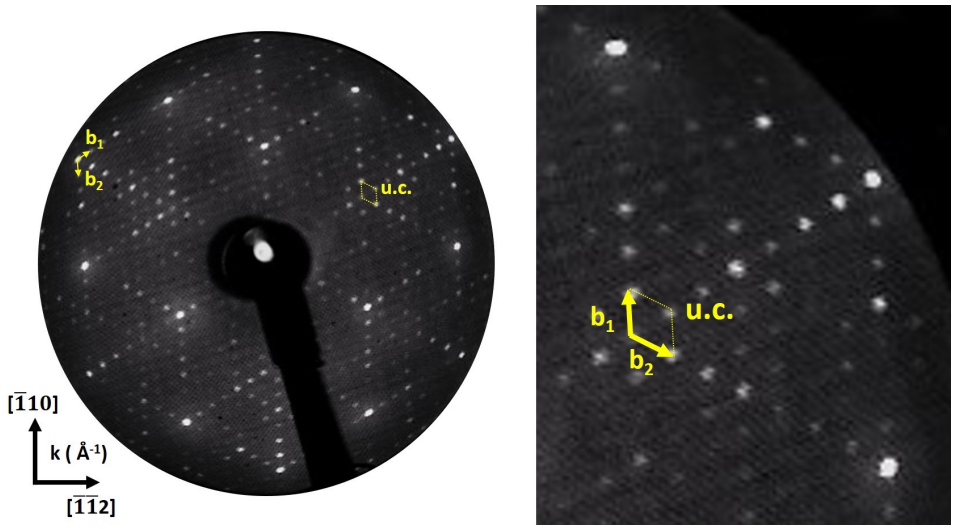

Figure 4.1: Si(111) 7×7 surface reconstruction. Left: LEED diffraction pattern with a beam energy of 96.5 eV. Right: zoom into the pattern to highlight the unit cell (u.c.) as well as the reciprocal lattice vectors.

(7×7) reciprocal lattice vectors. The unit cell is highlighted by a dashed line. The spots with the highest intensity correspond to the (1×1) structure of the underlying silicon crystal.

A striking feature of the DAS model of Si(111)-(7×7) is that the surface has a more complex symmetry than the bulk. There is an extra mirror line that runs along the short diagonal and separates the two halves of the unit cell into a faulted and unfaulted halves. This mirror raises the surface symmetry to 6-fold from 3-fold in the bulk [4]. Thus, one would expect to obtain a LEED pattern showing this 6-fold symmetry.

However, this is not what happens. The considerations on the diffraction from a 2D surface reported in Chapter 3.2, are valid only in the case of ideally true 2D network of atoms, and thus scattering only from one (i.e. the uppermost) layer. In real LEED experiments the primary electrons penetrate several atomic layers into the solid. The more they penetrate, the more scattering events in the direction perpendicular to the surface contribute to the LEED pattern. This leads to a modulation of the intensities of the Bragg reflections in comparison with the case of pure 2D scattering.

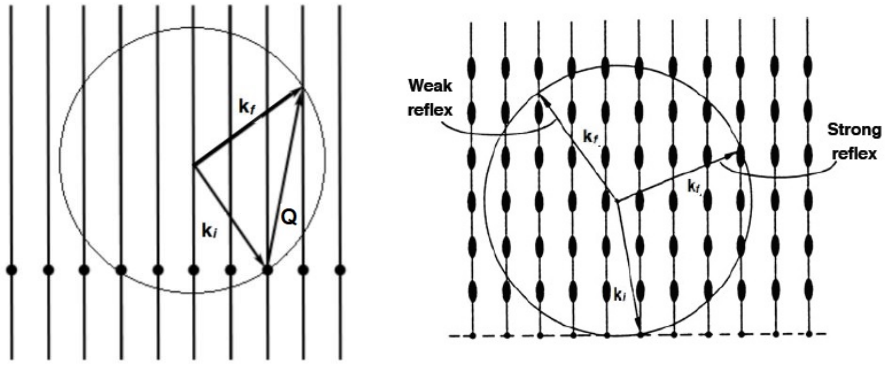

Figure 4.2: Construction of the Ewald sphere in the case (a) of scattering from the very first layer of the surface, and (b) of higher penetration depth, thus scattering from multiple layers (intermediate situation). From Ref. [59]

In the Ewald construction this translates in rods periodically less and more intense, as shown in Fig. 4.2 [59]. In the extreme case of 3D scattering, the thicker regions of the rods become points of the 3D reciprocal lattice. It is to be reminded that in the case of pure 2D scattering, the Laue condition for constructive interference in the direction perpendicular to the surface is always fulfilled. The deviation from the ideal case appears when this condition is not always fulfilled.

In the particular case of the (7×7) surface reconstruction the bulk 3-fold symmetric component will increasingly contribute to the resulting diffraction pattern as the energy is increased and destroy the ideally 6-fold symmetry of the (7×7) reconstruction alone. It is to be reminded that the (7×7) surface involves rearrangement and relaxation of atoms in four layers and each one of them has its own symmetry, e.g. the atoms of the topmost adatom layer form a local (2×2) structure, inside both the triangular subunits.

The mean free path of electrons, i.e. the sampling depth, in the (7×7) lattice is $\sim 0.7\sqrt{V}$Å (provided $V > 10$ V) [60]. As a consequence we expect that at energies around 50 eV or less the beam penetrates primarily only the adatom layer and the rest atom layer (see Fig. 2.4a). From this follows that for low primary beam energies the LEED pattern intensities should be nearly 6 fold symmetric and energy independent. This can be seen in the LEED patterns, and in the related cross sections, taken at 32 eV and 47 eV in Fig. 4.3

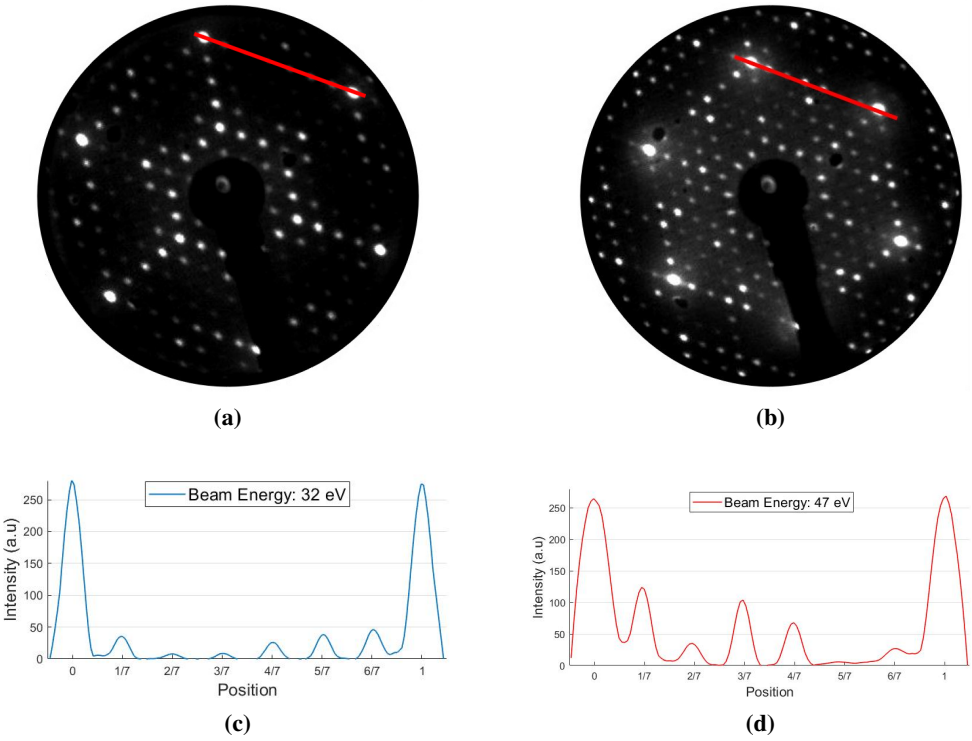

Figure 4.3: Typical low energy, (a) 32 eV and (b) 47 eV, LEED patterns showing nearly 6 fold symmetry. (c) and (d) show cross sections along the $(10) \rightarrow (01)$ direction indicated in the LEED patterns (a) and (b), respectively.

On the other hand, the LEED patterns that we measure for $E > 70$ eV usually have a pronounced 3-fold symmetry. At about 20 eV intervals, the fractional order LEED pattern rotational symmetry reverses from +3 fold to -3 fold. The symmetry change at higher voltages can be seen from Fig. 4.4 [1].

[1]The spots labeled as '0' and '1' in the cross section refer to the unfaulted and faulted half of the unit cell, respectively.

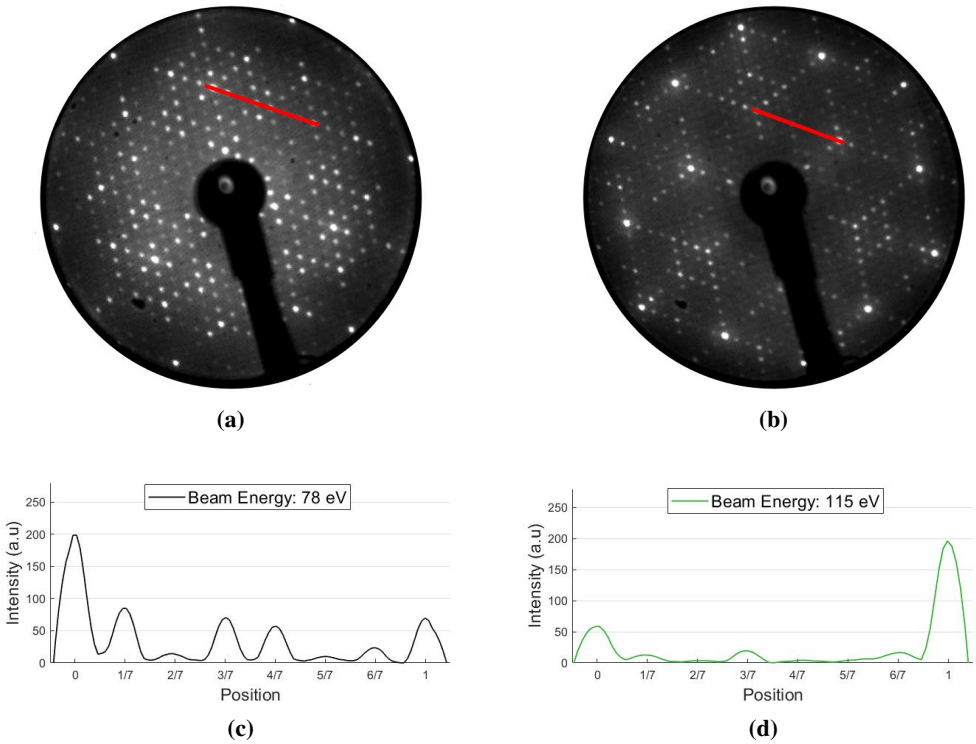

Figure 4.4: Typical (a) +3 fold and (b) -3 fold LEED patterns at beam energies 78 eV and 115 eV, respectively. (c) and (d) cross sections along the $(10) \rightarrow (01)$ direction in the cross sections indicated in the LEED patterns (a) and (b), respectively.

At higher beam energies, electrons penetrate deeper into the bulk and in the meantime will suffer from multiple scattering. The resulting diffraction pattern will be steeply 3-fold symmetric an with an increased background intensity (see Fig. 4.5). The most intense peaks are seen at low beam energy.

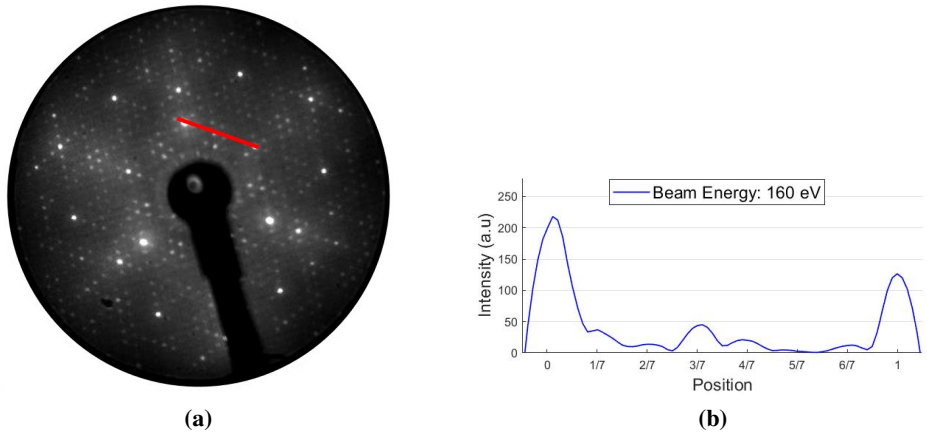

Figure 4.5: (a) High voltage LEED pattern, 160 eV. (b) cross sections along the $(10) \rightarrow (01)$ direction indicated in the LEED pattern (a).

As it could be now clearly understand, due to the symmetry change observed in the LEED pattern of the (7×7) surface as a function of the electron beam energy, it is mandatory to use compatible energy beams to compare different samples such as the pristine and the Rb exposed samples.

4.3 STM analysis

Fig. 4.6 shows three images from the reconstructed silicon surface, taken for different scan area dimensions.

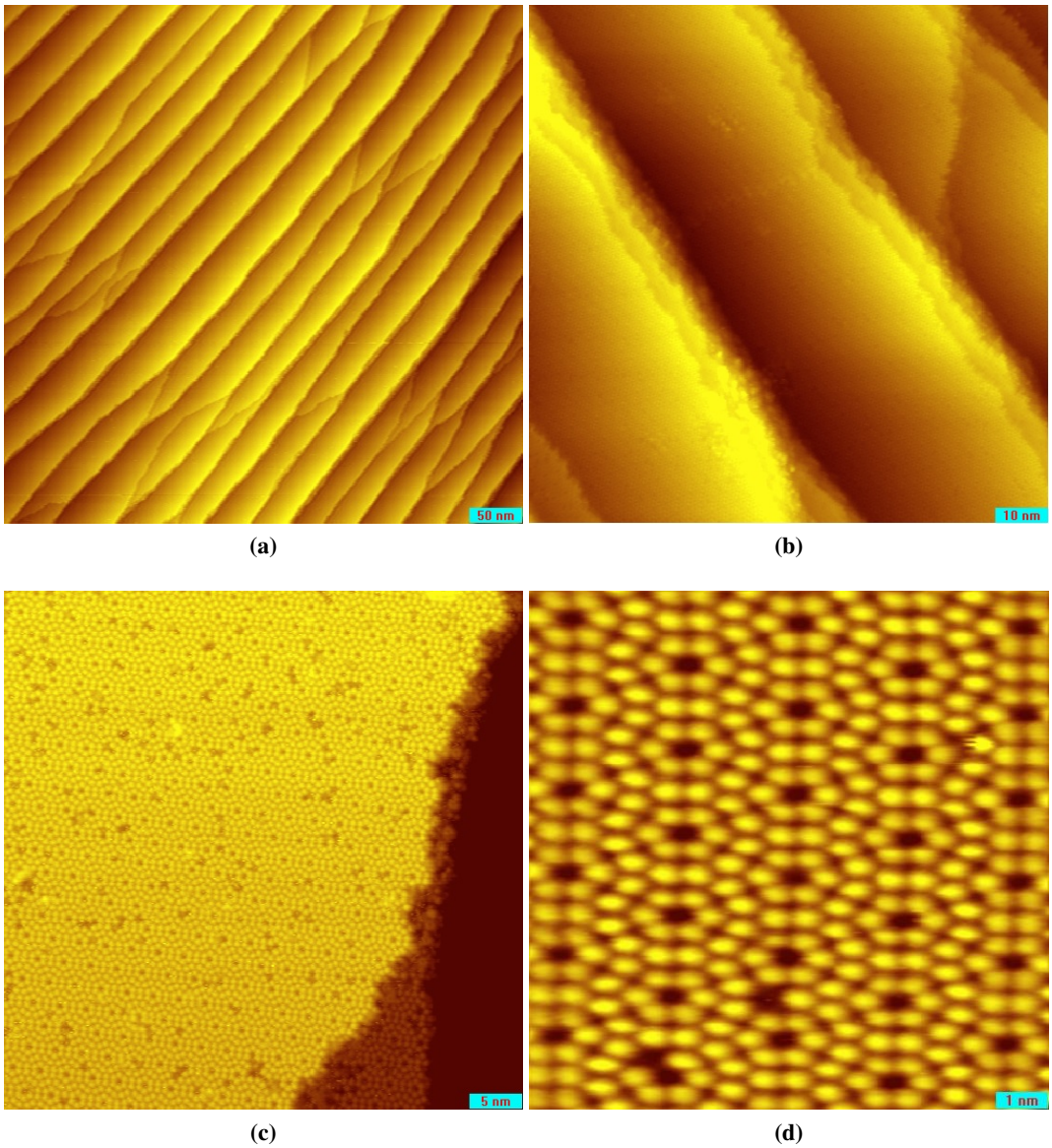

(a) **(b)**

(c) **(d)**

Figure 4.6: Si(111)-(7 × 7) surface reconstruction. STM topographic images of (a) 500 nm × 500 nm, (b) 100 nm × 100 nm, (c) 50 nm × 50 nm, and (d) 10 nm × 10 nm scan areas. Image parameters: (a) 1.3 V, 0.8 nA, (b) 1.3 V, 0.9 nA, (c) 1.3 V, 1.0 nA, and (d) 1.3 V, 0.80 nA.

Already from a 100 nm × 100 nm scan (see Fig. 4.6b), the presence of the (7 × 7= reconstructed surface is revealed. A zoom-in, in the same scanning area, better shows the uniform reconstruction of the surface (see Figs. 4.6c and 4.6d).

STM images show the presence of clean, parallel, and fairly regular ($\sim$ 50 nm large) flat terraces separated by single-high steps ($0.3 - 1.5$ nm), as shown in Fig. 4.7. The minimum step height corresponds to the interplanar distance of the $\{111\}$ faces which is 3.14 Å, or equivalently 314 pm. The number of steps formed depends on the misorientation of the wafer as well as the annealing process.

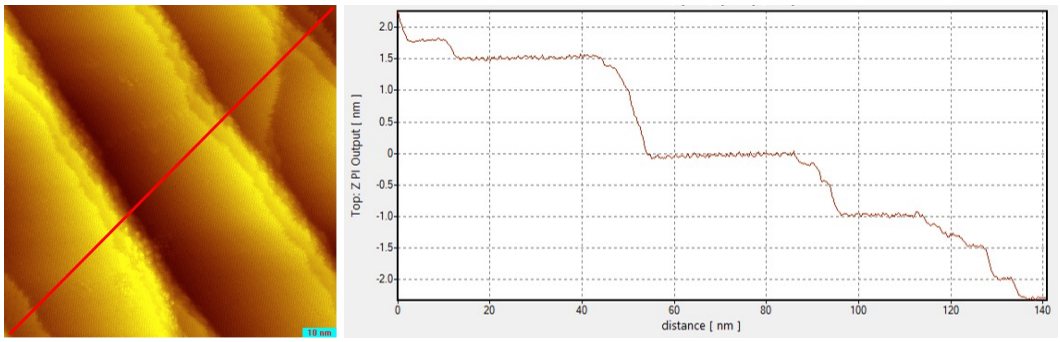

(a) (b)

Figure 4.7: (a) STM topographic image of the (7×7) surface from 100 nm $\times$ 100 nm scan area. Image parameters: 1.3 V, 0.9 nA. (b) Height profile along the red line in (a) of a typical STM scan 100 nm $\times$ 100 nm large.

Cross sections of the (7×7) surface, as shown in Fig. 4.8, allowed to measure the average length of the unit cell traslational vector which, from the experimental data, results 25.7 ± 1 Å. This value is in good agreement with the theoretical size of 26.88 Å of the (7×7) unit cell of the DAS model (see Section 2.2.2).

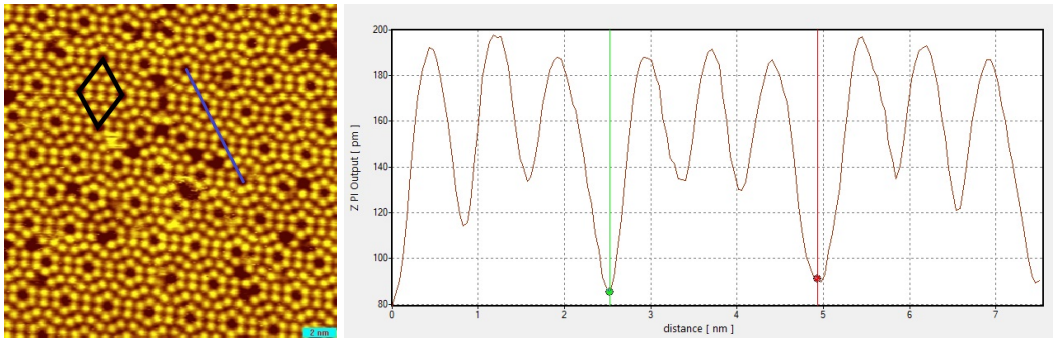

(a) (b)

Figure 4.8: (a): STM image of the (7×7) surface from a 20 nm $\times$ 20 nm scan area. The (7×7) unit cell has been highlighted in black. Image parameters: 1.3 V, 0.90 nA. (b): Cross section, along the blue line drawn in (a), reporting the surface periodicity.

In addition, stable, reproducible, and atomically resolved STM images were obtained at both tip bias polarities. Fig. 4.9 displays two STM topographical images, of a 5 nm $\times$ 5 nm area, where the 7×7 reconstruction is well visible both at positive (empty states) and negative (filled states) bias.

STM images of the Si(111)-(7×7) surface, taken at all bias values, reveal 12 topographic maxima per unit cell and a deep hole at the corners, as shown in Fig. 4.9. The positions of the observed maxima do not depend on the polarity of the applied bias voltage, i.e. the maxima of the empty and filled states are spatially coincident as shown in Fig. 4.9, thus the STM images provide geometric information about the positions of the surface atoms. These topographic maxima can be attributed to the 12 dangling bonds of the 12 adatoms in the DAS model (blue balls in Fig. 2.4b).

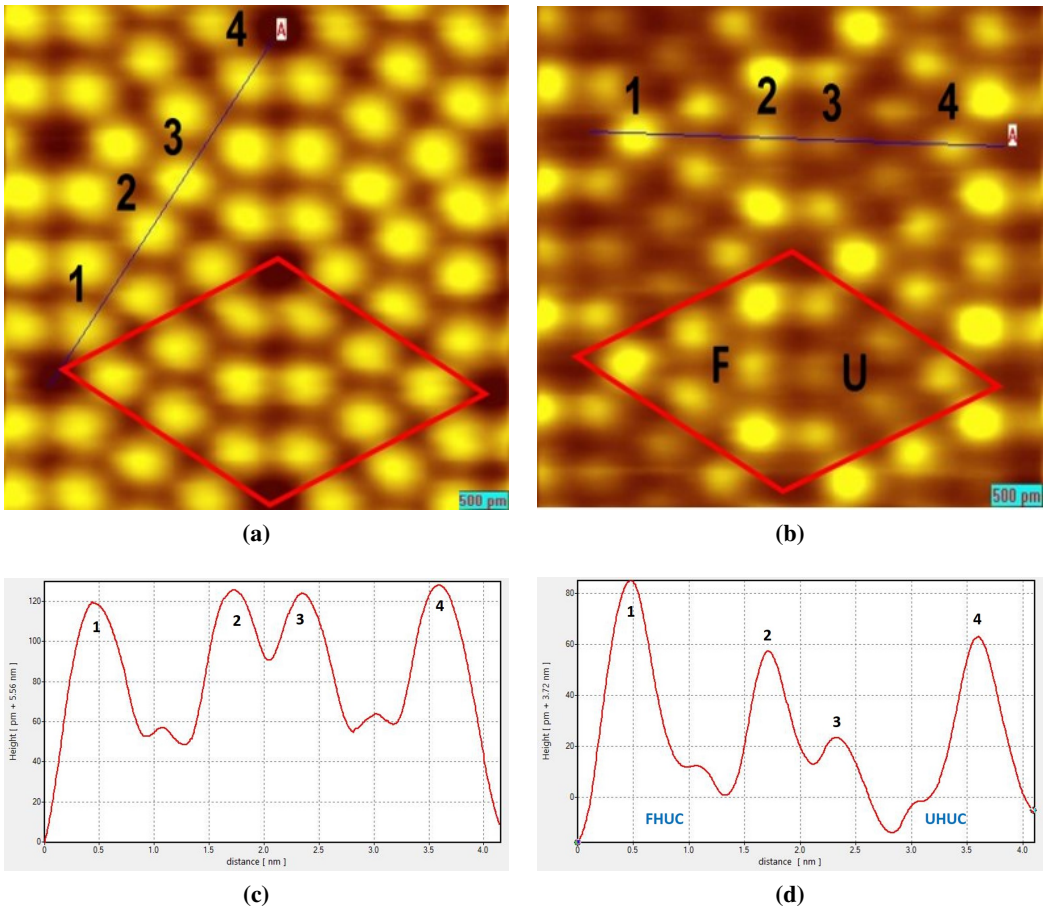

Figure 4.9: Si(111)-(7×7) surface reconstruction. Successive STM images of 5 nm $\times$ 5 nm scan area of (a) empy, and (b) dilled states. Image parameters: (a) 1.4 V, 0.8 nA, and (b) -1.4 V, 0.7 nA. The unit cell is highlighted in both images. The line profile shown in (c) and (d) are taken along the blue lines in Fig. (a) and (b). In (c) and (d), labels "1" and "3" denote corner adatoms and "2", "4" center adatoms

In the images obtained with a positive sample bias (Empty state, Fig. 4.9a), the 12 maxima are of even brightness (intensity), indicating an equal height of all adatoms (which sit in the top layer) in the unit cell, and the surface appears to be covered by flower like structure.

The images obtained with a negative sample bias (Filled state, Fig. 4.9b) clearly show an inequivalence between the adatoms in the two halves of a unit cell. The inequivalence between the adatoms in two different triangles can be explained by the slight electronic difference caused by the stacking fault (see 2.2.3). As a result, the filled state surface appears as a floor made up by two sets of triangular tiles. There is also an height difference among adatoms belonging to the same half on the unit cell. Adatoms can be further categorized into center adatoms, and corner adatoms (in Fig. 4.9b labeled as '1' ('3') and '2' ('4'), respectively). This brightness difference derives from the amount of charge transfer from the corner and center adatoms to rest atoms and corner holes [61]. Each adatom has a formal charge of +7/12, while rest atom and corner hole each has a formal charge of -1. Each corner adatom is surrounded by only one adjacent rest atom, while each center adatom has two neighboring rest atoms. This results in an amount of charge transferred from a corner adatoms to restatoms which is almost half that from center adatoms to restatoms. Therefore, the resulting electronic density of corner adatoms is higher than that of center adatoms. This is consistent with the brighter protrusion at corner adatoms than that at center adatoms in the filled states

STM image (as shown in Fig. 4.9b).

The dangling bonds on the adatoms are partially filled and therefore contribute to both empty and filled states. Center and corner adatoms possess two occupied surface states at different positions in the Fermi level. These states are probed in filled states images. The empty state image reveals instead the single adatom unoccupied state (U1). This feature is also revealed by STS.

STS spectra taken on a center adatom of the (7×7) surface allow to measure features of the local DOS function ($(dI/dV) \propto LDOS$). The occupied S1 and S2 states at negative bias voltages are clearly visible in Fig. 4.10. Also, the unoccupied state (U1) around +0.8 V is strongly pronounced.

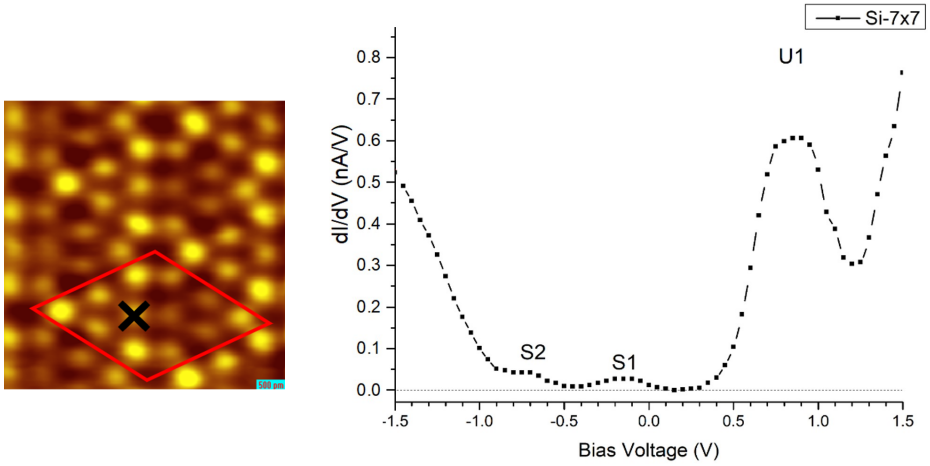

(a) **(b)**

Figure 4.10: (a) Filled states STM image of a 5 nm $\times$ 5 nm scan area of the pristine silicon surface. In red and black the unit cell and a center adatom are indicated. Image parameters: -1.4 V, 0.7 nA. (b) Average room temperature STS spectra measured on a center adatom, crossed in (a). Surface states (S1, S2) as well as the unoccupied state (U1) are indicated. Data points taken at intervals of 50 mV. Sample bias: -2 V, 500pA.

In agreement with the literature [2], the energy gap disappears and the Fermi level (pinned at 0.65 eV) sits inside the surface band, providing thereby the metallic conduction of the surface, at room temperature.

4.4 Summary

In this chapter, we demonstrated that the procedure we use to obtain the (7×7) substrate is highly reproducible. Moreover, the produced samples are high quality and state of the art. All the features of this surface that we measured resulted in agreement with the existing literature, i.e. the symmetry of the surface seen in the diffraction pattern, as well as the electronical and geometrical features revealed by the STM and STS.

This enabled us to use the so produced (7×7) as a template for the study of Rb adsorption on the Si(111). The results of the study are outlined in the next few chapters.

Chapter 5

Rb on Si(111): Room Temperature deposition

For several alkali metals it has been reported that an AM/Si(111)-(3×1) reconstruction could be obtained by room temperature deposition of the AM on the silicon substrate followed by an annealing.

In this chapter we therefore start by studying the surface modifications induced by Rb deposition at room temperature on the Si(111)-(7×7). After this characterization, successive annealing cycles have been performed. After each deposition and the annealing step, LEED and STM analysis have been carried out. A summary of the main findings will follow.

5.1 RT deposition

Figures 5.1 and 5.2 show the LEED patterns of the samples prepared by evaporating Rb at room temperature for 5, 10, and 15 minutes on the (7×7) surface, at a Rb rate of $2.2 \cdot 10^{-11}$ Torr.

(a) Dep. time: 5 min. **(b)** Dep. time: 10 min. **(c)** Dep. time: 15 min.

Figure 5.1: LEED patterns of (a) 5 min, (b) 10 min, and (c) 15 min room temperature Rb deposition at a rate of $2.2 \cdot 10^{-11}$ Torr on the pristine Si(111)-(7×7) sample. Contrast has been improved to highlight the presence of the (7×7) spots. Beam Energy: 76.5 eV.

The LEED patterns, shown in Fig. 5.1 and in Fig. 5.2, obtained upon room temperature Rb deposition clearly show a (7×7) pattern. However, the brightness of the (7×7) spots decreases, compared to the pristine silicon sample. The intensity of the (1×1) spots, relative to the silicon bulk, decrease as well at all the dosing time studied (see the patterns in Fig. 5.2e). In particular, Fig. 5.2e shows an increased asymmetry in the (1×1) spots after the

depositions. The spot labeled as '1' (faulted half) is decreased almost of the same amount for all the three dosing time studied, while the spot labeled as '0' (unfaulted half) is increasingly decreased with the deposition time. This might indicate that there is a preferential adsorption on the faulted half of the unit cell, up to saturation which is already achieved after 5 minutes deposition. Subsequently Rb atoms start adsorbing on the unfaulted half (to saturate all the adsorption sites on this half, takes more than 15 minutes deposition). These observations suggest the presence a disordered alkali overlayer, preferentially adsorbed on the faulted half of the unit cell. With increasing Rb coverage, Rb atoms starts to adsorb also on the unfaulted half. Moreover, this alkali overlayer does not destroy the periodicity of the underlying reconstructed Si surface. This interpretation is also consistent with the background increase, seen at increasing Rb coverage (as seen in Fig. 5.2).

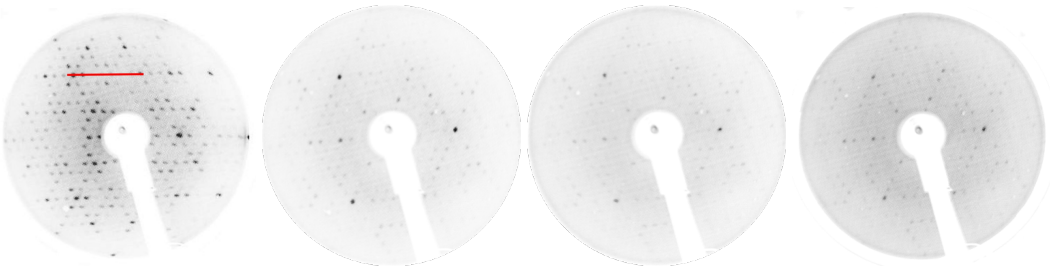

(a) Pristine. **(b)** Dep. time: 5 min. **(c)** Dep. time: 10 min. **(d)** Dep. time: 15 min.

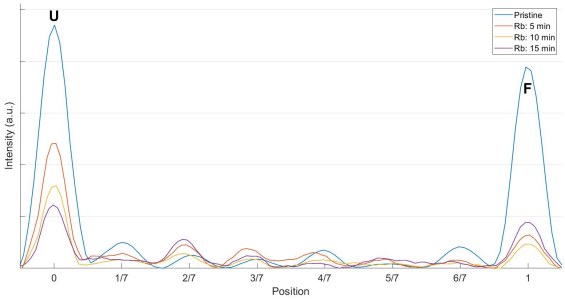

(e) LEED cross section

	Spot position	
Dep. Time	**0**	**1**
5 min	49%	84%
10 min	66%	88%
15 min	74%	77%

(f) Table intensity ratio.

Figure 5.2: LEED patterns of (a) the pristine Si(111)-(7 × 7) sample, (b) 5 min, (c) 10 min, and (d) 15 min room temperature Rb deposition at a rate of $2.2 \cdot 10^{-11}$ Torr on the pristine Si(111)-(7×) sample. Images are shown in B/W in order to highlight the increase in background intensities. Figure (e) shows a cross section of raw LEED patterns along the $(10) \rightarrow (01)$ direction, indicated in the pattern in (a). Beam Energy: 76.5 eV. (f) Table reporting intensity decrease of the (1×1) spots of the pristine silicon sample and upon Rb deposition (computed as $[\%] = \frac{I_{pristine} - I_{Rb/Si}}{I_{pristine}}$).

Figure 5.3 shows two STM images of 50 nm × 50 nm scan areas of the Rb/Si surface obtained upon RT Rb deposition on the (7 × 7) silicon surface. The typical triangular pattern observed in the filled states images of the Si(111)-(7 × 7) surface is still clearly visible and well resolved, upon Rb deposition.

A more detailed inspection of the samples surface shows that rubidium atoms preferentially adsorb on the faulted half unit cell, see Fig. 5.4a and 5.4b. This is consistent with the observed LEED spots intensities (in Fig. 5.2e). Triangular and lobe-like Rb clusters can be observed on the surface, in Fig. 5.4c the two features are highlighted by a red arrow and encircled. The clustering behavior of the Rb atoms increases with deposition time. Topographic STM scans of the sample surfaces upon Rb deposition at room temperature became more difficult as the dosing time was increased due to the high interaction between the weakly bound

Rb atoms and the STM tip.

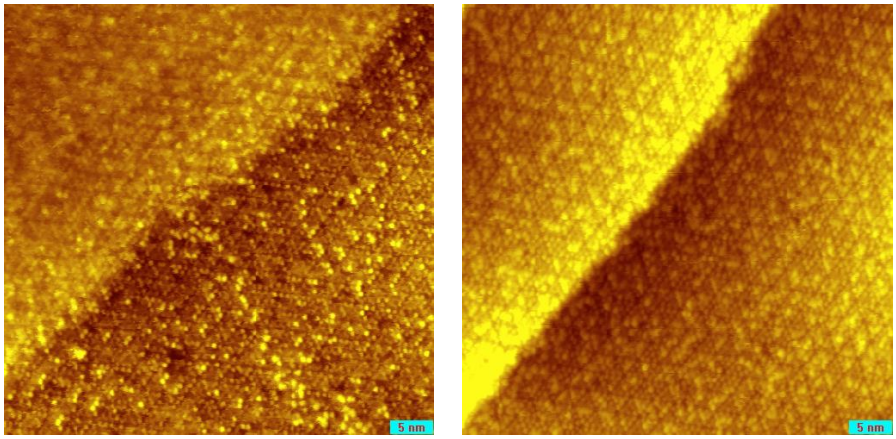

(a) (b)

Figure 5.3: STM topographic images of two different 50 nm × 50 nm scan areas after 2 min room temperature Rb deposition at 5.1 A on the pristine Si(111)-(7 × 7) sample. Image parameters: (a) -1.3 V, 0.8 nA, (b) and (c) -1.5 V, 0.8 nA.

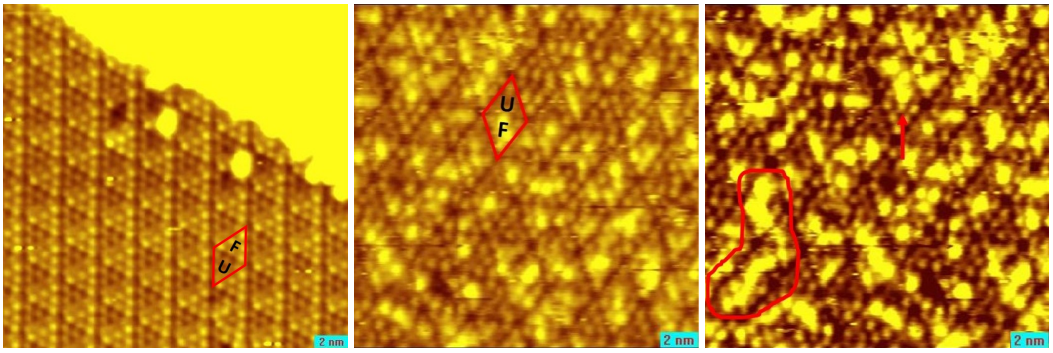

(a) (b) (c)

Figure 5.4: STM topographic images of 20 nm × 20 nm scan areas (a) pristine Si(111)-(7 × 7) surface, (b) and (c) upon 2 min room temperature Rb deposition at 5.1 A on the pristine Si(111)-(7 × 7) sample. In (a) and (b) the unit cell as well as the faulted and unfaulted subunits are highligted in red. In (c) in red, the arrows indicate triangular Rb clusters while a lobe-like pattern is encircled. (b) and (c) are two different scan areas of the same sample shown with different height contrast which is used to highlight different features of the sample. Image parameters: (a) -1.3 V, 0.8 nA, (b) and (c) -1.5 V, 0.8 nA.

Consistent with the LEED patterns, STM showed that room temperature deposition of Rb did not induce any new surface reconstruction nor modification of the surface periodicity. Rb atoms rather adsorbed on the (7 × 7) surface in a disordered fashion, but preferentially in the faulted half of the unit cell.

5.2 Annealing

In this section I discuss the results obtained upon annealing the samples obtained by Rb deposition at at room temperature. It can be expected that the annealing cycles, providing thermal energy to the system, will either increase the ordering of the Rb atoms on the surface

and/or provide enough energy for the Rb atoms to desorb from the surface, or it will provide energy for the Rb to react with the silicon atoms and form silicides.

A first annealing at 300°C has been performed on the samples prepared by dosing Rb for 5,10 and 15 minutes at room temperature with a rate of $2.2 \cdot 10^{-11}$ Torr (sample analyzed in the previous section).

The 15 minutes Rb-dosed silicon sample has been further annealed at 350°C and 400°C for 10 minutes/cycle. Afterwords a fast annealing up to 700°C has been also performed on this sample.

5.2.1 Annealing at 300°C

Fig. 5.5 shows cropped LEED patterns of the samples prepared by evaporating Rb at room temperature for 5, 10 and 15 minutes on the pristine (7×7) surface, at a Rb rate of $2.2 \cdot 10^{-11}$ Torr, before and after the annealing at 300°C.

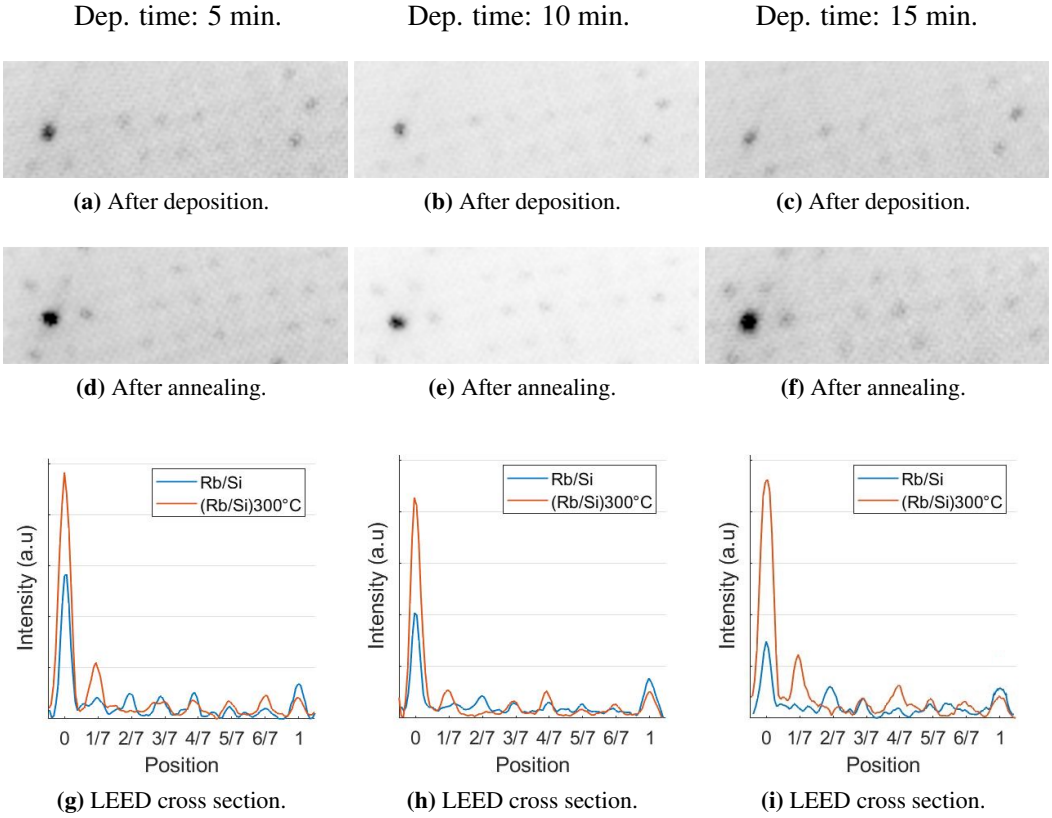

(a) After deposition. **(b)** After deposition. **(c)** After deposition.

(d) After annealing. **(e)** After annealing. **(f)** After annealing.

(g) LEED cross section. **(h)** LEED cross section. **(i)** LEED cross section.

Figure 5.5: Cropped LEED patterns along the $(10) \rightarrow (01)$ direction. LEED patterns of (a) and (d) of 5 min, (b) and (e) 10 min, and (c) and (f) 15 min room temperature Rb deposition at a rate of $2.2 \cdot 10^{-11}$ Torr on the pristine Si(111)-(7×7) sample. The patterns on the first row have been taken right after deposition at RT, while the second row reports the patterns of the same samples after 10 minutes annealing at 300°C. Beam Energy: 76.5 eV.

The LEED patterns revealed an increase in the intensity of the (7×7) spots. Moreover, the LEED patterns showed an increased asymmetry in the (1×1) spots. There was an high increase in the intensity of the spot relative to the unfaulted half of the unit cell (labeled as '0' in the cross sections in Fig. 5.5), while the intensity of the spot relative to the faulted half changed only very little. A gradual decrease in the background intensity is seen as well. (as seen from the cropped LEED patterns in Fig. 5.5). These evidences suggest Rb desorption from the unfaulted half of the unit cell and a partial rearrangement of the surface atoms.

STM provided further information both on the surface and about the Rb desorption process. Surprisingly, the presence of a new ordered phase on the surface was readily revealed after 10 minutes annealing at 300°C.

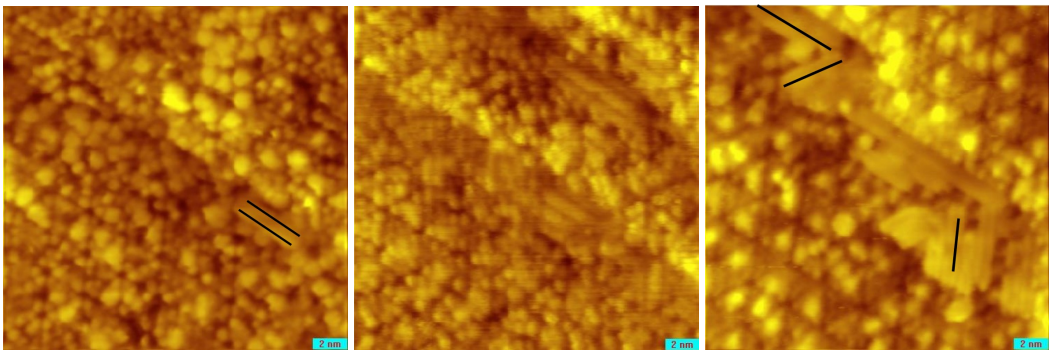

(a) **(b)** **(c)**

Figure 5.6: STM topographic images of 50 nm × 50 nm scan areas taken after an annealing at 300°C of room temperature Rb deposition on the pristine Si(111)-(7 × 7) for (a) 5 min, (b) 10 min and (c) 15 min. Image parameters: -2.5 V, 40 pA.

The (3 × 1) domains have been identified according to what reported in literature, refer to the STM scans shown in Fig. 2.6. At low amount of Rb, the surface presented just few isolated double bounded chains, i.e. (3 × 1) domains large one unit cell (see Fig. 5.6a). By increasing the amount of evaporated Rb, the (3 × 1) domains increased in size and the number of domains increased as well (see Fig. 5.6b). High dosing time allowed to form larger domains. The domains could be found in all the three possible orientations, as highlighted in Fig. 5.6c.

Even though the presence of a (3 × 1) phase became clear at high dosing time, the amount of converted surface areas did not exceed few percent of the total surface area (as seen in Fig. 5.7a). This explains why the LEED pattern only showed (7 × 7) spots.

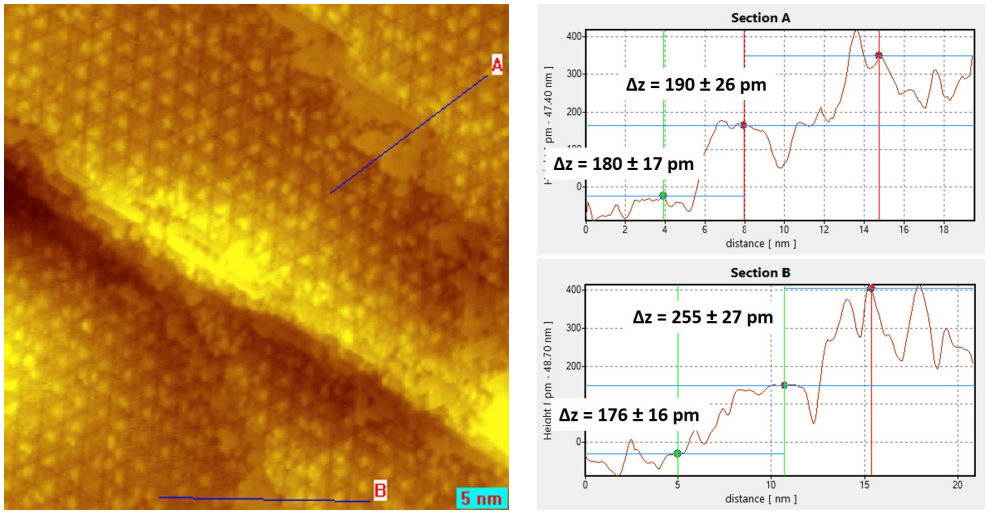

(a) **(b)**

Figure 5.7: (a) STM image from a 50 nm × 50 nm scan area of the (3 × 1) surface taken after an annealing at 300°C of room temperature Rb deposition on the pristine Si(111)-(7 × 7) sample for 15 min at a rate of $2.2 \cdot 10^{-11}$ Torr. Image parameters: -2.5 V, 40 pA. (b): Cross sections along the lines drawn in (a).

STM scans revealed that the (3×1) phase nucleates mainly near the step edge or on defects of the underlying silicon surface but never isolated in the center of the terraces. Fig. 5.7 shows a 50 nm $\times$ 50 nm large STM image and two cross sections taken across terraces. These cross sections have been taken in order to understand whether the (3×1) phase grows on the upper or lower edge of the terrace. The analysis of the height difference between the (3×1) areas and the unconverted (7×7) terraces, measured in multiple scans, revealed that this value is 180 ± 17 pm going from (3×1) to (7×7) areas, while going from (7×7) to (3×1) areas it spanned a wider range of values $(150 - 500$ pm). This suggests that the transformation takes place near the step edge on the lower terrace and that there is an height difference between the (7×7) and the (3×1) reconstruction on the same terrace.

Near the lower step edge of the terraces the density of Rb atoms is highly increased, as can be seen in Fig. 5.8a. Since this was not observed before the annealing, this is a clear indication of the an increase in the mobility of the Rb atoms due to the thermal energy provided by the annealing and proves that the bonding created between the Rb and Si atoms is weak, upon RT deposition of Rb. Rb atoms move isotropically, however when they get close to the step edge, they bind to silicon atoms. At the step edge the periodicity of the surface is broken thus the silicon atoms have an additional dangling bond which implies higher free energy.

A closer inspection of the unconverted areas revealed the presence of Rb single atoms or small clusters adsorbed preferentially in the faulted half of the (7×7) reconstruction, which still results clearly visible (see Fig. 5.8b). Upon annealing, the character of the Rb adsorption on the unconverted areas thus did not change. We observed reduced interaction between the Rb atoms and STM tip. These observations are consistent with the LEED evidences. Moreover they suggest that Rb atoms that were adsorbed on unfaulted half of the unit cell either moved and to form the (3×1) or just desorbed from the surface. Moreover, the presented evidences suggest an increased interaction between Rb and Si atoms.

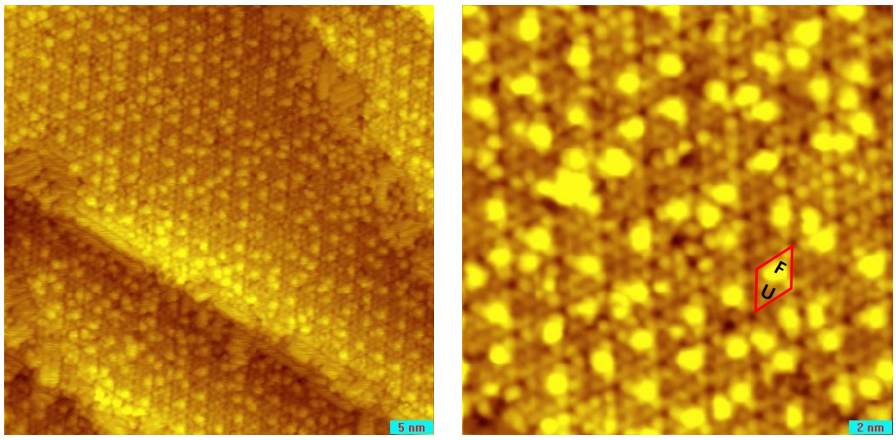

(a) **(b)**

Figure 5.8: STM topographic images of (a) 50 nm $\times$ 50 nm and (b) 20 nm $\times$ 20 nm scan areas taken after an annealing at 300°C of room temperature Rb deposition on the 7×7 silicon substrate for 15 minutes at a rate of $2.2 \cdot 10^{-11}$ Torr. Image parameters: -2.5 V, 40 pA.

5.2.2 Annealing cycles above 300°C

Rb desorption from the surface became evident after a second annealing at 350°C. The (3×1) phase completely disappeared, and the Rb atoms that did not leave the surface mainly

aggregated near the terrace edges, see Fig. 5.9 (Rb clusters in STM scans are imaged as protrusions on the surface).

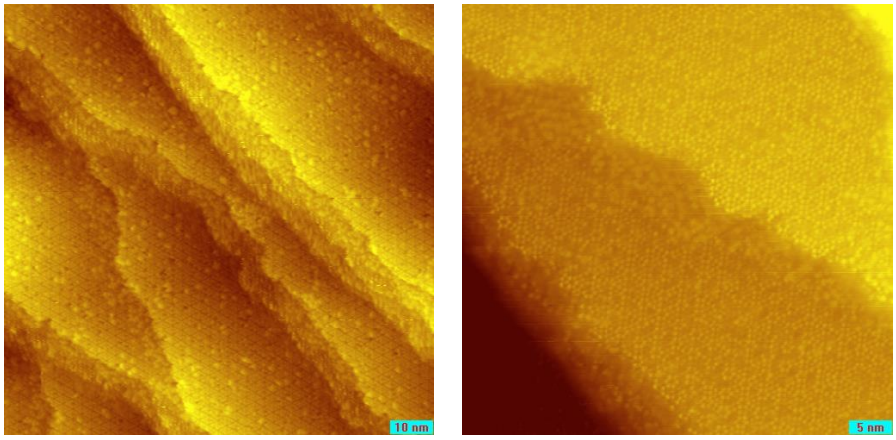

(a) **(b)**

Figure 5.9: STM topographic images of (a) 100 nm $\times$ 100 nm, and (b) 50 nm $\times$ 50 nm scan areas taken after an annealing at 350°C of room temperature Rb deposition on the (7×7) silicon substrate for 15 minutes at a rate of $2.2 \cdot 10^{-11}$ Torr. Image parameters: (a) -1.5 V 300 pA, and (b) -2.5 V 40 pA.

Moreover, as clearly seen from a direct comparison with the pristine silicon surface (shown in Fig.5.10a), after the annealing (shown in Fig.5.10b) the number of defects in the surface increased (holes and vacancies in STM scans are imaged as dark spots).

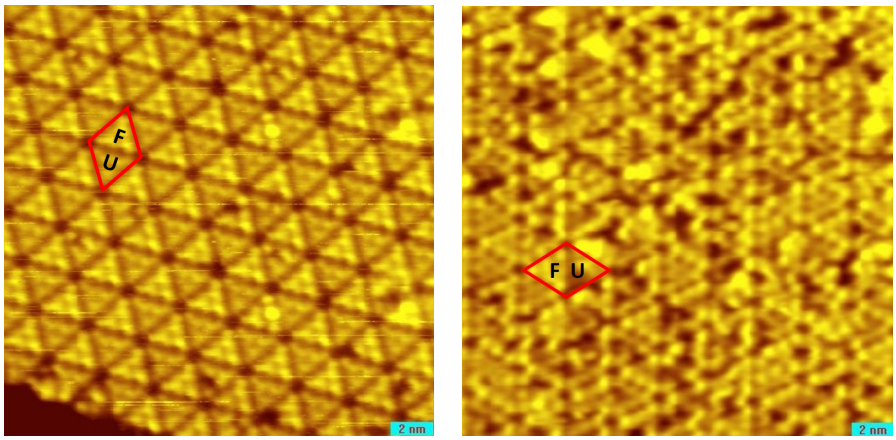

(a) Pristine. **(b)** Ann. 350°C of Rb/Si.

Figure 5.10: STM topographic images of 20 nm $\times$ 20 nm scan areas of (a) pristine silicon, and (b) after an annealing at 350°C of room temperature Rb deposition on the (7×7) silicon substrate for 15 minutes at a rate of $2.2 \cdot 10^{-11}$ Torr. Image parameters: (a) -1.3 V, 0.8 nA, and (b) -2.5 V, 40 pA. The (7×7) unit cell is highlighted in red.

After a further annealing at 400°C, the number of clusters adsorbed on the (7×7) reconstruction vastly decreased. However the number of holes and defects on the surface did not increase. Fig. 5.11 shows, via 100 nm $\times$ 100 nm large STM images, the evolution of the surface upon successive annealing at 300, 350 and 400°C, respectively.

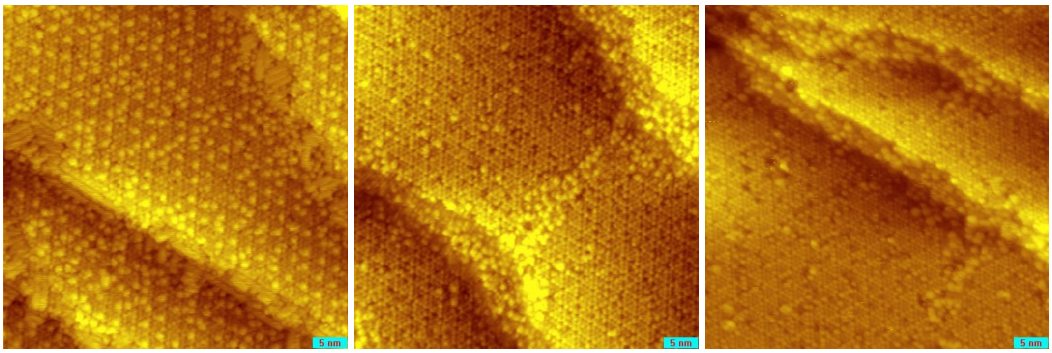

(a) Annealing 300°C. **(b)** Annealing 350°C. **(c)** Annealing 400°C.

Figure 5.11: Annealing at (a) 300, (b) 350 and (c) 400°C STM topographic images of 100 nm × 100 nm scan areas taken aof room temperature Rb deposition on the (7×7) silicon substrate for 15 minutes at a rate of $2.2 \cdot 10^{-11}$ Torr. Image parameters: -2.5 V, 40 pA.

Lastly, we performed a fast annealing of the sample up to 700°C. The ramp we used has

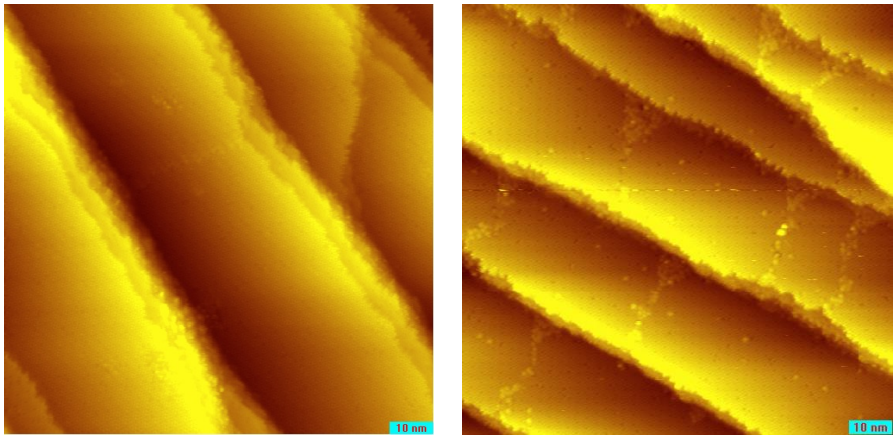

(a) Pristine. **(b)** Ann. 700°C of Rb/Si.

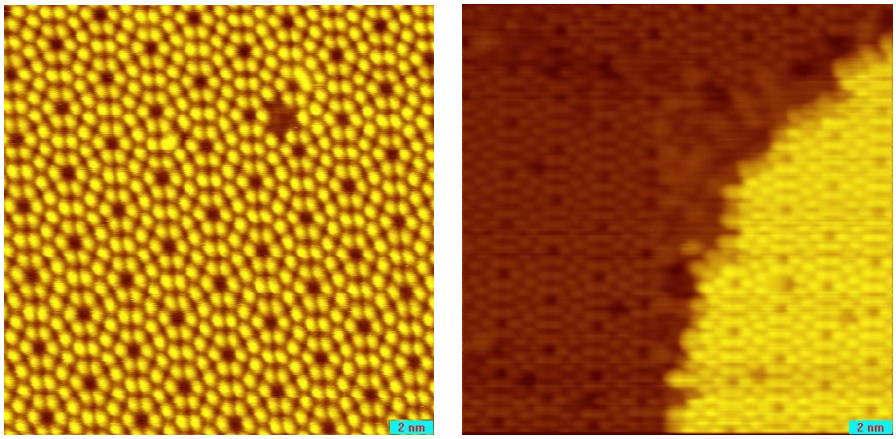

(c) Pristine. **(d)** Ann. 700°C of Rb/Si.

Figure 5.12: STM topographic images of (a), (c) pristine, and (b), (d) after an annealing at 700°C of room temperature Rb deposition on the (7×7) silicon substrate for 15 minutes at a rate of $2.2 \cdot 10^{-11}$ Torr. Image size: (a) and (b) 100 nm × 100 nm, (c) and (d) 20 nm × 20 nm Image parameters: (a) and (c) 1.3 V, 0.8 nA, (b) and (d) 1.5 V, 40 pA.

a slope of 1°C/s, the sample was then left at the temperature of 700°C for 10 s, after that the heating was immediately switched off. The resulting surface, apart from few defects, transitioned back to the original clean surface structure (see Fig. 5.12).

5.3 Results summary

We followed the evolution of the (7×7) silicon surface structure upon room temperature Rb deposition and after annealing steps.

We found that room temperature deposition of Rb did not induce any new surface reconstruction nor modification of the (7×7) periodicity of the underlying silicon substrate. Rb atoms rather adsorbed on the (7×7) surface in a disordered fashion, but preferentially in the faulted half of the unit cell.

Upon a 300°C annealing step, small (3×1) regions appeared on the surface, as imaged by STM. In particular, the number of converted areas increased with the amount of deposited Rb. However, the area of (3×1) patches did not exceed a few percent (even after 15 minutes deposition), explaining why we did not see (3×1) spots in LEED patterns. Despite this, we obtained the first direct evidence of the formation of the (3×1) phase with this approach using Rb as adsorbate, thus this analysis represents a novelty and an addition to the accumulated literature.

Further annealing provided evidence for the gradual Rb desorption from the silicon surface. At 350°C holes and vacancies appeared in the (7×7) periodicity. Annealing at even higher temperatures the Rb clusters adsorbed on the surface vastly decreased. After a fast annealing to 700°C the surface transitioned back to its original state. This revealed the reversibility of the adsorption and desorption process of Rb from the Si(111)-(7×7),

Chapter 6

Rubidium on Si(111): Deposition at High Temperatures

In this chapter we study the surface modifications induced by the Rb deposition on the Si(111)-(7 × 7) held at elevated temperature (300-400°C). The dependence on deposition conditions such as substrate temperature or deposition time and rate is investigated. These parameters critically influence the adsorption kinetics, thus the final sample morphology. We show the first real space image of a well resolved Rb induced Si(111)-(3 × 1) reconstruction. Additionally, such a sample has been subjected to an annealing step. After each deposition and annealing, LEED and STM analysis have been performed. The results are discussed and analyzed. Afterwards, a summary on the main findings follows.

6.1 Parameter tuning

The LEED and STM analysis presented in this section is organized as follows:

- Substrate temperature: during Rb deposition, the silicon substrate was held at temperatures between 300 and 400°C. We performed the same analysis for different sets of fixed parameters (i.e. deposition time and deposition rate).
- Rubidium amount: Rb was deposited for different amounts of time on the silicon surface held at elevated temperature. We report the analysis of a sample prepared with a particular set of fixed (i.e. substrate temperature and deposition rate) and optimized parameters.
- Deposition rate: three different deposition rates and their influence on the reconstruction are reported.

6.1.1 Substrate temperature

Various Rb depositions were performed on the Si(111)-(7 × 7) while the silicon substrate was held at temperatures between 300 and 400°C. LEED was readily used to check and study the just obtained samples. Hereafter I will present the results obtained for two different sets of samples. For one set of samples, STM analysis was performed as well. Conclusions from both analysis will be reported.

When Rb was deposited on the silicon substrate kept at a temperature of 300°C, the LEED pattern showed a very weak (3 × 1) pattern superimposed on a (7 × 7) pattern (see Fig. 6.1 (a)(e)(i)). As the substrate temperature was increased, the (3 × 1) pattern became

more clear. At 345°C we found a bright (3×1) pattern superimposed on a weak (7×7) (see Fig. 6.1(b)(f)(j)). With substrate temperatures higher than 345°C, the (7×7) spots gained brightness while (3×1) pattern started to weaken, up to a point where the reconstruction did not form. Upon deposition on the silicon substrate held at temperature of 400°C or higher, the 3×1 spots did not appear up in the LEED pattern (see Fig. 6.1 (d)(h)(l)), and only the (7×7) pattern was observed.

It is to note that with increasing amount of (3×1) conversion, the LEED pattern symmetry changes gradually from 3-fold to 6-fold. This is actually to be expected since the (3×1) does not have any fault.

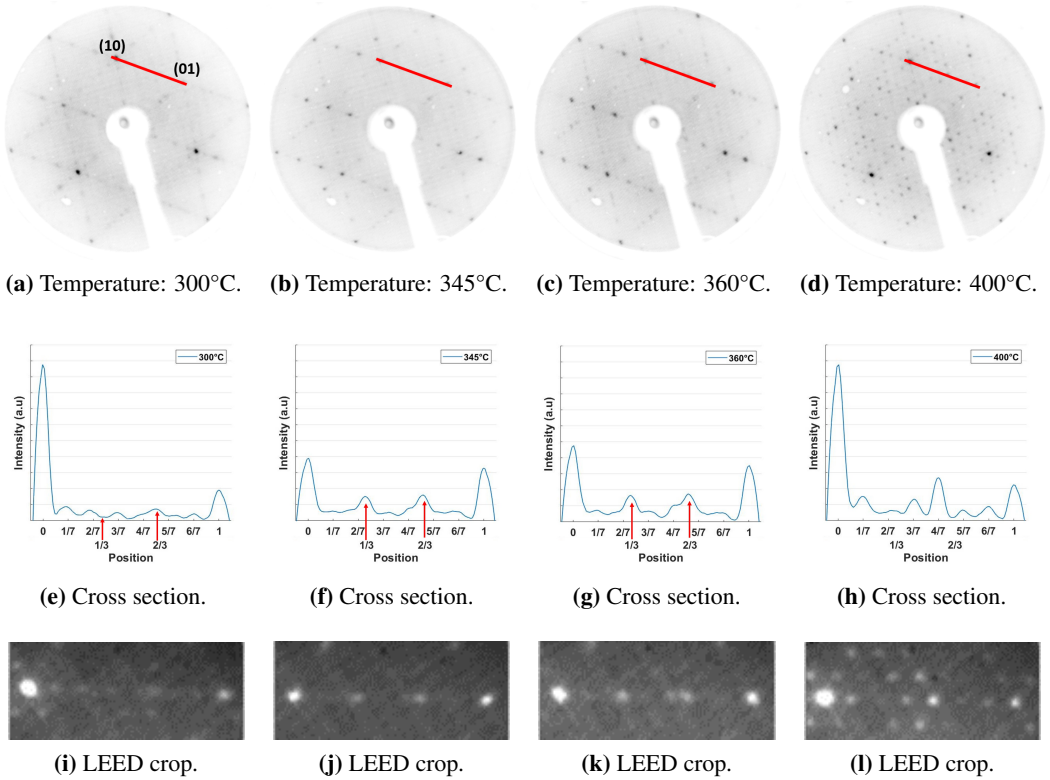

(a) Temperature: 300°C. **(b)** Temperature: 345°C. **(c)** Temperature: 360°C. **(d)** Temperature: 400°C.

(e) Cross section. **(f)** Cross section. **(g)** Cross section. **(h)** Cross section.

(i) LEED crop. **(j)** LEED crop. **(k)** LEED crop. **(l)** LEED crop.

Figure 6.1: LEED patterns of Rb deposited for 5 minutes at a rate of $5.6 \cdot 10^{-11}$ Torr on the Si(111)-(7×7) surface kept at different temperatures during deposition ((a) 300°C, (b) 345°C, (c) 360°C, and (d) 400°C. Beam Energy: 76.5 eV. In the second row we report the cross sections of raw LEED patterns taken along the $(10) \rightarrow (01)$ direction drawn with a red line in (a). In the third row we report the LEED patters cropped in the region of the cross section cut.

We studied the (3×1) LEED spots and plotted the average intensities of those in the first (1×1) unit cells for chosen beam energies (i.e. 76.5 and 95.5 eV) and two different set of samples (as reported in Fig. 6.2). What we found is that the temperature at which we have the maximum conversion of the surface into a (3×1) phase, is approximately 345°C.

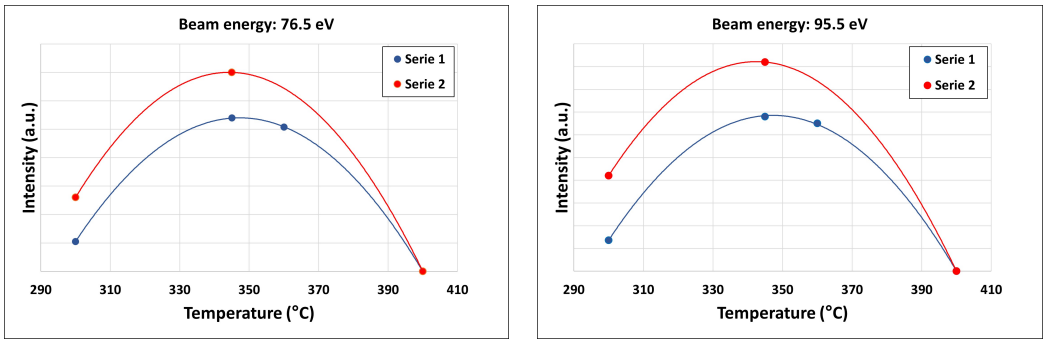

(a) **(b)**

Figure 6.2: Average intensity analysis of the 3×1 LEED spots in the first 1×1 unit cells. Serie 1 and Serie 2 refer to the samples prepared with 5 minutes deposition with a rate of 5.6 Torr and 9 minutes deposition with a rate of $2.2 \cdot 10^{-11}$ Torr on the Si(111)-(7×7) surface kept at 345°C during deposition. Beam Energy: (a) 76.5 eV and (b) 95.5 eV. The spline connecting the data points is drawn as a guide to the eye.

A peculiarity of the just obtained (3×1) Rb induced reconstruction is the presence, clearly revealed in the LEED patterns, of a directionality in the growth of this phase at all temperatures in the range of study. Thus the three possible orientations for the (3×1) phase are observed but with different intensities, as seen from Fig. 6.3. The direction of the line cut in red is the direction with the highest intensity of the (3×1) spots (further details on this, will be given in section 6.1.4).

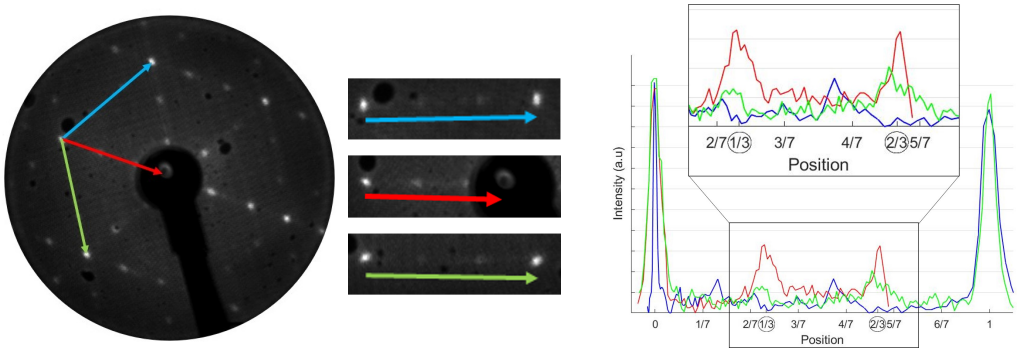

(a) **(b)** **(c)**

Figure 6.3: (a) LEED pattern of 5 minutes deposition at a rate of $5.6 \cdot 10^{-11}$ Torr on the Si(111)-(7×7) surface kept at 345°C during deposition. (b) Cross section of thee LEED pattern in (a) along the three equivalent growth direction of the (3×1) phase. The cuts and their direction are shown in (a) with the same color code used in the cross section plot. Beam Energy: 47.5 eV. The spot in the positions labeled $1/3$ and $2/3$ correspond to the (3×1) spots.

STM on these samples allowed to obtain the first real-space images of the Rb-induced (3×1) on Si(111). Well resolved images of large (3×1) domains, e.g. Fig. 6.4b, were obtained (further details will be given in section 6.1.4). The STM analysis, of samples dosed with Rb for 9 minutes at a rate of $2.2 \cdot 10^{-11}$ Torr, allowed to calculate the percentage of regions converted in (3×1) for different substrate temperatures used during the deposition and to corroborate the diffraction results.

In Fig. 6.4 are shown STM scans of a Rb/Si sample with Rb deposited for 9 minutes at a rate of $2.2 \cdot 10^{-11}$ Torr on the Si(111)-(7×7) surface kept at 345°C during deposition. When Rb (low to medium amount, corresponding to $0 - 9$ min deposition at a rate of

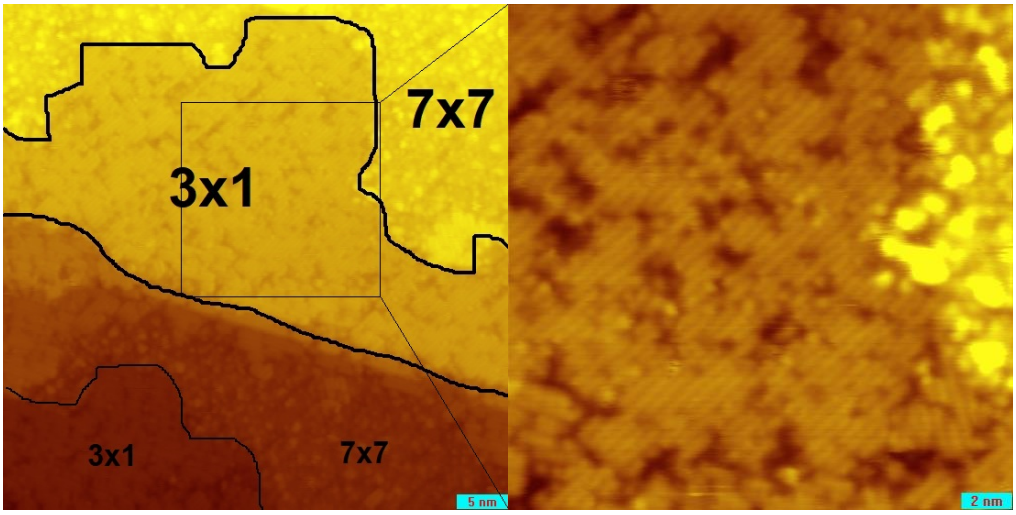

(a) **(b)**

Figure 6.4: STM topographic images of (a) 50 nm × 50 nm and 20 nm × 20 nm scan areas of 9 min Rb deposition with a rate of $2.2 \cdot 10^{-11}$ Torr on the Si(111)-(7 × 7) surface kept at 345°C. (a) is representative of the areas of the surface that convert to (3 × 1) and (b) is a zoom-in in the (3 × 1) area. Image parameters: -2.5 V, 40 pA

$2.2 \cdot 10^{-11}$ Torr) is deposited on a heated substrate conversion of the surface to (3 × 1) only appears as trenches in the terraces extending toward the upper terrace as highlighted in the 50 nm × 50 nm large STM image of Fig. 6.4a. We will call "fingerlike" mode this (3 × 1) growth that involves the formation of trenches in the terraces which strongly modifies the geometry of the terraces, otherwise smooth. A zoom-in in the trenches allows to corroborate these statements. Fig. 6.4b shows a zoom-in of 20 nm × 20 nm large STM scan of the (3 × 1) reconstruction taken in this "fingerlike" region. The parallel filled and empty rows characterizing this reconstruction are clearly visible.

We analyzed multiple STM images of large area scans and count the amount of (3 × 1) areas. In these conditions, as explained above, counting the (3 × 1) areas correspond counting the "fingerlike" regions. Figure 6.5 shows three STM images of 200 nm × 200 nm scan areas of the samples we used for this analysis.

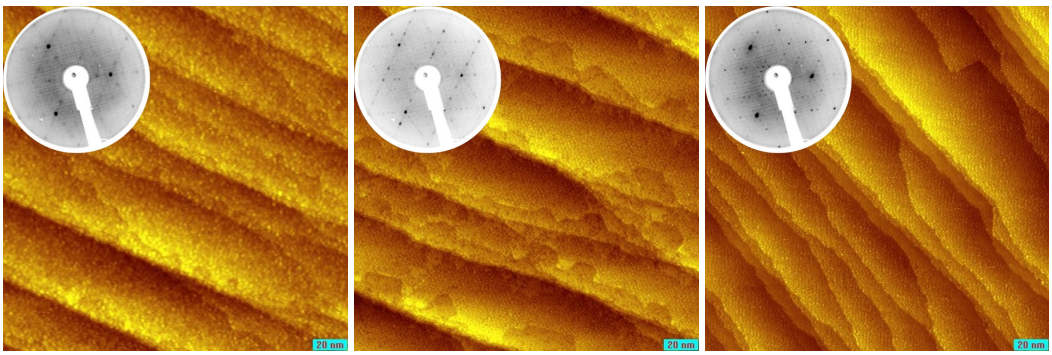

(a) Temperature: 300°C. **(b)** Temperature: 345°C. **(c)** Temperature: 400°C.

Figure 6.5: STM topographic images of 200 nm × 200 nm scan areas of 9 min Rb deposition with a rate of $2.2 \cdot 10^{-11}$ Torr on the Si(111)-(7 × 7) surface kept at different temperatures during deposition ((a) 300°C, (b) 345°C and (d) 400°C. Images are representative of the surface state of the samples. Image parameters: -2.5 V, 40 pA.

An amount of 20% of these areas was found in the sample prepared with deposition of the substrate held at 300°C and an increased amount of 65% on the one at 345°C. No such areas were found on the sample prepared depositing at 400°C.

In summary, from the combined analysis of the LEED diffraction patterns and of the STM topographic scans, the substrate temperature dependence has been studied and has been calibrated.

The maximum Rb induced $(7 \times 7) \rightarrow (3 \times 1)$ conversion has been found upon deposition on the Si(111)-(7×7) surface kept at 345°C. Due to this, the following analysis will be centered on samples prepared at this temperature.

6.1.2 Rubidium amount

The second analysis we performed was on the dependence of the silicon reconstruction on Rb surface coverage. We analyzed various deposition conditions which showed similar trends. Hereafter, a complete analysis of Rb deposition time on samples held at 345°C is presented.

Fig. 6.6 shows the LEED patterns of different amount of Rb deposited with a rate of $2.2 \cdot 10^{-11}$ Torr onto the Si(111)-(7×7) kept at 345°C.

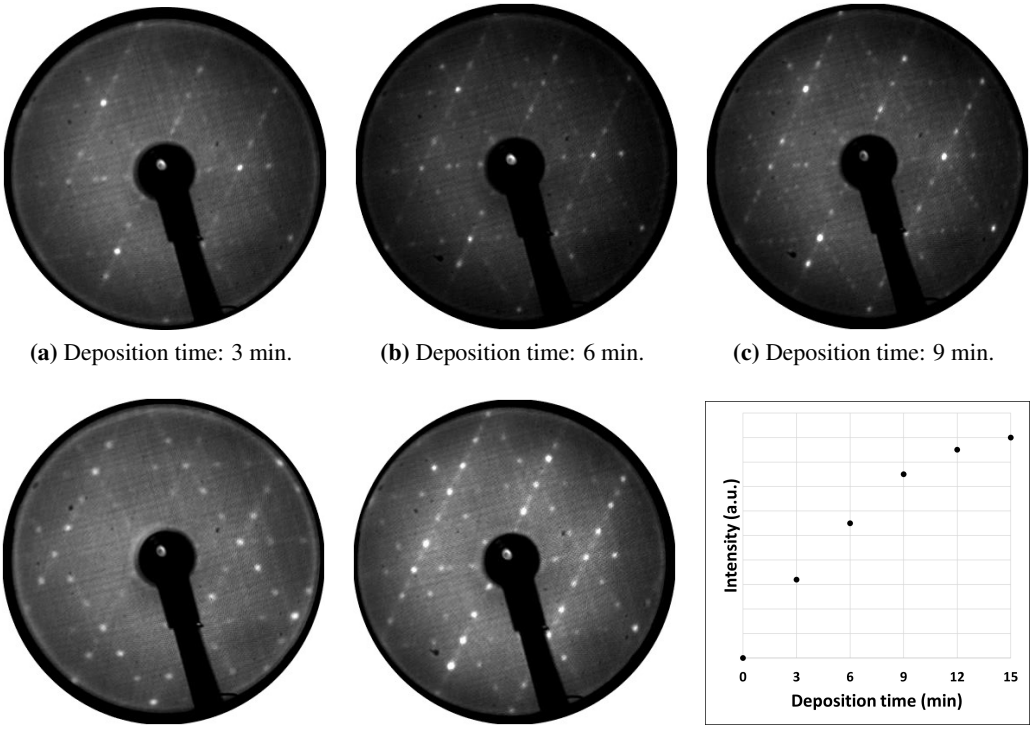

(a) Deposition time: 3 min. **(b)** Deposition time: 6 min. **(c)** Deposition time: 9 min.

(d) Deposition time: 12 min. **(e)** Deposition time: 15 min. **(f)** (3×1) Spot Analysis

Figure 6.6: LEED patterns of (a) 3 min, (b) 6 min, (c) 9 min, (d) 12 min and (e) 15 min Rb deposition with a rate of $2.2 \cdot 10^{-11}$ Torr on the Si(111)-(7×7) surface held at 345°C (Beam Energy: 76.5 eV) and (f) average intensity analysis of the 3×1 LEED spots in the first 1×1 unit cells.

LEED patterns clearly show a transition of the surface structure with increasing Rb coverage. A weak (3×1) pattern began to appear after 3 minutes of Rb deposition. When the Rb coverage was increased, the (3×1) LEED pattern became clearer and the (7×7) spots weaker. After 12 minutes Rb deposition, the (7×7) pattern had completely vanished.

Interestingly, besides the (3×1) spots the LEED patterns obtained upon 12 and 15 minutes Rb deposition revealed the presence of weak and broad spots arranged in a (6×1) pattern

(see Fig. 6.7). The weakness of the (6×1) spots suggests that only a small fraction of the surface is arranged with this periodicity. Moreover, the broadening of the (6×1) spots indicates the presence of small domains. It is to underline that this is the first time that a Rb(6×1) structure has been observed.

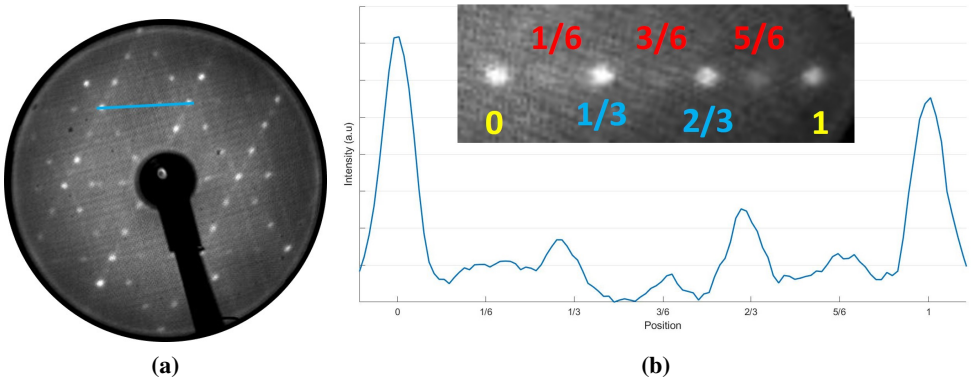

(a) **(b)**

Figure 6.7: (a) LEED pattern of 12 min Rb deposition with a rate of $2.2 \cdot 10^{-11}$ Torr on the Si-(7×7) surface held at 345°C (Beam Energy: 95.5 eV) and (b) cross sections of raw LEED pattern along the line drawn in (a). Cropped LEED pattern showing the (3×1) and (6×1) spots, as inset in (b).

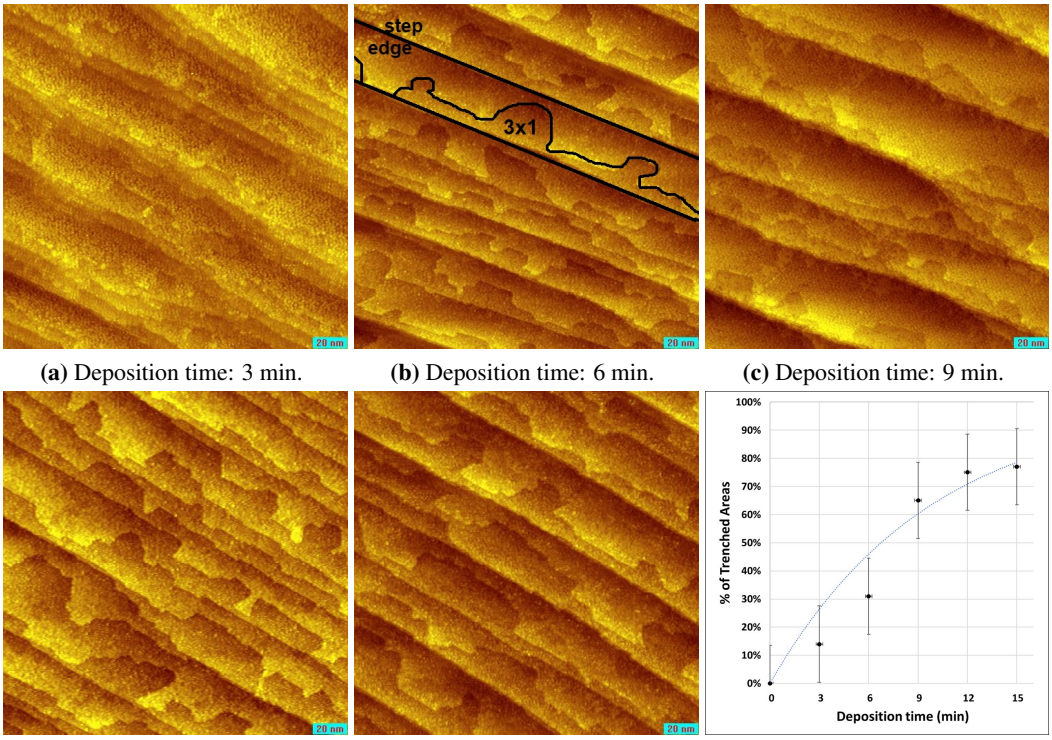

(a) Deposition time: 3 min. **(b)** Deposition time: 6 min. **(c)** Deposition time: 9 min.

(d) Deposition time: 12 min. **(e)** Deposition time: 15 min. **(f)** STM analysis.

Figure 6.8: Figure representative of the $(7 \times 7) \rightarrow (3 \times 1)$ that proceeded in a "fingerlike" mode (explicitly highlighted in (b)). STM topographic images of 200 nm $\times$ 200 nm scan areas of (a) 3 min, (b) 6 min, (c) 9 min, (d) 12 min and (e) 15 min Rb deposition with a rate of $2.2 \cdot 10^{-11}$ Torr on the Si(111)-(7×7) surface kept at 345°C. Images are representative of the surface of the samples. Image parameters: -2.5 V, 40 pA. (f) Plot of the trenched areas in the Rb/Si surface as a function of the deposition time. The line connecting the data points is drawn as a guide to the eye. The error has been taken as the standard error for the % measure, and as 10s for the deposition time.

Upon 3 minutes of Rb deposition, STM revealed the presence of (3×1) areas which appear as trenches in the terraces extending toward the upper terrace. An increasing amount of Rb atoms led to an increase in the number of (3×1) domains as well as an increase in their size. Up to 9 minutes deposition, the growth of the (3×1) domains proceeded by trenches in the terraces extending toward the upper terrace, in a "fingerlike" mode. With a further increase in deposition time, thus rubidium amount, the "fingerlike" growth reached a saturation limit estimated to be around 75% of the surface. This is summarized and shown in Fig. 6.8.

Around 75% of the surface convert into (3×1) in a "fingerlike" mode, further conversion into (3×1) areas appeared as overgrowth on the yet unconverted (7×7) terraces, proceeding from the step edge towards the upper terrace end (see Fig. 6.9). I will refer to this growth as "overgrown". Moreover, deposition of 15 minutes led to an almost complete conversion of the surface structure (see Fig. 6.9b).

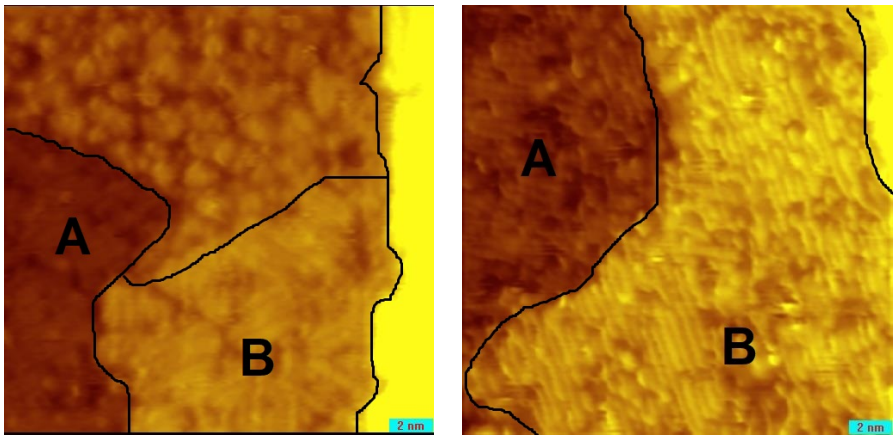

(a) Deposition time: 12 min. **(b)** Deposition time: 15 min.

Figure 6.9: STM topographic images of 20 nm $\times$ 20 nm scan areas of (a) 12 min, and (b) 15 min Rb deposition with a rate of $2.2 \cdot 10^{-11}$ Torr on the Si(111)-(7×7) surface kept at 345°C. Images are representative of the surface of the samples. Image parameters: -2.5 V, 40 pA. The regions labeled with the letters **A** and **B** correspond the (3×1) regions that converted via "fingerlike" mode and "overgrown", respectively. The unlabeled region in (a) represents an unconverted (7×7) region.

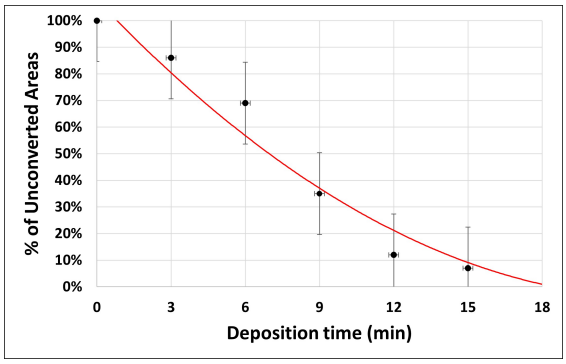

Figure 6.10: Plot of the unconverted areas of the Rb/Si surface as a function of the deposition time. The samples have been prepared by depositing Rb at a rate of $2.2 \cdot 10^{-11}$ Torr on the Si(111)-(7×7) surface held at 345°C during deposition. The red curve represent a second degree polynomial fit of the data, it has been shown as a guide to the eye. The error has been taken as standard for the % measure and for the deposition time as 10s.

It is to state that although LEED showed the presence of a (6×1) phase on the surface, by means of STM we were not able to distinguish (3×1) and (6×1) areas. The difference between the two reconstruction lies only in the orientation of alternate π-bonded chains, thus it would be required high resolution and stability in the images to resolve this difference.

The STM analysis of the converted (either (3×1) or (6×1) areas) and unconverted areas on the surface samples led to the plot shown in Fig. 6.10. It is clear from the plot that an increasing amount of deposited Rb leads to more and more converted areas. In particular it seems possible that 100% conversion can be reached.

6.1.3 Deposition Rate

The last parameter that we analyzed is the Rb evaporation rate. This can be varied by increasing or decreasing the direct current heating of the dispenser (as explained in section 3.5) and was monitored with an RGA (for further details refer to section 3.6).

In the following experiment, the number of Rb atoms evaporated onto the silicon surface has been kept constant by varying, inversely proportional to the deposition rate, the deposition time. The samples here presented were prepared by depositing the Rb atoms onto the silicon substrate kept at 345°C during deposition. 2, 4 and 6 minutes deposition time were used for the samples in which the rubidium atoms were evaporated at rate 1 ($4.1 \cdot 10^{-11}$ Torr), rate 2 ($2.1 \cdot 10^{-11}$ Torr) and 3 ($1.3 \cdot 10^{-11}$ Torr) respectively. Thus the number of Rb deposited on the three samples is (rate 1×2 min $= 8.2 \cdot 10^{-11}$ Torr), (rate 2×4 min $= 8.4 \cdot 10^{-11}$ Torr), and (rate 3×6 min $= 7.8 \cdot 10^{-11}$ Torr). In Fig. 6.11 the LEED patterns of the samples prepared with the three deposition rates are repoted.

(a) Rate 1. Dep. time: 2 min. **(b)** Rate 2. Dep. time: 4 min. **(c)** Rate 3. Dep. time: 6 min.

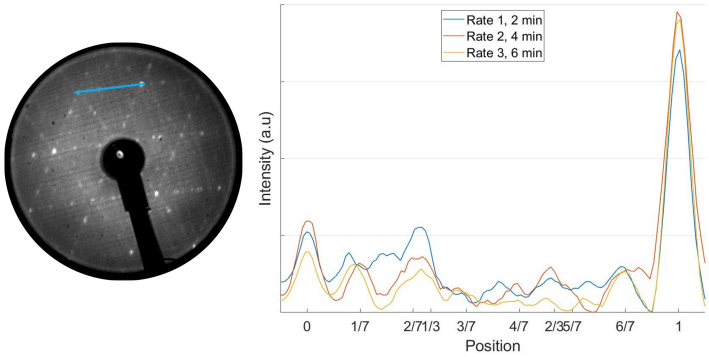

(d) LEED cross section.

Figure 6.11: LEED patterns of Rb deposition for (a) 2 min at rate 1, (b) 4 min at rate 2, (c) 6 min at rate 3 on the silicon substrate kept at 345°C. Beam Energy: 76.5 eV. (d) cross sections of the LEED patterns along the $(10) \rightarrow (01)$ direction, highlighted in the pattern reported on the left.

The analysis of the LEED patterns, i.e. an analysis of the average intensity of the 3×1 spots in the first 1×1 unit cells, for which one cross section is reported in Fig. 6.11d, suggests an equivalence in the three samples.

From the STM topographic images of the three samples we estimated the fraction of (3×1) regions. The (3×1) areas have been identified as the "fingerlike" regions, as previously explained and shown in Fig. 6.4.

Large area scans of the three samples are reported in Fig. 6.12.

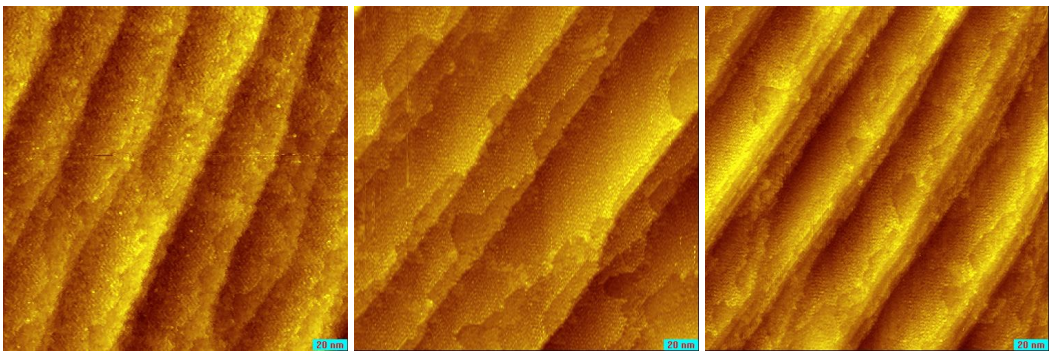

(a) Rate 1. Dep. time: 2 min. **(b)** Rate 2. Dep. time: 4 min. **(c)** Rate 3. Dep. time: 6 min.

Figure 6.12: STM topographic images of 200 nm $\times$ 200 nm scan areas of Rb deposition for (a) 2 min at Rate 1, (b) 4 min at Rate 2, (c) 6 min at Rate 3 on the silicon substrate kept at 345°C. Images are representative of the surface state of the samples. Image parameters: -2.5 V, 40 pA

The STM analysis led to an estimate of (3×1) regions in the three samples which resulted in 34% for sample (Rate 1, 2 min), 34% for sample (Rate 2, 4 min) and 32% for sample (Rate 3, 6 min).

Considering an error of around 3% in the estimation of the converted areas, it results that there is no significant difference between the three samples, i.e. the three samples are equivalent. The result of the STM analysis are in agreement with the results of LEED, suggesting that the deposition rate (in our range) is not a critical parameter for the formation of the (3×1) phase.

6.1.4 Characterization of the (3×1) surface reconstruction

Substrate temperature, Rb amount and rate and their influence on the reconstruction have been analyzed. We discovered that the maximum $(7 \times 7) \rightarrow (3 \times 1)$ can be obtained when silicon is kept at 345°C. Increasing Rb coverage of the surface leads to an enlargement of the (3×1) domains, together with the appearance of a (6×1) phase at LEED. The presence of two growth modes for the (3×1) structure has also been reported. The deposition rate, in our range of analysis, did not significantly influence the reconstruction.

Therefore, I will here review the results obtained upon Rb deposition at $2.2 \cdot 10^{-11}$ Torr on silicon held at 345°C with a particular focus to the 9 and 12 minutes Rb/Si sample.

The LEED patterns obtained upon 12 minutes Rb deposition show high intensity sharp (3×1) spots, and in between these spots other weak and broad spots attributed to a (6×1) periodicity can be seen as well (see Fig.6.13.

Moreover, all three possible rotational domains of the (3×1) structure, each rotated by 120°, can be seen by both LEED and STM (see Fig. 6.14). This symmetry is imposed by the underlying Si(111) substrate. Even though all the rotational domains could be found, the LEED patterns showed a preferential growth direction (already reported in Fig. 6.3).

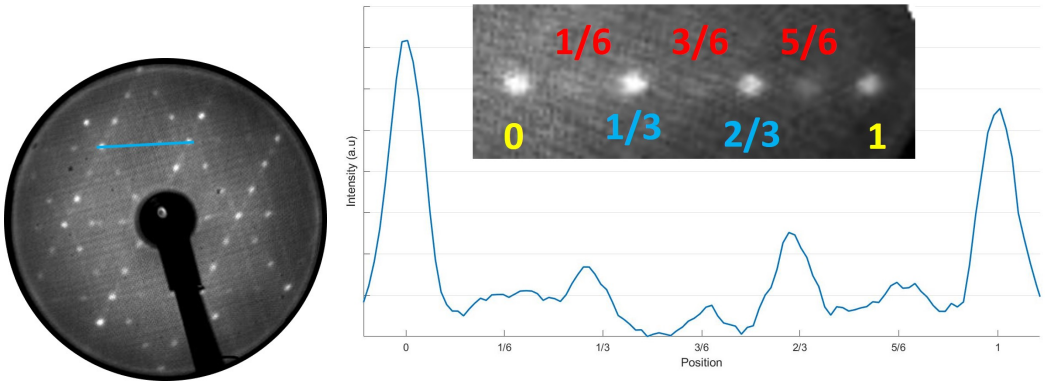

(a) (b)

Figure 6.13: (a) LEED pattern of 12 min Rb deposition with a rate of $2.2 \cdot 10^{-11}$ Torr on the silicon substrate held at 345°C (Beam Energy: 95.5 eV) and (b) cross sections of raw LEED pattern along the line drawn in (a). Cropped LEED pattern showing the (3×1) and (6×1) spots, as inset in (b).

Comparing LEED patterns and STM images we find that the preferred growth direction is the one labeled **A** in Fig. 6.14. This growth direction is one of the two orthogonal to the terrace edge, and this might be due to the way the "fingerlike" regions grow: conversion starts from the step edge and extends toward the inside of the terrace.

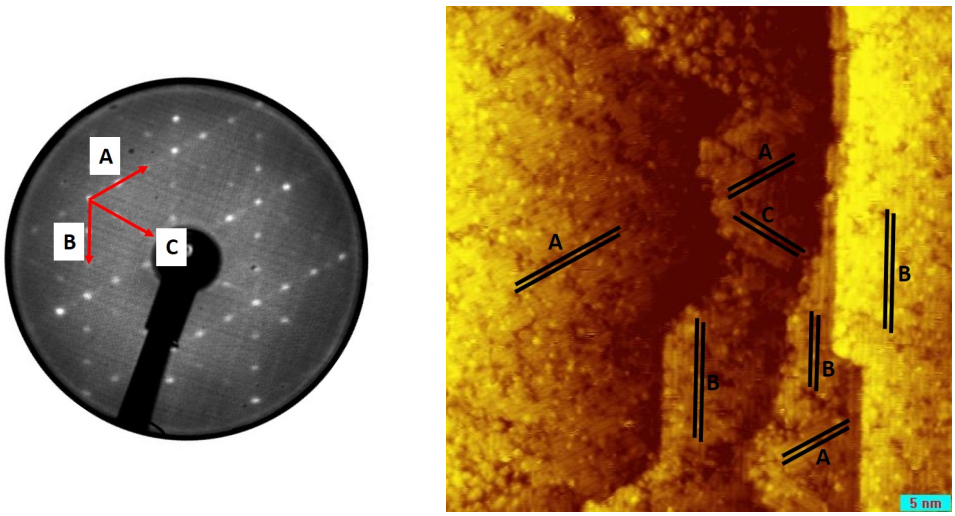

(a) (b)

Figure 6.14: (a) LEED pattern and (b) STM scan of 12 min Rb deposition with a rate of $2.2 \cdot 10^{-11}$ Torr on the silicon substrate held at 345°C. (a) Beam Energy: 95.5 eV). (b) Image size: 50 nm $\times$ 50 nm. Image parameters: -2.5 V, 40 pA. In both figures the three growth direction are labeled and highlighted.

The STM images of the (3×1) regions are characterized by parallel double rows separated by a "missing row" running along the $(1\bar{1}0)$ direction. The experimental distance, measured via STM cross sections along the topographic scans as shown in Fig. 6.15, among the rows is of 11.17 ± 0.57 Å. This is a value that is in very good agreement with the theoretical value of 11.52 Å [52].

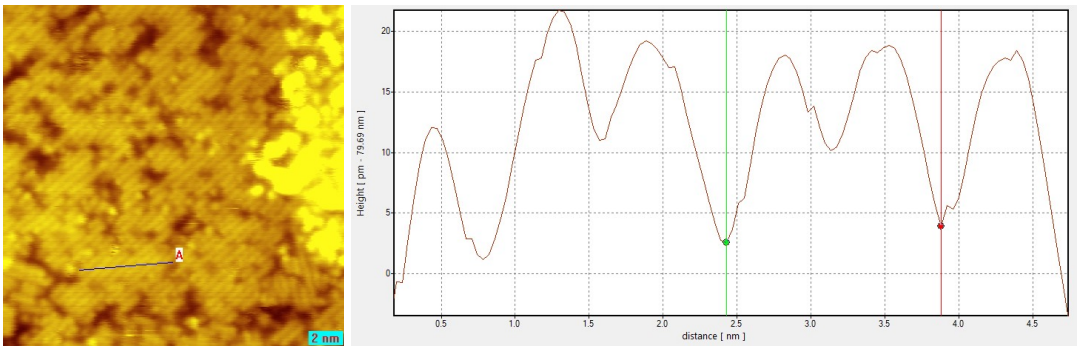

(a) **(b)**

Figure 6.15: (a): STM image of the (3×1) surface from a 20 nm $\times$ 20 nm scan area obtained upon 9 min Rb deposition with a rate of $2.2 \cdot 10^{-11}$ Torr on the silicon substrate kept at 345°C. Image parameters: -2.5 V, 40 pA. (b): Cross section, along the line drawn in (a), reporting the surface periodicity.

Upon closer inspection, this surface contains some disorder represented by defect like extra atoms adsorbed on the rows or vacancies within the rows. This feature is highlighted in Fig. 6.16 which shows a well resolved image of the surface.

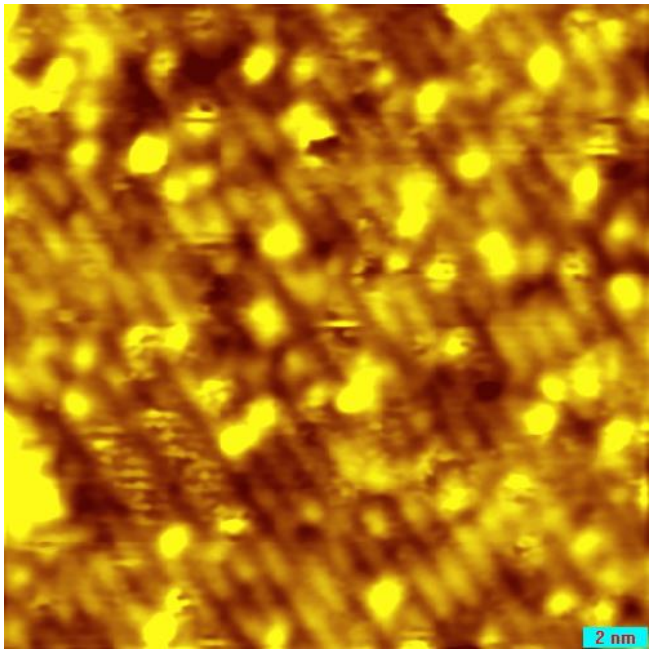

Figure 6.16: STM topographic images of 20 nm $\times$ 20 nm scan area of the (3×1) surface obtained upon 12 min Rb deposition with a rate of $2.2 \cdot 10^{-11}$ Torr on the Si-(7×7) substrate kept at 345°C. Images are representative of the surface state of the samples. Image parameters: -2.5 V, 40 pA. Defects such as vacancies and extra atoms adsorbed on top of the rows are clearly visible.

Fig. 6.17 shows a 50 nm $\times$ 50 nm large STM image and two cross sections taken across terraces. This scan is representative of the (3×1) growth that proceed in a "fingerlike" mode. The STM scan reveals that the growth of the (3×1) domains proceed by trenches in the terraces extending toward the upper terrace. These cross sections have been taken in order to understand whether the (3×1) phase grows on the upper or lower edge of the terrace. The height difference measured going from (7×7) to "fingerlike" (3×1) areas,

measured in different scans, is of 175 ± 24 pm (Cross section B in Fig. 6.17). The height difference measured instead going from "fingerlike" (3×1) to (7×7) areas spanned from few hundreds pm to nm. The results reveal there is an height difference between the (7×7) and the "fingerlike" (3×1) areas and suggest that Si mass transport has occurred in the (3×1) reconstruction process (further details on the possible mechanism of formation will be given in Chapter 7).

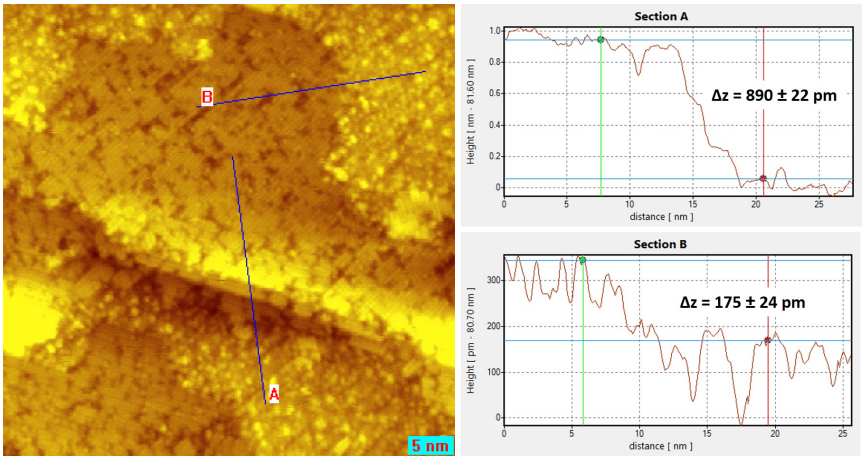

(a) **(b)**

Figure 6.17: (a): STM image from a 50 nm $\times$ 50 nm scan area of 9 min Rb deposition with a rate of $2.2 \cdot 10^{-11}$ Torr on the Si-(7×7) substrate kept at 345°C. Image parameters: -2.5 V, 40 pA. (b): Cross section, along the lines drawn in (a).

Upon deposition of an elevated amount of Rb, the growth proceeded both via "fingerlike" mode and "overgrown". Fig. 6.18 shows a 50 nm $\times$ 50 nm large STM image and two cross sections taken across terraces. The height difference between the "fingerlike" and "overgrown" regions measures 280 ± 35 pm, this value is in agreement with the height of a Si(111) monolayer which is ~ 310 pm. The height difference measured between the "overgrown" and the (7×7) regions on the same terrace is 72 ± 20 pm.

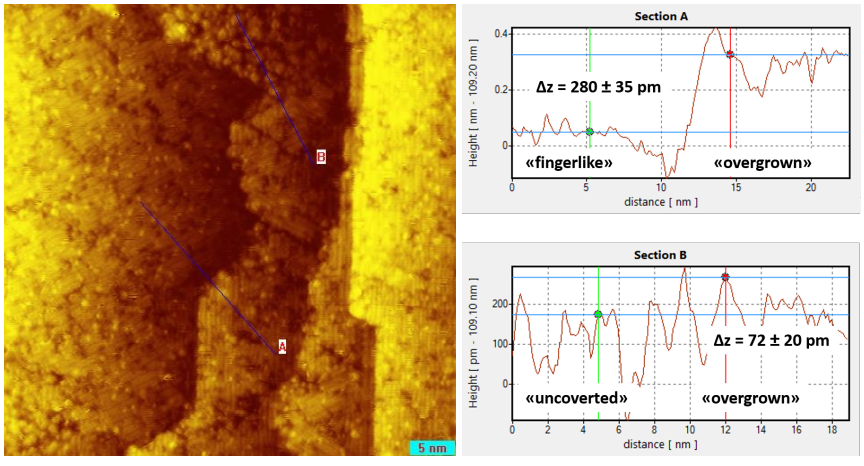

(a) **(b)**

Figure 6.18: (a): STM image from a 50 nm $\times$ 50 nm scan area of 9 min Rb deposition with a rate of $2.2 \cdot 10^{-11}$ Torr on the Si-(7×7) substrate kept at 345°C. Image parameters: -2.5 V, 40 pA. (b): Cross section, along the lines drawn in (a).

The surface electronic character was investigated via scanning tunneling spectroscopy (STS). STS allowed to measure features of the local DOS function ($(dI/dV) \propto LDOS$). Fig. 6.19 shows dI/dV curves taken over the Rb(3×1) surface and of the center adatom in the pristine (7×7) structure (discussed in Chapter 4). Two striking differences are visible between the two spectra. Upon Rb adsorption surface states (S_1 and S_2) vanish as well as the unoccupied state (U_1). Moreover, while the Si-(7×7) surface exhibit a (semi-)metallic character, in the Rb(3×1) phase a large gap opens up. the The Rb(3×1) is semiconducting with a gap of about 1.5 eV. This is consistent with what already reported in literature: the AM(3×1) phase produced by other alkali metals, such as K, Na and Cs [38] was reported to be semiconducting.

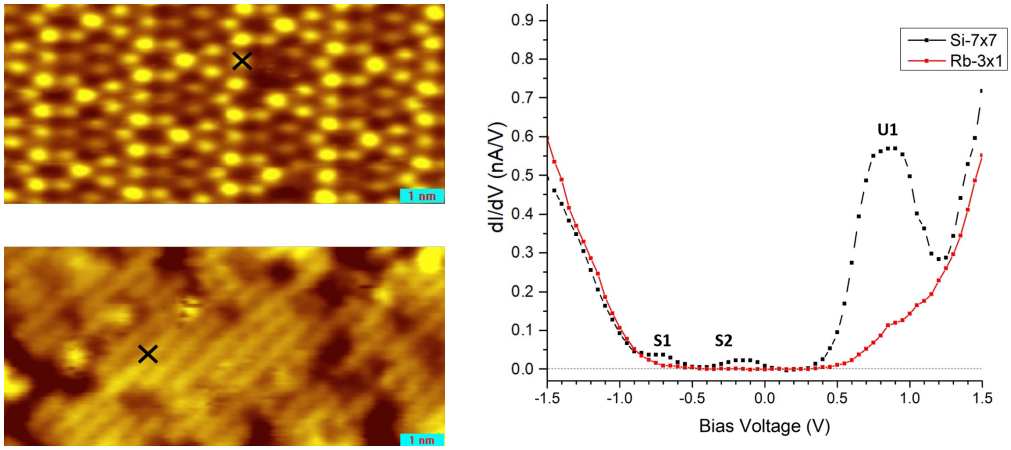

(a) **(b)**

Figure 6.19: (a) STM image of the pristine Si(111)-(7×7) surface and of the (3×1) surface. The **x** highlights the points where the STS spectra were taken. Image parameters: (a) -1.4 V, 0.7 nA, and (b) -2.5 V, 40 pA. (b) Average STS spectra measured at room temperature on a center adatom of the pristine Si(111)-(7×7) and on a row of the Rb(3×1) structure.

The interesting feature here, is that the coexistence phase is an example for a lateral metal-semiconductor contact. We could obtain sample exhibiting large (3×1) and (7×7) regions upon Rb deposition for 6 to 12 minutes at a rate of $2.2 \cdot 10^{-11}$ Torr on the silicon substrate held at 345°C. In such samples, a planar 2D Schottky contact is formed. In particular, the (7×7) domains represent the metallic phase (reminder: the Fermi level is pinned at 0.65 eV in the Si-(7×7)) while the (3×1) domains represent the semiconducting phase.

6.2 Annealing

As we have already seen, the deposition temperature plays an important role. The sample prepared by dosing Rb for 12 minutes at a rate of $2.2 \cdot 10^{-11}$ Torr on Si(111)-(7×7) held at 345°C was annealed for 10 minutes at 400°C. This sample was then readily analyzed by LEED and STM. We did this annealing step to study the stability of the Rb-Si system and the effect of heating the (3×1) phase.

Figure 6.20a shows the typical LEED pattern of the pristine Si(111)-(7×7) surface. Deposition of 12 minutes of Rb evaporated at a rate of $2.2 \cdot 10^{-11}$ Torr on the (7×7) surface (Fig. 6.20a) held at 345°C led to the formation of the (3×1) and (6×1) phases clearly visible in the LEED pattern in Fig. 6.20b (and in Fig. 6.7). A 400°C annealing of this surface led to the complete disappearance of the (3×1) and (6×1) spots.

After the annealing, the LEED pattern in 6.20c and better highlighted in the cross section in Fig. 6.20i clearly shows the presence of high intensity (1×1) spots. In particular, the ratio between the intensity of the (1×1) spots relative to the unfaulted (labeled as '0') and the spot relative to the faulted half (labeled as '1') of the unit cell is $\frac{I_0}{I_1} \sim 8.4$, higher than the ratio $\frac{I_0}{I_1} \sim 5$ measured for the pristine (7×7). The reappearance of some weak fractional (7×7) spots is also seen in the LEED patterns (Fig. 6.20c).

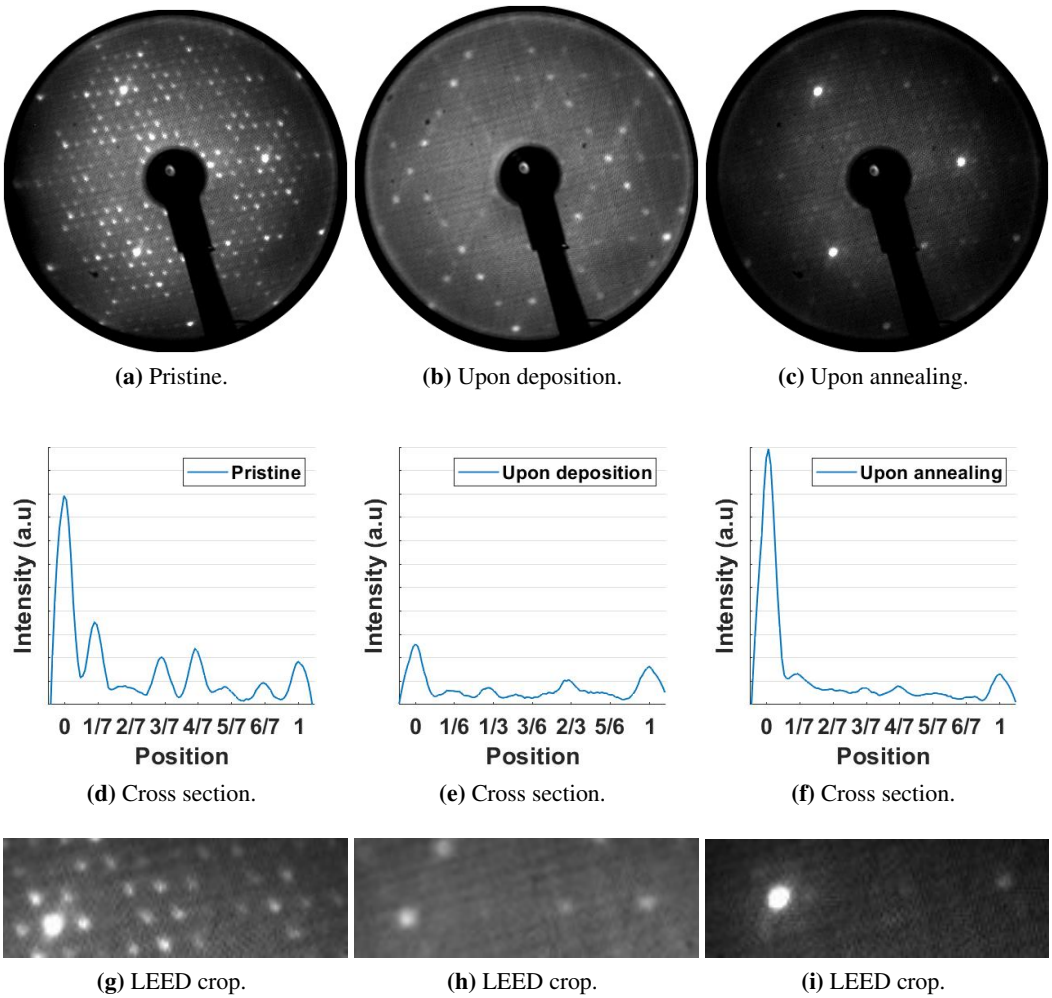

(a) Pristine. **(b)** Upon deposition. **(c)** Upon annealing.

(d) Cross section. **(e)** Cross section. **(f)** Cross section.

(g) LEED crop. **(h)** LEED crop. **(i)** LEED crop.

Figure 6.20: LEED patterns of (a) the pristine silicon sample, (b) after 12 minutes Rb at a rate of $2.2 \cdot 10^{-11}$ Torr deposited on the silicon substrate kept at 345°C, and (c) after a 10 minutes annealing at 400°C. Beam Energy: 76.5 eV. The second row shows the cross sections of raw LEED patterns along the $(10) \rightarrow (01)$ direction, highlighted in the third row that shows LEED patterns cropped in this region

The distinct difference in the topography of the surface obtained after producing the (3×1) phase and after the sample annealing becomes apparent already from large area STM scans (see Fig. 6.21). The STM image shown in Fig. 6.21a has been taken before the annealing and has already been discussed in section 6.1.4. After the annealing STM reveals the presence of islands on the surface, encircled in Fig. 6.21b.

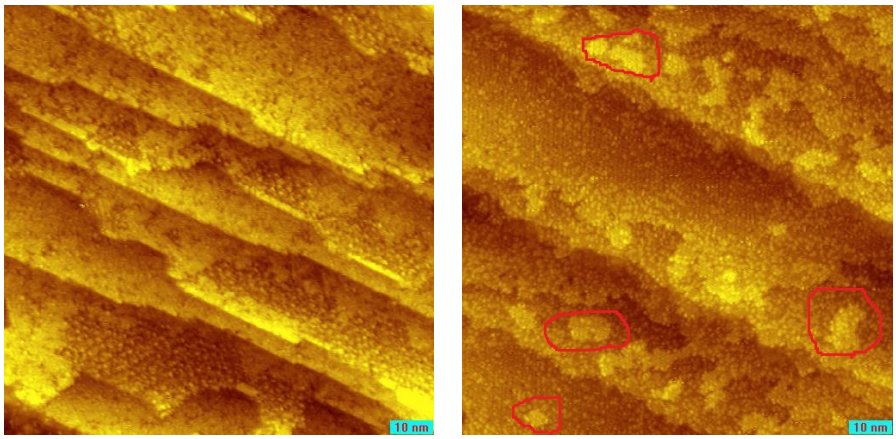

(a) (b)

Figure 6.21: STM topographic images of 100 nm × 100 nm scan areas of 12 min Rb deposition at a rate of $2.2 \cdot 10^{-11}$ Torr on the silicon substrate kept at 345°C. (a) After the deposition and (b) after a 10 minutes annealing at 400°C. Images are representative of the surface state of the samples. In (b) some of these newly revealed island are encircled in red. Image parameters: (a) -2.5 V, 40 pA and (b) -2 V, 40 pA.

A closer inspection of the surface allowed to demonstrate the complete disappearance of the (3×1) and (6×1) phase (which, in this sample, was covering almost 90% of the surface) both on the terraces and at the step edges. The terraces were covered by the (7×7) phase and clusters of atoms adsorbed on this reconstruction in a disordered way, as shown in Fig. 6.22.

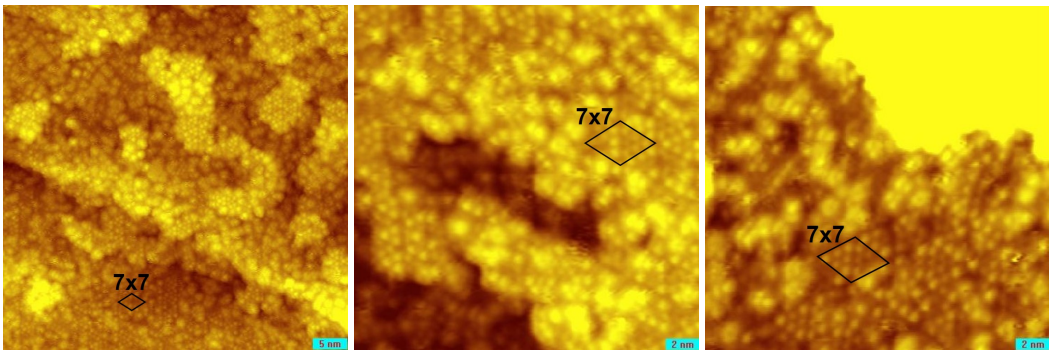

(a) (b) (c)

Figure 6.22: STM topographic images taken after annealing 10 minutes at 400°C the sample of 12 min Rb deposition at a rate of $2.2 \cdot 10^{-11}$ Torr on the silicon substrate kept at 345°C. Scan area: (a) 50 nm × 50 nm, (b) and (c) (a) 20 nm × 20 nm. Image parameters: -2 V, 40 pA.

The islands instead preferentially nucleate in the regions where the (3×1) growth progressed in a "fingerlike" fashion. These are just few unit cells large, and 300 ± 11 pm high a value that corresponds to the height of a Si(111) bilayer. In particular the islands are at the same height as the upper terrace. Cross sections along the islands are reported in Fig. 6.23.

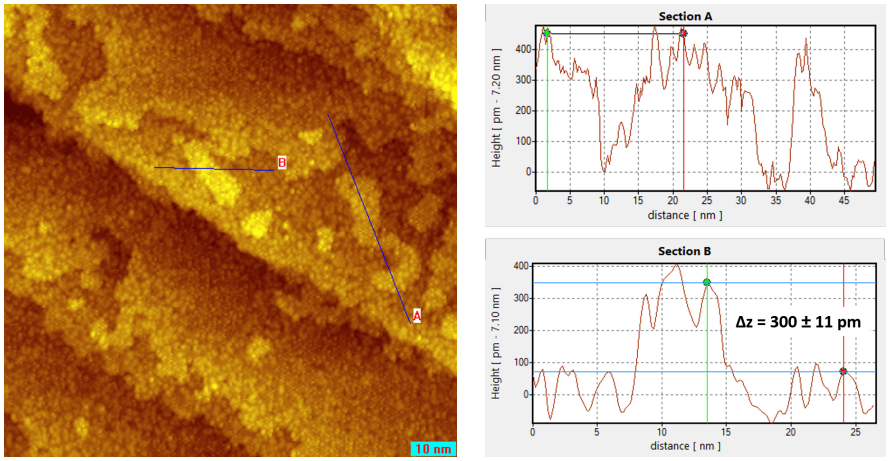

(a) **(b)**

Figure 6.23: (a): STM image from a 100 nm $\times$ 100 nm scan area of the (3×1) surface taken after an annealing at 400°C of Rb deposition at 345°C on the (7×7) silicon substrate for 12 min at a rate of $2.2 \cdot 10^{-11}$ Torr. Image parameters: -1.6 V, 30 pA. (b): Cross section, along the lines drawn in (a).

The islands are formed by domains with either of three different DAS reconstruction, i.e. (5×5), (7×7) and (9×9). From Fig. 6.24, it is possible to see that the adatoms in the (5×5) and (9×9) unit cell are arranged similarly to the (7×7), but instead of 12 adatoms per unit cell there are 6 and 20 adatoms, respectively. Surrounding the adatoms are 4 corner holes identical to the 4 corner holes surrounding the adatoms of the (7×7) unit cell. The stacking fault presents in all the three DAS structure in question manifests in the filled state images as brightness difference between the two halves of the unit cell. Moreover, since the islands are formed by domains of different periodicity, vacancy and faults are created as highlighted by the red arrow in Fig. 6.24b placed at the boundary between (5×5) and (7×7) domains.

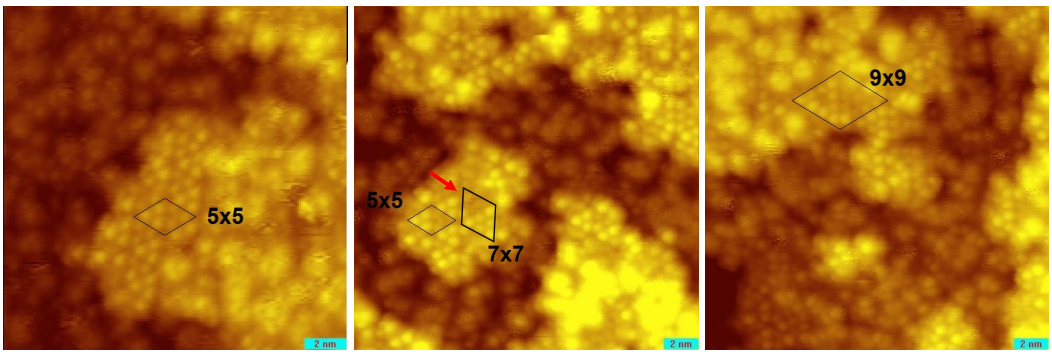

(a) **(b)** **(c)**

Figure 6.24: STM topographic images of (a) 10 nm $\times$ 10 nm, (b) and (c) 20 nm $\times$ 20 nm scan areas taken after annealing 10 minutes at 400°C the sample of 12 min Rb deposition at a rate of $2.2 \cdot 10^{-11}$ Torr on the silicon substrate kept at 345°C. The unit cell of the (5×5), (7×7), and (9×9) reconstructions are highlighted. The red arrow indicate a boundary between two DAS regions. Image parameters: -1.6 V, 30 pA.

6.3 Results summary

In this chapter, we first studied the effect of Rb deposition on a Si(111)-(7×7) at elevated temperatures. We found formation of a (3×1) reconstruction. Then we analyzed the dependence of the (3×1) reconstruction on the deposition conditions, i.e. substrate temperature, deposition time and deposition rate. We analyzed the (3×1) reconstruction on an optimized sample and studied the effect 400°C annealing of the latter.

What we found is that of Rb at elevated temperatures induces a (3×1) reconstruction in a temperature range of about 300-390°C, even at low Rb coverage. The substrate temperature at which we obtained the highest amount of surface conversion is about 345°C.

By increasing the amount of Rb, on silicon kept at 345°C, we found that it might be possible to obtain a 100% conversion of the surface. Moreover, up to a conversion of about 75% of the surface periodicity into (3×1) the growth of the reconstructed domains proceeds in a "fingerlike mode", that is by trenches in the terraces that extend toward the upper terrace. Further conversion of the surface proceeds in "overgrowth", conversion appears also on the lower terrace and proceeds from the step edge towards the terrace end.

At high Rb coverage, the LEED patterns showed the presence of a (6×1) reconstruction. This reconstruction has never been seen for Rb as adsorbate.

The deposition rates we analyzed proved not to be a critical parameter for the formation of the (3×1) structure.

An optimized sample has been used to characterize the (3×1) structure obtained by depositing Rb on a heated substrate. In particular, the analysis performed on this sample revealed the semiconducting character of the Rb(3×1) surface.

On this sample we also performed an annealing step at 400°C. After this step, we saw Rb desorption and destabilization of the (3×1) reconstruction which completely disappeared. Islands of either three different DAS reconstruction ($n \times n$, with $n = 5, 7, 9$) appeared on the surface, preferentially in the "fingerlike" regions left by the (3×1) formation. The terraces were instead covered by the (7×7) phase and clusters of atoms adsorbed on this reconstruction in a disordered fashion.

Chapter 7

Summary and discussion

7.1 The Rb induced (3×1) reconstruction

7.1.1 Ordering and nucleation

The underlying concept of the adsorbate-induced surface reconstruction phenomenon (such as the Rb(3×1) silicon reconstruction) is the displacement of substrate atoms at (or near) the surface to new equilibrium positions in response to the changes of their energy induced by particles chemisorption. The adsorption may cause reconstruction of the surface, involving displacement of many substrate atoms, and result in a surface structure which is substantially different from the unreconstructed or clean surface.

Reconstruction of a surface with adsorption mainly depends on the surface coverage of the adsorbate and on the experimental conditions (e.g. temperature, pressure[1]). I will here review the effect of both factors and provide a simple model to explain the experimental evidences presented in the previous chapters.

7.1.1.1 Deposition at RT

Upon deposition of Rb at room temperature, Rb atoms disorderly adsorb on top of Si atoms, but preferentially on the faulted half of the unit cell. The (3×1) phase could only be obtained upon annealing (discussed Chapter 5). In this case the (3×1) phase is found to nucleate mainly near the step edge on the lower terraces or on defects of the underlying silicon surface, but never isolated in the center of the terraces (as clearly shown in Fig. 5.7a). Near the step edge on the lower terrace, the density of Rb atoms is highly increased. Since this was not observed before the annealing, it is a clear indication of the an increase in the mobility of the Rb atoms due to the thermal energy provided by the annealing and proves that the bonding created between the Rb and Si atoms is weak, upon RT deposition of Rb. Rb atoms move preferentially towards the step edges where the periodicity of the surface is broken and thus the silicon atoms have an additional dangling bond which implies higher free energy. In the case of RT deposition, the amount of (3×1) reconstructed areas increased with deposition time (Rb quantity), however did not exceed a few percent of the total surface, even at high dosing time. The presence of only (7×7) spots in the LEED patterns result thus justified.

Experimental data suggests that the (3×1) formation is an activated process and it can start only when enough energy is supplied to the system. Moreover, annealing temperature increases the Rb atoms mobility, favoring them to reach the suitable sites for reconstruction.

[1] This entire thesis work has been performed in UHV conditions. The pressure never exceeded $3 \cdot 10^{-9}$ mbar.

The most suitable sites are represented by the step edge of the lower terrace. This process is in competition with Rb evaporation from the surface, causing the lost of part of the Rb atoms. Therefore, if the annealing temperature is too high, losses are expected to prevent or destroy the (3×1) reconstruction. Moreover, the (3×1) structure only forms when the Rb density is high enough (area under consideration must be larger than a (7×7) unit cell) then Rb will react with the Si atoms and form (3×1) domains. A sketch of the process is shown in Fig. 7.1. In figure, the (3×1) domains are shown as protrusions from the flat (7×7) terrace. According to what we found experimentally (shown in Fig. 5.7) the (3×1) reconstruction protrudes of ~ 180 pm from the flat terrace, in the bias conditions we used to scan the surface.

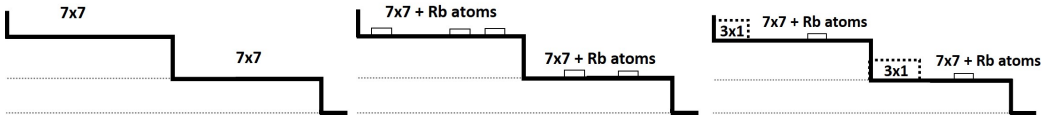

(a) Pristine **(b)** As deposited **(c)** After the annealing

Figure 7.1: Model for the Rb(3×1) induced by an annealing of RT rubidium deposition. Schematic of (a) Pristine Si-(7×7), (b) after RT Rb deposition, Rb atoms are adsorbed on top of the (7×7) surface, and (c) upon annealing where small (3×1) regions coexist with the phase in (b).

7.1.1.2 Deposition at elevated temperature

The (3×1) phase obtained upon deposition onto a heated substrate (discussed in Chapter 6) showed some similarities with the RT deposition. Also in this case, for low to medium Rb coverages (deposition for $0-9$ min with a rate of $2.2 \cdot 10^{-11}$ Torr), the (3×1) phase starts growing from the step edge. Conversely to what happens upon RT deposition the growth starts on the upper terrace edge and keeps on growing towards the inside of the terrace, in a "fingerlike" mode (as can be seen in the cross section of Fig. 6.17). The conversion from large terraces and smooth step structure of the pristine wafer into terraces where the step edges are very rough and with "fingerlike" structures extending over a large area of the terraces suggest high mass transport in the transformation from (7×7) to (3×1).

With increasing amount of Rb, (3×1) regions grow in size and reach a saturation point at which this phase grows together with a (6×1) phase. The appearance of the newly obtained phase with doubled periodicity could be ascribed to the large atomic size of the Rb atom ($r_a = 220 \pm 9$ pm) as well as to the Rb nearest neighbor distance (4.78 Å) which is larger than that of the Si(111)-(1×1) lattice spacing (3.84 Å) thus the (3×1) row or the two zigzag chain rows are stretched out laterally to enhance the width of the row and are shifted slightly along the row to produce the (6×1) structure, as already reported for the Cs adsorbed on Si(111) [35, 43]. The appearance of the (6×1) structure in the LEED is accompanied by the STM observation such that the "fingerlike" growth mode reaches a saturation (at about 75% of the surface converted into (3×1)) and the surface transition keeps going from the step edges on the lower terrace towards the trenched regions. I called this growth mode "overgrown" since it is shows up as an overgrowth on the (7×7) terrace. It can be possible the phase that "overgrows" is a (6×1) structure, since this new growth mode and the LEED (6×1) spots appear simultaneously. Moreover this could be one of the reasons of an height difference between the "fingerlike" domains and the "overgrown" domains. However it can also be possible that the difference that we measure between the two height is not real but it is just an effect induced by the different electronic surroundings. However, it is to underline that the switch in growth mode allowed to obtain almost complete conversion of the surface.

The most interesting feature of the Rb(3×1) grown on the Si(111)-(7×7) held at elevated temperatures is that the phase grows in two domains "fingelike and "overgrowth". It is to note that in this case, if the deposition temperature is too low then Rb atoms will not have enough mobility to reach suitable sites to form the reconstruction. If the deposition temperature is instead to high, Rb atoms will not even stick to the surface. Based on our experimental observations, I suggest for the formation process the following model.

Deposited Rb atoms can migrate across the (7×7) surface and react at a suitable sites to form the (3×1) structure. At the initial stage of formation the suitable sites are the step edge on the upper terrace. Rb, reacting with Si atoms will form "fingerlike" regions. Since the (3×1) phase is characterized by a smaller Si atom density, the Si surplus is ejected onto the surrounding (7×7) region (as shown in Fig. 7.2b). As long as we deposit low-medium amounts of Rb the Rb-Si reaction will take place predominantly at the upper terraces step edge (as shown in Fig. 7.2c). However, when the excess of silicon becomes important, new favored sites of reaction will be formed (this happens at amount of deposited Rb). Rb atoms will react with this excess and form the "overgrown" domains (as shown in Fig. 7.2d). A sketch of the process is shown in Fig. 7.1. The height of the (3×1) domains have been chosen according to what we found experimentally (shown in Fig. 6.17 and in Fig. 6.18).

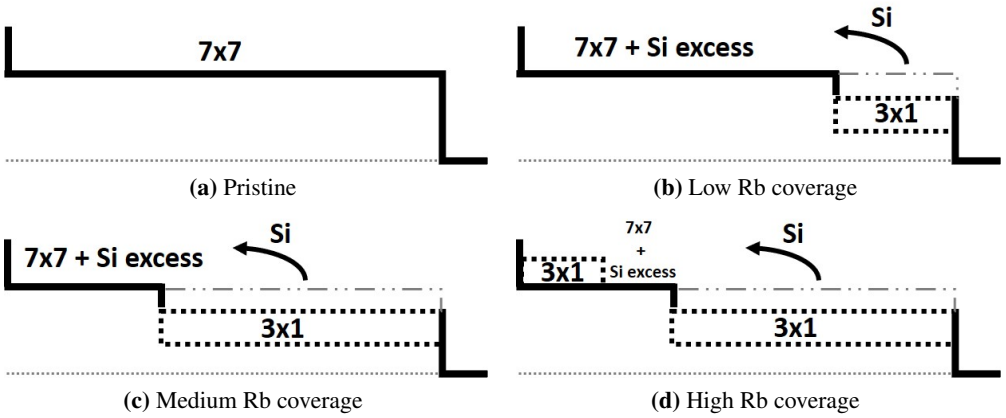

(a) Pristine **(b)** Low Rb coverage

(c) Medium Rb coverage **(d)** High Rb coverage

Figure 7.2: Model for the Rb(3×1) induced by elevated temperature Rb deposition. Process at (a) low Rb coverage, and (b) high Rb coverage. The gray dash-dotted line shows the geometry of the pristine (7×7) terrace.

7.1.2 Summary

For the reconstruction process to happen it is required for the adsorption energy (the driving force of the surface reconstruction) to be higher than the cohesion energy of the substrate atoms otherwise the process is hindered. The difference between these two energies represents the energy barrier that has to be overcome. A balance between adsorption, desorption and diffusion processes must be reached in order for the reconstruction processes to happen.

Indeed, we observed that the (3×1) reconstruction appears only upon annealing or when the substrate is held at elevated temperature, in a precise and narrow range of temperatures (300-390°C).

Upon deposition at RT, Rb atoms have low kinetic energies, and this translates in a reduced diffusion length (approximately one unit cell). Despite the low mobility, the system will try to reach the configuration of minimal energy. The deposited Rb will move in the vicinity of the spot where it arrived at the silicon surface, and what we see is adsorption preferentially on the faulted half of the unit cell. The thermal annealing of the (Rb/Si) sample

increases the probability of overcoming the energy barrier favoring the diffusion process (the diffusion coefficient has the form of an Arrhenius equation, thus $\propto e^{-a/k_BT}$). Rb atoms gain enough mobility to move towards suitable adsorption sites and (3×1) patches appear on the annealed sample (in Fig. 7.3b). The annealing can be pictured as a lowering of the energy barrier, however it has to be kept in mind that this is just a representation and what increases is just the probability of the process.

Heating the silicon surface during deposition brings the surface to a higher free energy state thus lowering the activation barrier (in Fig. 7.3b). Rb atoms can move on a more reactive surface and start the (3×1) conversion process. It is to underline here that for the process to happen the adsorption must be favored compared to desorption otherwise Rb atoms will not stick to the Si surface.

The concepts expressed above are summarized in the energy diagrams schematically shown in Fig. 7.3.

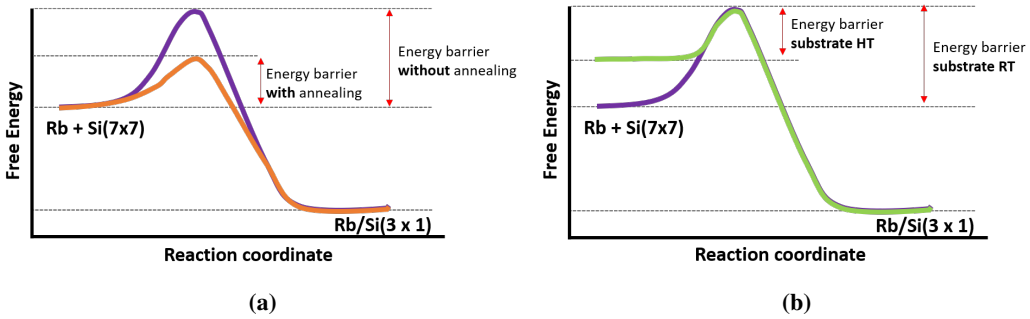

Figure 7.3: Energy diagram for the (3×1) formation starting (a) from RT deposition, and (b) on the silicon substrate held at elevated temperature. The violet line indicates the reaction energy diagram of the pristine reaction. The orange and green line indicate the reaction energy diagrams with the a favored energetic for the reconstruction process.

7.2 Desorption

As it has been shown above, temperature plays an important role in the formation of the (3×1) phase. Temperature is also a critical parameter in the desorption process of Rb atoms from the surface and in the formation of other intermediate silicon structures prior to the complete restoration of the pristine (7×7) surface.

Rb desorption, from the sample containing the (3×1) phase obtained by RT deposition followed by an annealing of the system at 300°C, became clear after an annealing at 350°C. The (3×1) phase completely disappeared but the Rb atoms that did not leave the surface mainly aggregated near the terrace edges. Rb atoms that instead desorbed from the surface, left holes in the (7×7) structure. Further annealing at higher temperature, led to the decrease in the number of Rb clusters adsorbed on the (7×7). However the number of holes and defects on the surface did not increase, suggesting that also a rearrangement of silicon atoms took place.

In the case of Rb deposited on a heated substrate, the annealing led to somehow different observations. A 400°C annealing of this surface led to the complete disappearance of the (3×1) domains. A distinct topographic difference became apparent already from large STM scan areas. The STM images revealed the presence of just few unit cells large and $\sim$ 300 pm high island on the surface (this value correspond to a Si(111) bilayer). The islands preferentially

nucleate in the regions where the (3×1) growth progressed in a "fingerlike" fashion. These new domains are formed by either of three different DAS reconstruction, i.e. (5×5), (7×7) and (9×9), while the terraces show a (7×7) periodicity. In this case, a rearrangement of the silicon atoms became clear.

The absence of additional DAS reconstructions in the desorption and reconstruction step of the samples prepared by RT deposition is to be expected. In the case of RT deposition, the (3×1) reconstruction is mainly confined to small domains and the other Rb atoms are bound to the (7×7) reconstruction in the form of single atom or small clusters. With deposition on a heated substrate, the (3×1) domains are larger and strongly modify the geometry and the structure of the pristine silicon terraces on a larger scale. Once Rb starts to desorb it destabilize the (3×1) structure. The destabilization of the (3×1) leaves also disordered silicon atoms, that were involved in the reconstruction, on the terraces in an unfavorable energy state. With the annealing, this excess of silicon is free to move towards the "holes" left by the "fingerlike" domains and rearrange in more energetically favored reconstruction (refer to adsorption model shown in Fig. 7.2). The process of reconstruction, in this case, must undergo some intermediate phases since the mobility of silicon is limited (annealing at 400°C, normally a stable (7×7) reconstruction is obtained by an annealing at 600°C or above).

In both cases, after a last annealing at 600°C, the pristine surface was restored. Few defects, represented mainly by additional atoms (either Si or rubidium silicides), placed on the surface structure at domain boundaries, were still present. These defects were then eliminated by flashing the surface. This is a clear indication of the reversibility of the adsorption and reconstruction process of Rb on Si(111)-(7×7).

7.3 Conclusions

The main achievement of this thesis has been to obtain for the first time real space images of the Rb-induced (3×1) reconstruction on the Si(111)-(7×7). We also obtained the first LEED evidence of a Rb-induced (6×1) structure.

More in general, in this thesis work, we carried out an STM and LEED investigation on the effect of Rb deposition on the Si(111)-(7×7). We first characterized the Si-(7×7) reconstructed samples that served as substrate for the deposition. We demonstrated the reproducibility of the preparation method as well as the state of the art of the samples. The Rb-Si interaction was then studied by depositing Rb on the Si-(7×7) surface either at room temperature or held at elevated temperatures, in the range of 300-400°C. The evolution of the structure upon deposition was studied via annealing cycles.

Consistently with the observation on other alkali metals [8, 35, 36, 44, 48, 49] we found that room temperature deposition of Rb did not induce any new surface reconstruction nor modification of the (7×7) periodicity of the underlying silicon substrate. Rb atoms rather adsorbed on the (7×7) surface in a disordered fashion, but preferentially in the faulted half of the unit cell. Upon a mild annealing, the surface showed some degree of rearrangement: after a 300°C annealing, (3×1) domains formed on the surface. The same results were found on Cs and K [36]. Moreover, the domain size was found to increase with the amount of deposited Rb. Further annealing of the surface only led to progressive Rb desorption.

On the other hand, Rb deposition on the (7×7) surface held at elevated temperatures was found to readily induce a (3×1) reconstruction. We studied the influence of the deposition temperature on the reconstruction. The temperature range in which we observe the (3×1) reconstruction (300-390°C) is compatible with the range reported by Daimon and Ino [8]. Subsequently, we studied the effect of surface coverage. Two striking feature came out from

this study. At high Rb dosing time, the Rb(3×1) is found to grow in two modes and separated domains, named "fingelike and "overgrown". Moreover, at these dosing time, we evidence the presence of at LEED of a (6×1) pattern, previously observed only with Cs [35, 43]. We also performed STS on Rb(3×1) areas and we discovered that the reconstruction is semiconducting with a large energy gap (~ 1.5 eV). Consistently with what already reported for the (3×1) induced by other alkali metals [38].

Also, in these deposition conditions an annealing of the (3×1) surface led to the desorption of Rb atoms. However, in this case the surface showed the presence of Si rearrangement. This manifested in the (7×7) rearrangement of the terraces but more evidently in islands grown in the trenched terraces. The islands were reconstructed in either of three DAS reconstruction, i.e. (5×5), (7×7), and (9×9). These DAS structure were also observed during Na desorption from the (3×1) surface [62].

We conclude the investigation with a model for the growth and nucleation of the Rb(3×1) reconstruction and we discuss the desorption process in order to explain our experimental observations.

The results reported in this thesis complement and add to the literature of a wide field such the metal-semiconductor interfaces. The alkali metal-Si interface that has been a main focus of experimental and theoretical investigations, since the discovery of the stable (7×7) reconstruction. Of particular interest both from a chemical and electrical prospective has been the (3×1) reconstruction. Even though in the years a lot of experimental observations have been accumulated, there are still some unanswered question on the system. In particular, the atomic size of the AM seems to play an important role on the observed differences among the alkalies. Our study on Rb results particulartly interesting, relevant, and worth, for many reasons but mainly because Rb has a large atomic radius which is comparable to Cs. Up to now, the lack of an extended literature on the system has prevented for further speculations on the size importance.

Bibliography

[1] I. M. Ross, "The foundation of the silicon age," *Bell Labs Technical Journal*, vol. 2, no. 4, pp. 3–14, 1997.

[2] K. Oura, M. Katayama, A. V. Zotov, V. G. Lifshits, and A. A. Saranin, *Surface Science*. Springer Berlin Heidelberg, 2003.

[3] C. B. Duke, "Semiconductor Surface Reconstruction: The Structural Chemistry of Two-Dimensional Surface Compounds," *Chemical Reviews*, vol. 96, pp. 1237–1260, Jan. 1996.

[4] K. Takayanagi, Y. Tanishiro, M. Takahashi, and S. Takahashi, "Structural analysis of Si(111)-7×7 by UHV-transmission electron diffraction and microscopy," *Journal of Vacuum Science & Technology A: Vacuum, Surfaces, and Films*, vol. 3, pp. 1502–1506, May 1985.

[5] M. Mauerer, I. L. Shumay, W. Berthold, and U. Höfer, "Ultrafast carrier dynamics in Si$(111)7\times7$ dangling bonds probed by time-resolved second-harmonic generation and two-photon photoemission," *Phys. Rev. B*, vol. 73, p. 245305, Jun 2006.

[6] B. Reihl, R. Dudde, L. Johansson, K. Magnusson, S. Sorensen, and S. Wiklund, "The bonding of alkali metals to semiconductor surfaces: a direct and inverse photoemission study," *Applied Surface Science*, vol. 56-58, pp. 123 – 136, 1992.

[7] C. Chan, K. Ho, and K. Bohnen, "Chapter 3 - surface reconstruction: Metal surfaces and metal on semiconductor surfaces," in *Physical Structure* (W. Unertl, ed.), vol. 1 of *Handbook of Surface Science*, pp. 101 – 136, North-Holland, 1996.

[8] H. Daimon and S. Ino, "Study of the Si(111) 7×7 surface structure by alkali-metal adsorption," *Surface Science*, vol. 164, no. 1, pp. 320 – 326, 1985.

[9] D. Jeon, T. Hashizume, T. Sakurai, and R. F. Willis, "Structural and electronic properties of ordered single and multiple layers of Na on the Si(111) surface," *Phys. Rev. Lett.*, vol. 69, pp. 1419–1422, Aug 1992.

[10] M. Tikhov, L. Surnev, and M. Kiskinova, "Na-induced (7×7)-to-(3×1) structural transformation on a Si(111)7×7 surface and the resulting passivation of the surface towards interaction with oxygen," *Phys. Rev. B*, vol. 44, pp. 3222–3225, Aug 1991.

[11] K. J. R. Rosman and P. D. P. Taylor, "Isotopic compositions of the elements 1997 (Technical Report)," *Pure and Applied Chemistry*, vol. 70, pp. 217–235, Jan. 1998.

[12] G. Mileti, C. Affolderbach, F. Droz, and E. M. Murphy, "Navigating more precisely with laser clocks," *ESA bulletin*, no. 122, pp. 52–58, 2005.

[13] S. Marcuccio, A. Genovese, and M. Andrenucci, "Experimental Performance of Field Emission Microthrusters," *Journal of Propulsion and Power*, vol. 14, pp. 774–781, Sept. 1998.

[14] I. Shvarchuck, K. Dieckmann, M. Zielonkowski, and J. Walraven, "Broad-area diode-laser system for a rubidium Bose-Einstein condensation experiment," *Applied Physics B: Lasers and Optics*, vol. 71, pp. 475–480, Oct. 2000.

[15] A. M. Kaufman, R. P. Anderson, T. M. Hanna, E. Tiesinga, P. S. Julienne, and D. S. Hall, "Radio-frequency dressing of multiple Feshbach resonances," *Physical Review A*, vol. 80, Nov. 2009.

[16] T. Gentile, W. Chen, G. Jones, E. Babcock, and T. Walker, "Polarized He-3 spin filters for slow neutron physics," *Journal of Research of the National Institute of Standards and Technology*, vol. 110, p. 299, May 2005.

[17] Y. Wang, Z. Li, R. Tan, and W. Huang, "Research on Rb-DPAL for the pumping of SERF rubidium magnetometers," in *AOPC 2017: Laser Components, Systems, and Applications* (L. Jiang, S. Jiang, L. Wang, and L. Zhang, eds.), SPIE, Oct. 2017.

[18] U. Roelcke, E. Radü, K. von Ammon, O. Hausmann, R. Maguire, and K. Leenders, "Alteration of blood-brain barrier in human brain tumors: comparison of [18F]fluorodeoxyglucose, [11C]methionine and rubidium-82 using PET," *Journal of the Neurological Sciences*, vol. 132, pp. 20–27, Sept. 1995.

[19] L. E. Long, "Rubidium-Strontium method," in *Encyclopedia of Earth Science*, pp. 556–561, Kluwer Academic Publishers.

[20] G. Grosso and G. P. Parravicini, *Solid State Physics, Second Edition*. Academic Press, 2 ed., 2013.

[21] `https://en.wikipedia.org/wiki/Electronic_band_structure`.

[22] J. Kubby and J. Boland, "Scanning tunneling microscopy of semiconductor surfaces," *Surface Science Reports*, vol. 26, no. 3, pp. 61 – 204, 1996.

[23] D. Chadi, "Atomic structure of reconstructed group IV and III–V semiconductor surfaces," *Ultramicroscopy*, vol. 31, no. 1, pp. 1 – 9, 1989.

[24] C. Duke, "Surface structures of tetrahedrally coordinated semiconductors: principles, practice, and universality," *Applied Surface Science*, vol. 65-66, pp. 543 – 552, 1993.

[25] G. Binnig, H. Rohrer, C. Gerber, and E. Weibel, "7×7 Reconstruction on Si(111) Resolved in Real Space," *Phys. Rev. Lett.*, vol. 50, pp. 120–123, Jan 1983.

[26] H. N. Waltenburg and J. T. Yates, "Surface Chemistry of Silicon," *Chemical Reviews*, vol. 95, pp. 1589–1673, July 1995.

[27] R. Laven, "Ultra-Thin Ag Films on the Sn/Si(111)-$\sqrt{3} \times \sqrt{3}$ Surface Studied by STM," Master's thesis, Karlstads Universitet, June 2018.

[28] R. M. Tromp, R. J. Hamers, and J. E. Demuth, "Quantum states and atomic structure of silicon surfaces," *Science*, vol. 234, no. 4774, pp. 304–309, 1986.

[29] D. Jeon, T. Hashizume, and T. Sakurai, "Scanning Tunneling Microscopy of the Na/Ge(111)3×1," *Le Journal de Physique IV*, vol. 06, pp. C5–189–C5–194, Sept. 1996.

[30] W. C. Fan and A. Ignatiev, "Metal-adsorbate-induced Si(111)-(1×3) reconstruction," *Physical Review B*, vol. 41, pp. 3592–3595, Feb. 1990.

[31] K. J. Wan, X. F. Lin, and J. Nogami, "Comparison of the 3×1 reconstructions of the Si(111) surface induced by Li and Ag," *Physical Review B*, vol. 46, pp. 13635–13638, Nov. 1992.

[32] T. Sekiguchi, F. Shimokoshi, T. Nagao, and S. Hasegawa, "A series of Ca-induced reconstructions on Si(111) surface," *Surface Science*, vol. 493, no. 1, pp. 148 – 156, 2001.

[33] J. Quinn and F. Jona, "New results on the reaction of Si111 with Mg," *Surface Science Letters*, vol. 249, no. 1, pp. L307 – L311, 1991.

[34] J. J. Paggel, H. Haak, W. Theis, and K. Horn, "Na adsorption on Si(111)-7×7 studied by scanning tunneling microscopy and photoemission," *Journal of Vacuum Science & Technology B: Microelectronics and Nanometer Structures Processing, Measurement, and Phenomena*, vol. 11, no. 4, pp. 1439–1443, 1993.

[35] K.-S. An, H.-W. Yeo, K.-W. Lee, R.-J. Park, J.-S. Kim, C.-Y. Park, and S.-B. Lee, "Reconstruction of a Cs-adsorbed Si(111) 7×7 Surface," *Journal of the Korean Physical Society*, vol. 27, no. 1, pp. 111–113, 1994.

[36] T. Hashizume, K. Motai, Y. Hasegawa, I. Sumita, H. Tanaka, S. Amano, S. Hyodo, and T. Sakurai, "Alkali metal adsorption on the Si(111)7×7 surface," *Journal of Vacuum Science & Technology B: Microelectronics and Nanometer Structures Processing, Measurement, and Phenomena*, vol. 9, no. 2, pp. 745–747, 1991.

[37] R. Z. Bakhtizin, C. Park, T. Hashizume, and T. Sakurai, "Scanning tunneling microscopy study of the (3×1) reconstruction induced by Li adsorption on the Si(111) surface," *Applied Surface Science*, vol. 87-88, pp. 347 – 352, 1995. Proceedings of the 41st International Field Emission Symposium.

[38] D. Jeon, T. Hashizume, and T. Sakurai, "Scanning tunneling microscopy of alkali metal-induced structures on the Si(111) surface," *Journal of Vacuum Science & Technology B: Microelectronics and Nanometer Structures Processing, Measurement, and Phenomena*, vol. 12, no. 3, pp. 2044–2048, 1994.

[39] T. Okuda, H. Shigeoka, H. Daimon, S. Suga, T. Kinoshita, and A. Kakizaki, "Surface and bulk core level shifts of the Si(111) 3×1-Na and Si(111) $\delta 7 \times 7$-Na surfaces," *Surface Science*, vol. 321, no. 1, pp. 105 – 110, 1994.

[40] K. Sakamoto, T. Okuda, H. Nishimoto, H. Daimon, S. Suga, T. Kinoshita, and A. Kakizaki, "Photoemission study of the Si(111)3×1-K surface," *Phys. Rev. B*, vol. 50, pp. 1725–1732, Jul 1994.

[41] J. J. Paggel, G. Neuhold, H. Haak, and K. Horn, "Scanning-tunneling-microscopy and photoemission study of an alkali-metal-induced structural phase transition: Si(111)-(7×7) into Si(111)-Na(3×1)," *Phys. Rev. B*, vol. 52, pp. 5813–5823, Aug 1995.

[42] A. A. Saranin, A. V. Zotov, V. G. Lifshits, J.-T. Ryu, O. Kubo, H. Tani, T. Harada, M. Katayama, and K. Oura, "Reexamination of the $\mathrm{Si}(111)3 \times 1 - \mathrm{Na}$ reconstruction on the basis of si atom density and unit cluster determination," *Phys. Rev. B*, vol. 58, pp. 3545–3548, Aug 1998.

[43] C.-Y. Park, K.-S. An, J.-S. Kim, R.-J. Park, J. Chung, T. Kinoshita, A. Kakizaki, and T. Ishii, "Photoemission study of the Si(111)6×1-Cs surface," *Physical Review B*, vol. 52, no. 11, pp. 8198–8202, 1995.

[44] S. Mizuno and A. Ichimiya, "RHEED study of alkali metals on Si(111) surface," *Applied Surface Science*, vol. 33-34, pp. 38 – 44, 1988.

[45] S. Lagomarsino, F. Scarinci, P. Castrucci, C. Giannini, E. Fontes, and J. Patel, "Si-alkali metal interface study by X-ray standing wave technique in ultrahigh vacuum with synchrotron radiation," *Applied Surface Science*, vol. 56-58, pp. 402–407, Jan. 1992.

[46] V. Eteläniemi, E. G. Michel, and G. Materlik, "X-ray standing-wave study of alkali-metal/Si(111)7×7 interfaces," *Phys. Rev. B*, vol. 48, pp. 12023–12031, Oct 1993.

[47] P. Castrucci, S. Lagomarsino, F. Scarinci, and C. Giannini, "Multisite occupancy at the alkali/silicon (111) interface studied with XSW," *Journal of Physics D: Applied Physics*, vol. 26, pp. A192–A196, Apr. 1993.

[48] K.-H. Wu, Y. Fujikawa, Y. Takamura, and T. Sakurai, "Alkali Metal Adsorption on the Si(111)-(7 × 7) Surface," *Chinese Journal of Physics*, vol. 43, pp. 197–211, Feb. 2005.

[49] K. O. Magnusson and B. Reihl, "Development of the surface electronic structure of K and Cs overlayers on Si(111)7×7," *Physical Review B*, vol. 41, pp. 12071–12075, June 1990.

[50] Y. Tezuka, H. Daimon, and S. Ino, "Change of Surface Electronic States Induced by Li and K Adsorption on the Si(111)7×7 Structure," *Japanese Journal of Applied Physics*, vol. 29, pp. 1773–1777, sep 1990.

[51] D. Rodrigues, "Alkali-metal adsorption on Si(111) surfaces: a comparative study of the bonding nature for Li, Na, K and Rb," *Journal of Physics: Condensed Matter*, vol. 5, pp. A123–A126, aug 1993.

[52] S. C. Erwin, "New Structural Model for the Alkali-Induced Si(111)-(3 × 1) Reconstruction from First Principles," *Phys. Rev. Lett.*, vol. 75, pp. 1973–1976, Sep 1995.

[53] K. C. Pandey, "Reconstruction of the Si(100)-2x1 Surface," in *Proceedings of the 17th International Conference on the Physics of Semiconductors* (J. D. Chadi and W. A. Harrison, eds.), (New York, NY), pp. 55–58, Springer New York, 1985.

[54] L. Basta, "A calorimetric study of hydrogen storage on graphene functionalized with Titanium," Master's thesis, Universitá di Pisa, Pisa, 2017.

[55] L. Meng, Y. Wang, L. Zhang, S. Du, R. Wu, L. Li, Y. Zhang, G. Li, H. Zhou, W. A. Hofer, and H.-J. Gao, "Buckled Silicene Formation on Ir(111)," *Nano Letters*, vol. 13, pp. 685–690, Jan. 2013.

[56] C. J. Chen, *Introduction to Scanning Tunneling Microscopy*. Oxford University Press, Sept. 2007.

[57] B. Voigtländer, *Scanning Probe Microscopy*. Springer Berlin Heidelberg, 2015.

[58] S. Fiori, "Li-functionalized Graphene on Silicon Carbide," Master's thesis, Universitá di Pisa, Pisa, 2017.

[59] H. Lüth, *Surface and Interfaces of Solids*. Springer Berlin Heidelberg, 1993.

[60] J. D. Levine, S. H. McFarlane, and P. Mark, "Si (111) 7 × 7 surface structure: Calculations of LEED intensity and comparison with experiment," *Phys. Rev. B*, vol. 16, pp. 5415–5425, Dec 1977.

[61] J. E. Northrup, "Origin of surface states on Si(111)(7×7)," *Phys. Rev. Lett.*, vol. 57, pp. 154–154, Jul 1986.

[62] S. Olthoff, A. McKinnon, and M. Welland, "Thermal desorption of Na from Na-Si(111)3 × 1: in situ observation of the 3 × 1-to-7 × 7 structural transformation using a high-temperature scanning tunnelling microscope," *Surface Science*, vol. 326, no. 1, pp. 113 – 123, 1995.